CORROSION OF TITANIUM, ZIRCONIUM AND THEIR ALLOYS FOR BIOMEDICAL APPLICATIONS

by

Yue Zhang

A thesis submitted to the University of Birmingham
for the degree of DOCTOR OF PHILOSOPHY

School of Metallurgy and Materials
College of Engineering and Physical Sciences
University of Birmingham
September 2017

ABSTRACT

The degradation of Ti implant surfaces *in vivo,* has remained a concern despite its perceived excellent corrosion resistance. Elevated levels of metal release have been detected both locally and systemically, often leading to unfavourable biological responses. Therefore, it is important to understand how and why the metal corrodes in physiological environments, and the nature of corrosion products that are likely to generated.

The corrosion behaviour of Ti, Zr and their alloys (Ti6Al4V and TiZr) were studied in simulated physiological solutions. It was found that albumin, the most prevalent tissue fluid protein, induced a time-dependent dissolution of Ti6Al4V in the presence of H_2O_2, an inflammatory biomolecule commonly found in peri-implant sites, in 0.9% NaCl. However, the corrosion of Zr was observed to be unaffected by the presence of H_2O_2 and/or albumin in 0.9% NaCl. Furthermore, TiZr alloys have been shown to possess enhanced passivity in comparison to CP Ti in the various exposure conditions including highly acidic (HCl), oxidative environments (H_2O_2 in 0.9% NaCl) and cell cultures (macrophage).

Corrosion products of Zr were characterised *in situ* by synchrotron X-ray methods and were found to be $ZrOCl_2 \cdot 8H_2O$, tetragonal ZrO_2, and Zr metal fragments in 0.9% NaCl regardless of the presence or absence of H_2O_2 and/or albumin. The presence of Zr metal fragments as a result of an electrochemical corrosion process indicates the generation of metal species in the absence of mechanical wear.

ACKNOWLEDGEMENT

My sincere thanks go to a great many people who guided and helped me on this piece of work.

Prof. Alison Davenport and Prof. Owen Addison, having them both as my supervisors are truly a great fortune. They guided me with patience, extensive support, and their broad sicentific expertise. I am so grateful to have them to lead my way of thinking as a scientist and evolving as a person.

My thanks also go to people who offered their technical expertise. Thanks to Dr. Bernerd Burke for extensive help on biological work. Thanks to Prof. Mihai Stoica and Dr. Konstantin Ignatyev for their expertise and assistance at Diamond Light Source.

My acknowledge also goes to Prof. John Scully and Dr. Brendy Rincon Troconis for kindly hosting my stay at University of Virginia. Also to Scully's students for their kindness, supports and help.

Thanks to all my collegues: Liya, Fei, Augus, Steven, Flaviu, Alex, Qi, Nina, Cleo, Helen, I enjoyed having them as my peer, my friend, and my contestant. I also want to thank to a special friend Nargis, who made me feel loved and kept me as part of the family while writing up in a country with 10 inches of snow.

In the end, I wish to express my sincere gratitude and love to my dad Shourun, my mom Suxia, and my patner Rui. Their unconditional love, support and compassion are my fuel for this 4 year's 'marathoon'

TABLE OF CONTENTS

1 INTRODUCTION 1

2 LITERATURE REVIEW 4

2.1 Ti and its alloys as dental implants 4

2.1.1 Commercially pure (CP) Ti and Ti6Al4V 4

2.1.2 TiZr binary alloys 7

2.2 Corrosion of Ti and its alloys in *in vivo* conditions 9

2.2.1 General corrosion 9

2.2.2 Localised corrosion 11

2.2.3 Mechanically assisted crevice corrosion 14

2.3 *in vitro* corrosion studies of Zr, Ti and its alloys 17

2.3.1 Introduction 17

2.3.2 The effect of environmental acidity, chloride and hydrogen peroxide 18

2.3.3 Effect of proteins 27

2.3.4 Effect of cellular induced corrosion 30

2.4 Clinical failure and biological impact of implant metal release 32

2.4.1 Failure of Ti dental implants 32

2.4.2 Release and toxicity of metal degradation products 33

2.4.3 Current understandings of *in vivo* metal degradation 35

2.5 Current standards of corrosion testing of biomedical materials 36

2.6 Synchrotron X-ray radiation techniques 37

2.6.1 Introduction 37

2.6.2 X-ray diffraction (XRD) 38

2.6.3 X-ray absorption spectroscopy (XAS) 39

2.7 Summary 41

3 MATERIALS AND METHODS 43

3.1 Materials 43

3.2 Sample and surface preparation 45

3.2.1 Samples for metallographic characterisation 45

3.2.2 Samples for electrochemical measurements 46

3.2.3 Samples for cell culture immersion tests 46
3.2.4 Samples of Zr artificial pits for in-situ synchrotron characterisation 46
3.3 Electrochemical measurements and testing solutions 47
3.3.1 General procedure 47
3.3.2 Potentiodynamic Polarisation 49
3.3.3 Potentiostatic Polarisation 50
3.3.4 Electrochemical Impedance spectroscopy (EIS) 51
3.3.5 Electrochemical measurements of Zr artificial pits and bulk Zr samples 52
3.4 Immersion tests 53
3.4.1 Corrosion (ion release) in macrophage cell culture 53
3.4.2 Incubation of Ti6Al4Vin H_2O_2 and/or albumin containing solutions to investigate morphology of surface oxide layer 55
3.4.3 Quantification of metal release 55
3.5 *in situ* characterisation of Zr artificial corrosion pit using synchrotron X-ray methods 56
3.5.1 X-ray diffraction 56
3.5.2 X-ray absorption near edge structure 58
3.6 Surface characterisation 59
3.6.1 Surface coverage of cells on Ti, Zr and TiZr substrates 59
3.6.2 Surface morphology of Ti6Al4V and Zr after corrosion 61
3.7 Transmission electron microscopy 61
4 THE EFFECT OF ZR ADDITION ON THE CORROSION OF TI IN SIMULATED PHYSIOLOGICAL CONDITIONS 63
4.1 Introduction 63
4.2 Microstructure Characterisation 65
4.3 Corrosion behaviour in HCl 68
4.4 Corrosion behaviour in physiological saline with and without H_2O_2 71
4.5 Metal ion release associated with THP-1 culture 76
4.5.1 THP-1 cell adherence 76

4.5.2 Morphology and surface coverage of M1 and M2 phenotypes of THP-1 cells 78
4.5.3 Cellular induced metal ion release 81
4.6 Discussion 87
4.6.1 Zr reduces the passive current density of Ti in HCl solutions 87
4.6.2 Zr contents increased corrosion resistance of CP Ti in physiological saline with H_2O_2 89
4.6.3 Increased pitting susceptibility by higher Zr concentrations to Ti. 90
4.6.4 Zr additions enhance cell mediated corrosion resistance 90
4.7 Conclusion 93
5 SYNERGISTIC EFFECTS OF ALBUMIN AND H_2O_2 ON CORROSION OF TI6AL4V 95
5.1 Introduction 95
5.2 Corrosion under open circuit conditions 97
5.2.1 Open circuit potential 97
5.2.2 Potentiodynamic polarisation 98
5.2.3 Electrochemical impedance spectroscopy (EIS) 100
5.2.4 Surface morphology after corrosion 103
5.3 Time dependent corrosion behaviour at controlled potential 107
5.4 Metal ion release and EIS measurement at constant potentials 108
5.4.1 Metal ion release at constant potentials 108
5.4.2 Potentiostatic EIS 110
5.5 Discussion 113
5.5.1 Effect of exposure time on corrosion of Ti6Al4V in the presence of H_2O_2 with and without addition of albumin 113
5.5.2 Effect of potential on dissolution and oxide film formation on Ti6Al4V in presence of albumin and H_2O_2 117
5.6 Conclusions 122
6 IN SITU CHARACTERISATION OF CORROSION PRODUCTS IN ZR ARTIFICIAL PIT AND BULK ZR ELECTROCHEMISTRY IN SIMULATED PHYSIOLOGICAL SOLUTIONS 123

6.1 Introduction 123
6.2 Electrochemistry of Zr artificial pits 125
6.3 Structure of Zr corrosion products formed in-situ 127
6.4 Structure of black corrosion products further away from the corrosion front 129
6.5 Structure of the salt layer adjacent to the corrosion front 132
6.6 Comparison of corrosion species in the simulated physiological solutions 134
6.7 XANES of Zr solution species 137
6.8 *ex situ* microscopy of Zr corrosion products and its dissolving interface 138
6.8.1 SEM of the dissolving Zr interface 138
6.8.2 TEM of Zr corrosion products 139
6.9 Electrochemical polarisation on bulk Zr surfaces 142
6.9.1 Anodic Polarisation 142
6.9.2 SEM of Zr pits following anodic breakdown 144
6.10 Discussions 146
6.10.1 Formation of Zr metal fragments 146
6.10.2 $ZrOCl_2 \cdot 8H_2O$ 147
6.10.3 Tetragonal ZrO_2 148
6.10.4 The effects of H_2O_2 and albumin on electrochemistry of Zr and formation of Zr corrosion products and their biomedical implications 150
6.11 Conclusion 153
7 GENERAL DISCUSSION AND FUTURE WORK 155
7.1 General discussion 155
7.1.1 The need for improved environmental conditions and methods for corrosion testing 155
7.1.2 Characterisation of degradation products in simulated physiological environment 159
7.1.3 Corrosion behaviour and development opportunities of binary TiZr alloys 161

7.2 Future Work 163
7.2.1 Improved approximation of testing solutions to peri-implant environment 163
7.2.2 Further studies of corrosion tests on TiZr binary alloys 164
7.2.3 Characterisation of degradation products of TiZr 164
7.2.4 Exposing cells to simulated corrosion products 165
7.2.5 Opportunities for the development of new TiZr based ternary alloys 165
8 CONCLUSIONS 167
9 REFERENCES 169

LIST OF ABBREVIATIONS

^{125}I	Iodine-125 (radiolabelling for proteins)
AC	Alternating Current
AES	Auger Electron Spectroscopy
AESEC	Atomic emission spectroelectrochemistry
AFM	Atomic Force Microscopy
Ag/AgCl	Silver/silver chloride electrode
Al_2O_3	Aluminium oxide
ANOVA	Analysis of variance
ASTM	American Society for Testing and Materials
BAHA	Bone-Anchored-Hearing-Aid
BSA	Bovine Serum Albumin
BSE	Back scattered electron
CE	Counter electrode
CoCrMo	Cobalt Chromium Molybdenum alloy
CP Nb	Commercially Pure niobium
CP Ti	Commercially Pure titanium
CP Zr	Commercially Pure zirconium
CPE	Constant Phase Element
DC	Direct Current
EDTA	Ethylenediaminetetraacetic acid
EDX/EDS	Energy Dispersive X-ray spectroscopy
EIS	Electrochemical Impedance Spectroscopy
E-pH	Potential-pH (diagram)
EXAFS	Extended X-ray Absorption Fine Structure
FCS	Fetal Calf Serum
FWHM	Full Width Half Maximum
H_2O_2	Hydrogen peroxide

HCl	Hydrochloric acid
HF	Hydrofluoric acid
HNO_3	Nitric acid
ICP-MS	Inductively Coupled Plasma Mass Spectroscopy
IFN-γ	Interferon gamma
IL-4	Interleukin 4
LPS	Lipopolysaccharide
M1	Pro-inflammatory phenotype of macrophage
M2	Tissue repair phenotype of macrophage
MACC	Mechanically Assisted Crevice Corrosion
NADPH	Nicotinamide adenine dinucleotide phosphate
OCP	Open Circuit Potential
PBS	Phosphate Buffered Saline
PMA	Phorbol 12-myristate 13-acetate
PVC	Polyvinyl chloride
QCM	Quartz Crystal Microbalance
RE	Reference electrode
ROS	Reactive Oxygen Species
RPMI-1640	Roswell Park Memorial Institute-1640 (cell culture medium)
SBF	Simulated Body Fluid
SCE	Saturated Calomel Electrode
SDS	Sodium dodecyl (lauryl) sulfate
SE	Secondary electron
SEM	Scanning Electron Microscopy
SiC	Silicon Carbide
SOD	Superoxide dismutase
TEM	Transmission Electron Microscopy
THP-1 cells	Human monocytic cell line

Ti6Al4V	ASTM Grade 5
Ti6Al4V-ELI	ASTM Grade 5, extra low interstitial
TiO_2	Titanium dioxide
TiZr	Titanium zirconium alloy
UTS	Ultimate Tensile Strength
WE	Working electrode
XANES	X-ray Absorption Near Edge Structure
XAS	X-ray Absorption Spectroscopy
XPS	X-ray Photoelectron Spectroscopy
XRD	X-ray Diffraction
$Zr(OH)_4$	Zirconium hydroxide
ZrO_2	Zirconium dioxide
$ZrOCl_2 \cdot 8H_2O$	Zirconyl chloride octahydrate

LIST OF SYMBOLS

°C	Degree Celsius
EU/mL	Endotoxin Units
f	frequency of alternating current signal
ω	angular frequency
E	potential
E_{corr}	corrosion potential
I	current
i	current density
i_{corr}	corrosion current density
i_{crit}	critical current density
ppb	parts per billion
R_{hf}	resistive component at high frequency
R_{lf}	resistive component at low frequency
R_{ox}	oxide resistance
R_p	polarisation resistance
R_s	solution resistance
C_{ox}	oxide capacitance
Y_{hf}	constant phase element at high frequency
Y_{lf}	constant phase element at low frequency
T	temperature
t	time
Θ	Bragg's angle
λ	X-ray wavelength
K	Scherrer constant
L	particle size

1 INTRODUCTION

Titanium (Ti) and its alloys are the most common metallic biomaterials used to manufacture dental or craniofacial implants (1). Ti has been selected as the material of choice due to its predictable and largely favourable interactions with biological tissues or fluids, together with its excellent corrosion resistance conferred by the presence of a stable passive oxide surface. For dental implant applications, the most commonly used grades of Ti are commercially pure (CP) ASTM Grade 2 or Grade 4. However, on occasion enhanced mechanical properties are required, such as for small diameter dental implants ($\leqslant$ 3.5 mm) or patients exhibiting parafunctional (high loading) masticatory habits. In these circumstances, fatigue fracture of CP Ti implants is considered a risk which limits clinical applications (2, 3).

As a consequence of the clinical need to use small diameter dental implants, Ti alloys with enhanced mechanical properties are being sought. The alloy of Ti most often used is Ti6Al4V (ASTM Grade 5), which possesses enhanced mechanical properties compared with CP Ti whilst maintaining excellent surface passivity (1). However, concerns have been raised regarding the constitutional elements, Al and V, which may be released *in vivo* and have been associated with local and systemic tissue responses (4, 5). Alternative Ti alloys that are V and/or Al free have been identified and contain elements that are considered as being less biologically significant, such as Zr, Nb, Ta, and Pd (2). Recently new TiZr binary alloys have attracted attention and have been demonstrated to

provide improved mechanical properties without deteriorating corrosion resistance and short-term biocompatibility when compared with CP Ti (2).

It is widely recognised that the degradation of Ti implants *in vivo* is inevitable, and the deterioration of implant surfaces in physiological environment is often a slow and continuous process (6). Elevated levels of Ti have been reported both locally and systemically in subjects that have implants that have not been subjected to obvious mechanical damage (7-9). Ti species (both in oxidation and metallic states) have been found locally accumulated in the peri-implant soft tissues (7, 9), and systemically disseminated in body fluids (serum and urine) and distant organs (8, 10-12). It has been shown that Ti can be found in tissue fluids bound to biomolecules that are involved in cationic transport and in blood, Ti has been shown to be predominantly bound to serum transferrin (8).

The identification of Ti ions bound to biomolecules, coupled with the size and chemistry of Ti degradation products found in many peri-implant environments which suggest they have not been generated through wear, has implicated corrosion as a mechanism leading to metal release *in vivo*. Therefore, more comprehensive studies are required for mechanistic understanding of the complex interplay between the metal surface and biological environment. In addition, *in vivo* metal release has been demonstrated to induce unfavourable local and systemic host responses, therefore it is of vital importance to characterise both physical and chemical forms of metal degradation products and how they can be manifested by exposure conditions in simulated physiological environment.

It has been identified that inflammation, associated with infiltration of immune cells into peri-implant tissues, can act to modify the corrosion resistance of Ti (13). Studies have reported that immune cells such as macrophages and neutrophils can increase corrosion of Ti associated with the cellular generation of reactive oxygen species (ROS) (14, 15). Many studies have reported that H_2O_2, a type of ROS species, significantly enhances the corrosion of Ti (16-22). However, there is a great variation in the levels of H_2O_2 exposure from the *in vitro* tests (17-21, 23), which are significantly higher than its physiological level (24, 25). Additionally, it has been reported recently that albumin, the most abundant protein in blood plasma (26), synergistically enhances the corrosion of Ti in the presence of H_2O_2 (17, 27). However, there is a lack of mechanistic understanding on the action of these two species, in combination.

This thesis considers the current literature and addresses experimentally how differences in peri-implant environments that are not usually explored in pre-clinical corrosion tests set by relevant ‘Standards’ will affect the corrosion behaviour of Ti6Al4V and TiZr alloys. Despite Zr being a common element used to manufacture biomedical implants (28, 29), its corrosion behaviour in physiological environments is poorly understood. The corrosion of Zr is therefore characterised to help interpretation of the findings from studies on TiZr binary alloys.

2 LITERATURE REVIEW

2.1 Ti and its alloys as dental implants

2.1.1 Commercially pure (CP) Ti and Ti6Al4V

The American Society for Testing Materials (ASTM) endorsed 31 Grades of Ti and its alloys, among which 23 Grades are classified as biomedical materials. Manufacturers routinely use 6 different Ti-based biomaterials to fabricate dental implants, namely commercially pure (CP) Ti Grades 1-4 and Ti6Al4V Grade 5 as well as Ti6Al4V extra low interstitial (ELI) (30). CP Ti Grades 1-4 refer to the unalloyed pure Ti which contain trace elements of carbon, oxygen, nitrogen and iron, and can be distinguished by variation in oxygen concentrations (Table 2-1) (30). Ti6Al4V is classified as Grade 5 which is commonly used in orthopaedic applications and, albeit less commonly, used for dental implants, for instance Axiom® (Anthogyr, Sallanches, France) (31). The mechanical and physical properties of Grade I-IV and the Ti6Al4V alloys are listed in Table 2-2 (30, 32).

Ti has a close packed hexagonal phase (hcp, α) at room temperature and body centred cubic phase (bcc, β) at high temperature with a transformation temperature at around 883 °C (33). Alloying elements are categorised into 1) α stabilisers including Al; 2) β stabilisers including V and Fe; and 3) neutral stabilisers including Zr. CP Ti grades have structures consisting of α phase in equiaxed grains at room temperature. Ti6Al4V contains both the α stabiliser Al and the β stabiliser V and therefore contains a combination of α+β phases. The microstructure of Ti6Al4V can be modified by heat treatment and by its

thermomechanical processing history. For example, the microstructure of Ti6Al4V can be fully lamellar, consisting of laths of alternating α and β phases, or composed of fully equiaxed α grains, or composed of a ‘bimodal’ structure consisting of equiaxed primary α grains and transformed β depending on the processing history (34).

Table 2-1. Composition (wt%) of CP Ti and Ti6Al4V alloys (30).

	N	C	H	Fe	O	Al	V	Ti
CP Ti Grade 1	0.03	0.01	0.015	0.02	0.18	-	-	Bal.
CP Ti Grade 2	0.03	0.01	0.015	0.03	0.25	-	-	Bal.
CP Ti Grade 3	0.0.3	0.01	0.015	0.03	0.35	-	-	Bal.
CP Ti Grade 4	0.03	0.01	0.015	0.05	0.40	-	-	Bal.
Ti6Al4V ELI	0.05	0.08	0.012	0.10	0.13	5.5-6.5	3.5-4.5	Bal.
Ti6Al4V	0.05	0.08	0.015	0.30	0.2	5.5-6.75	3.5-4.5	Bal.

Table 2-2. Mechanical properties of commercially pure Ti and Ti6Al4V (30, 32).

	Modulus (GPa)	UTS (MPa)	Yield Strength (MPa)	Elongation (%)	Density (g/cc)	Phase
CP Ti Grade 1	102	240	170	24	4.5	α
CP Ti Grade 2	102	345	275	20	4.5	α
CP Ti Grade 3	102	450	380	18	4.5	α
CP Ti Grade 4	104	550	483	15	4.5	α
Ti6Al4V ELI	113	860	795	10	4.4	α+β
Ti6Al4V	113	930	860	10	4.4	α+β

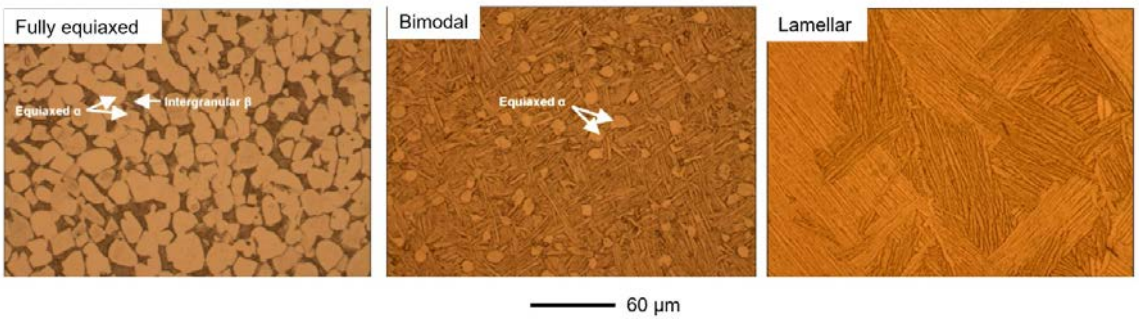

Figure 2-1. Different microstructures of Ti6Al4V alloys obtained by thermomechanical processing histories with variation in forging temperature and subsequent heat treatment and cooling rates. Figure taken from (34).

2.1.2 TiZr binary alloys

TiZr binary alloys have been recently developed for clinical usage and are intended to substitute CP Ti particularly for small diameter implant applications. Zr is in the same periodic group as Ti and possesses the same crystal structure with similar chemical properties (35). Zr is considered as a neutral stabiliser and has complete solubility in both phases of Ti. From the TiZr phase diagram (36), it can be seen that Zr reduces the melting point of Ti and slows the speed of phase transformation from β to α of Ti (33).

As-cast structures of TiZr alloys containing 10, 20, 30, 40 wt% Zr additions are shown in Figure 2-2. All TiZr alloys were in hcp α phases exhibiting some lath-like martensitic features (37). As the Zr addition increases, the number of acicular martensitic structures increases which is probably caused by a reduced martensitic transition temperature (38). The microstructure of Ti-10Zr is characterised in the form of packets of martensite, consisting of colonies that are resolvable optically and belong to the same variant of orientation relation. Similar characteristics are found in Ti-20Zr and Ti-30Zr but with further increase in solute (decrease in martensitic transition temperature) the martensite colony size decreases until the colonies totally degenerate to individual platelets at a sufficient solute concentration (38), as shown in Ti-40Zr. Complete solubility of Zr in Ti is expected to increase the mechanical properties of Ti by solid solution strengthening (35). Zr alloying additions in Ti have been shown to result in significantly better mechanical properties, such as increased elongation, hardness, flexural strength and fatigue strength (39). It can be seen from Figure 2-3 that the hardness and tensile strength can be increased by the addition of

Zr by over two-folds. Commercial TiZr alloys, for instance Roxolid® (13-17% Zr), have been shown to provide a 40% increase in tensile strength and 13%~42% increases in fatigue endurance level compared with that of cold worked CP-Ti Grade 4 (2).

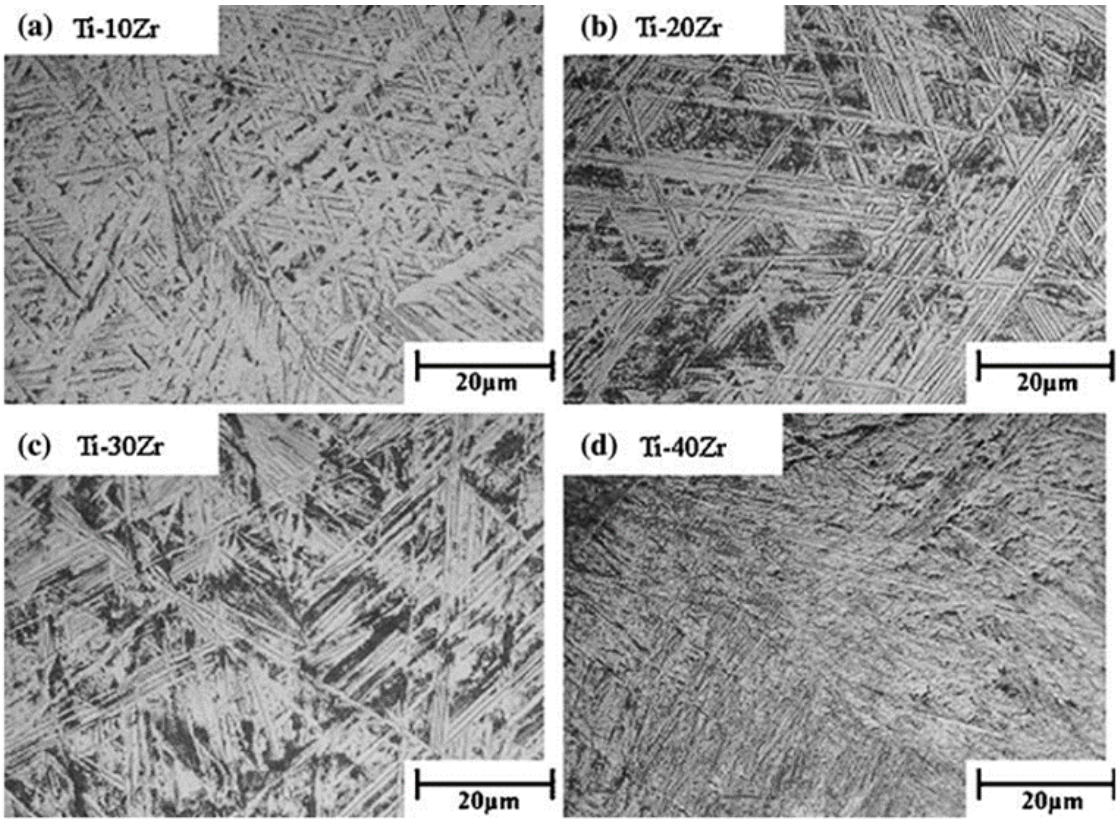

Figure 2-2. Optical micrographs of (a) Ti-10Zr; (b) Ti-20Zr; (c) Ti-30Zr; (d) Ti-40Zr. The 10, 20, 30, 40 refer to at% of Zr in Ti. Figure taken from (37).

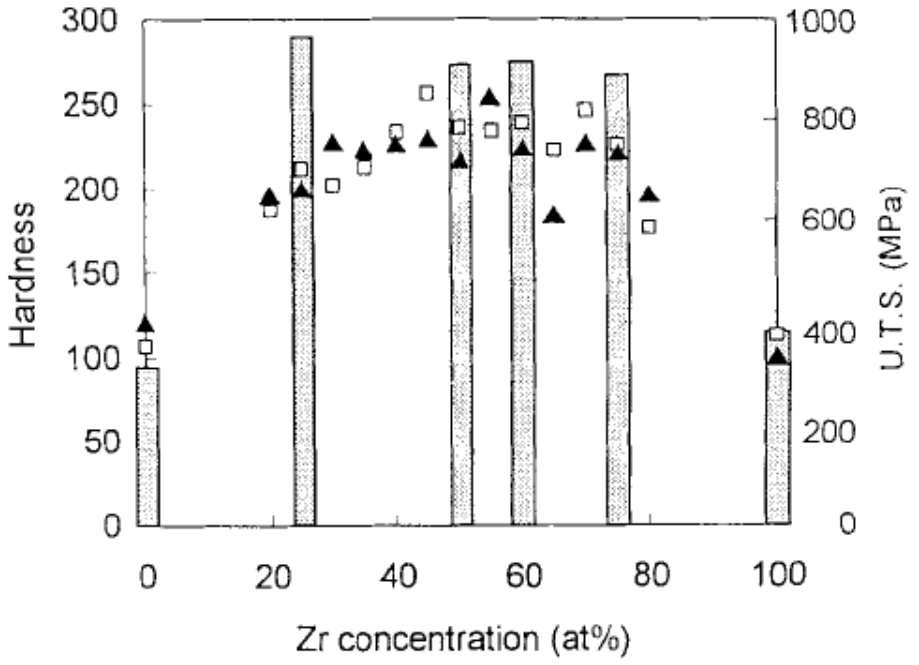

Figure 2-3 Vickers hardness and ultimate tensile strength (U.T.S) of TiZr alloys containing 0, 25, 50, 60, 75 and 100% of Zr. Symbols square and triangle are indicating hardness of the alloys as cast and as homogenised, respectively. Figure taken from (35).

2.2 Corrosion of Ti and its alloys in *in vivo* conditions

2.2.1 General corrosion

Ti spontaneously forms a stable oxide surface layer on exposure to air (40). When the oxide layer forms, the metal is 'passivated' and the rate of corrosion is significantly reduced by the presence of the protective surface oxide film (41). It has been found that the oxide layer on Ti implant surfaces prepared by standard clinical practices (machining, ultrasonic cleaning and sterilization) predominantly consists of TiO_2 with a thickness of 2-6 nm (42). Similarly the passive film found on Ti6Al4V is predominantly TiO_2, but also contains Al as Al_2O_3 however no evidence has been shown for V(43). The air-formed oxide

film on the TiZr alloy surface has also been characterised and it was suggested that a preferential air-oxidation of Ti occurs relative to Zr (44).

General corrosion refers to the dissolution of passive films i.e. the rate of ion transfer through the film, as well as the stability of the film against dissolution (45). The nature and stability of the passive film can be affected by the composition of the electrolyte, the redox conditions (e.g. free radicals and reactive oxygen species), the exposure time and the temperature (45).

Ti and its alloys can be considered as some of the most corrosion resistant biomaterials due to the high stability of TiO_2 in many electrolytes. However, Ti oxide surface film thickness and its composition are subjected to change when they are in contact with tissues and body fluids. It has been reported that the oxide film continues to grow after implantation (46), and studies have shown that the thickness can increase from 5 nm up to 200 nm following 6 years of implantation (47). One hypothesis for the increasing oxide film growth is attributed to interaction with Reactive Oxygen Species (ROS) including H_2O_2, which are produced by immune cells that infiltrate the peri-implant tissue (21, 48), via complexation reaction with Ti and its oxides (16-22). Oxide composition has been reported to have changed in several studies. *In vivo* observation of the interface between human tissue and Ti-implant have shown incorporation of calcium phosphate into the oxide film TiO_2 (46) and this has also been seen in *in vivo* studies where Ca and P were detected on the TiO_2-electrolyte interface after the first hour of exposure in simulated body fluid (SBF) at 37 °C (49).

2.2.2 Localised corrosion

Localised corrosion is typically initiated by inhomogeneities, either in the material or in the surrounding environment (45). A type of localised corrosion is pitting corrosion, which is caused by local dissolution of the metal and formation of cavities surrounded by an intact passivated surface (50). Ti and its alloys show very high pitting resistance in chloride containing environments, with pitting potentials up to 10 V (45). Therefore, it is unlikely for pitting corrosion of Ti to occur under physiological conditions where the potential is typically <1 V (45). However, metastable pitting of Ti has been reported by Burstein et al. in simulated physiological solutions where localised passivity breakdown below the pitting potential but with no permanent propagation of pits. It has also been shown that increasing temperature increases events of metastable pits and proteins such as albumin have been reported to stimulate the nucleation of the pits (51, 52). Although these metastable pits do not cause complete deterioration of the passivity, it should be noted that metal released from Ti implants is routinely detected in clinical samples (45).

Zr is susceptible to pitting attack in halide ion-containing environments such as Cl^- (53, 54). The effect of Cl^- concentration on the pitting potential of Zr, based on several electrochemical methods, has been illustrated by Equation 2-1 (55)

$$E_p\ (V_{SCE}) = 0.134 - 0.088 \log [Cl^- N] \qquad \text{Equation 2-1}$$

where pitting potential is reduced by increasing the concentration of Cl^-. It is understood that the pitting susceptibility of Zr is increased with increasing temperature and with decreasing pH. Pitting resistance of Zr can be increased

by alloying with other elements such as Ti (54). It has been reported that in the actively growing pits on Zr, a colourless viscous solution or white precipitate could be seen exuding from the corroded area inside the pit, in acidic or neutral basic Cl^- solutions (54). In addition, the formation of black precipitates and gas evolution were observed within the growing Zr pit. The black precipitate was shown to contain α-zirconium i.e. zirconium metal by X-ray analysis, and the evolution of H_2 bubbles was speculated to be products from the reaction between the 'bare' surface of the ejected Zr metal particles and water (54, 56).

The mechanism of pitting corrosion of Zr is not well understood and a number of mechanisms have been proposed. The role of chloride ions have been reported specifically, although the evidence available is based on different observation techniques (including scanning Auger electron spectroscopy, X-ray photoelectron spectroscopy, scanning transmission electron microscopy), there is no consensus on whether chloride ions enter the surface oxide film or act only at flaws (57), although, it is likely that material film entry by halides would be much slower than that at flaws (57).

Crevice corrosion is a form of localised corrosion that is closely related to pitting corrosion. It occurs preferentially on the metal surface where mass transfer is limited, such as at surface deposits or in narrow crevices (45). In the confined space such as a crevice, an occluded cell is formed where the metal surface area is exposed to a volume of solution that is stagnated, and aggressive local chemistry can be developed due to restrictions of mass transport (58). When dissolved oxygen, which is used to maintain passivity, is used up in the

occluded cell, and cannot be refreshed by the bulk environment, crevice corrosion can be initiated (58). Dissolution of metal is supported by an O_2 reduction at the surface external to the crevice (58). Released metal ions will hydrolyse in the crevice and produce H^+ ions (Equation 2-2 and Equation 2-3), which cause migration of anions such as Cl^- for electro-charge neutrality. Localised aggressive chemistry can be established containing high concentrations of H^+ and Cl^- ions which favours metal dissolution over repassivation.

$$Ti^{4+} + 2H_2O \leftrightarrow [Ti(OH)_2]^{2+} + 2H^+ \qquad \text{Equation 2-2 (58)}$$

$$Ti^{4+} + 4H_2O \leftrightarrow Ti(OH)_4 + 4H^+ \qquad \text{Equation 2-3 (42)}$$

The resistance to crevice corrosion of Ti is reported to be decreased with increasing temperature and reducing pH. A critical temperature of 65 °C has been reported for the initiation of crevice corrosion of Ti Grade 2 (58). *In vivo*, temperature clearly will not be the critical factor to cause crevice corrosion of Ti, however, low pH values in localised environments has been shown to result in crevice corrosion (45). Figure 2-4 shows evidence of localised attack on cemented Ti6Al4V hip implants where pH values were reduced due to the hydrolysis of metal ions in the crevice formed between bone cement and the implant surface (45, 59). Figure 2-5 shows pitting evidence on the distal end of a retrieved cemented Ti6Al4V stem (60).

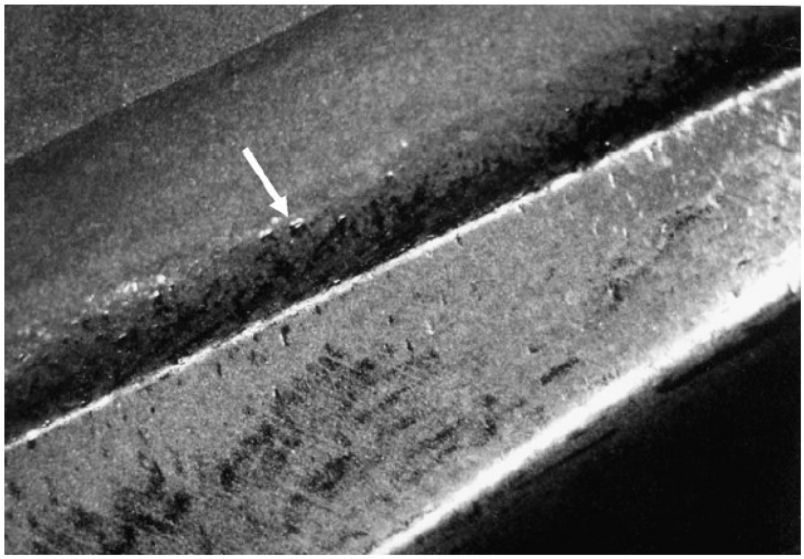

Figure 2-4. Evidence of localised attack (indicated by arrow) on a cemented Ti6Al4V stem hip implant as a result of crevice corrosion (45, 58). Figure taken from (45).

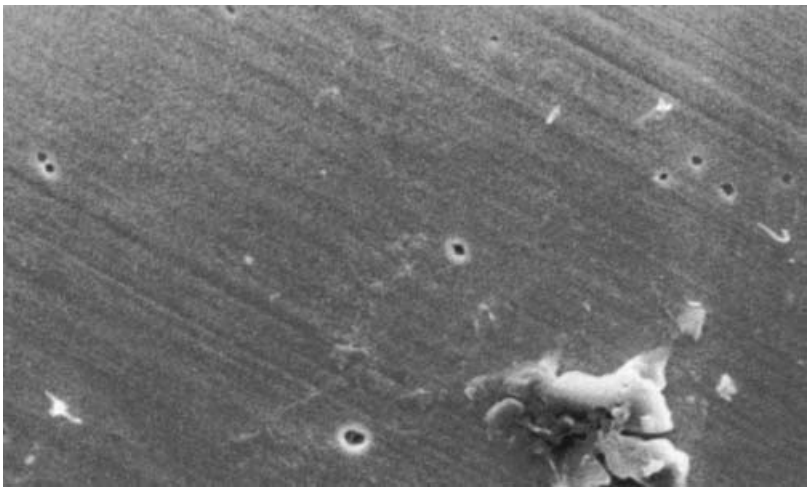

Figure 2-5 Scanning electron microscopy image shows signs of pitting on a retrieved primary cemented femoral Ti6Al4V implant. Figure taken from (60).

2.2.3 Mechanically assisted crevice corrosion

Mechanically-assisted crevice corrosion (MACC) refers to the corrosion damage of two closely pressing surfaces when they are subjected to small amplitude oscillatory motion and corrosion action (45). It should be emphasised that mechanical motion between the two pressed surfaces are in relatively small

scale (e.g. between 1 to 100 µm) such as that encountered at modular junctions of hip implants (61), resulting in progressive rupture of passive films of the metal couple in a crevice environment (45). The two closely fitting surfaces form a narrow crevice. Unpassivated metal will quickly and spontaneously repassivate which consumes O_2 in the crevice solution. Ultimately when free O_2 is depleted, the crevice corrosion condition is readily established where the metal ion concentration is increased and Cl^- ions are attracted for charge balance (62). Aggressive solution chemistry is developed and maintained in the geometrically confined narrow crevice, favouring dissolution of passive films and results in active attack of Ti and bursts of metal dissolution. A schematic diagram for the mechanism of MACC is shown in Figure 2-6.

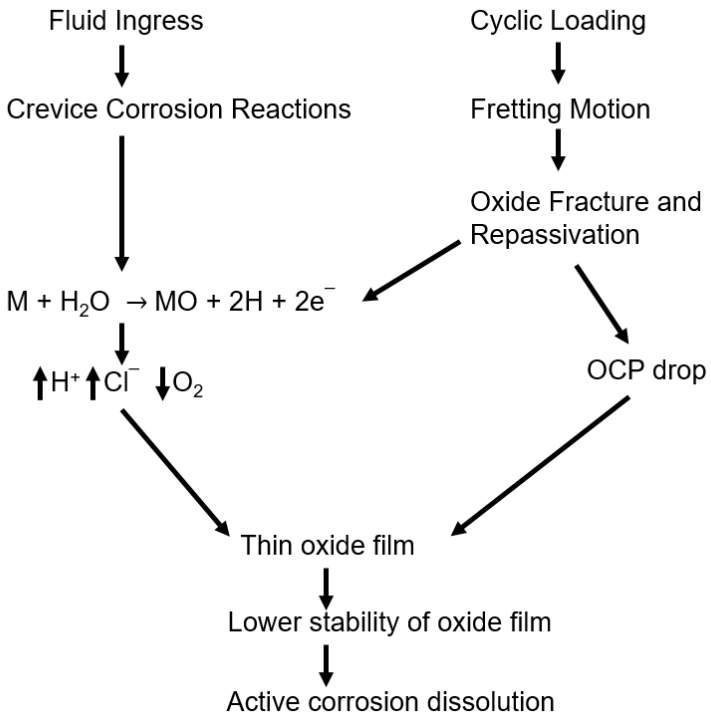

Figure 2-6. Schematic of the Mechanism of Mechanically Assisted Crevice Corrosion (MACC). Figure reproduced from (63).

MACC can drastically alter the corrosion behaviour of a substrate by mechanically disrupting the passive film and significantly increasing its corrosion rate. It should be noted that MACC is different from tribocorrosion, which is defined as conjoint action of mechanical wear and corrosion attack on the metal surface (45). However, the mechanical wear in tribocorrosion occurs on rather small contact areas in two relative large surfaces of metals and the mechanical motion is on a relatively large scale such as the sliding wear motion of pin-on-disc type apparatus (64). The mechanical motion between the two sliding surfaces destroys the passive film however the amplitude of motion is large enough, so that fresh solution can be replenished in the contact environment resulting in rapid repassivation of the surface.

MACC has been identified as an important, but under-explored factor when studying implant corrosion (23). Clinical evidence in the form of retrieved modular Ti alloy implants has associated MACC directly with prosthesis failure (62, 63, 65). Relative motions at the modular connections and consequent abrasive loss of the passive oxides facilitate the MACC conditions (65). Gilbert et al., showed that approximately 16-35% of 148 retrieved orthopaedic implants exhibited moderate to severe fretting corrosion at head-neck tapers in both mixed (Co-Cr/Ti6Al4V) and same (Co-Cr/Co-Cr) stem-head hip implants (62). Rodrigues et al. reported that retrieved hip implants with Ti6Al4V/Ti6Al4V modular taper interfaces showed evidence of severe corrosion with signs of etching, pitting, preferential dissolution of β phase of Ti6Al4V and as well as hydrogen embrittlement induced surface cracking as a result of MACC (Figure 2-7) (66). Cemented Ti6Al4V Furlong stem hip implants were also reported to

be degraded possibly under MACC mechanism where micro-movement between the stem and cement initiated the progressive abrasion of the protective oxide layer followed by a subsequent MACC cascade (60). Therefore the mechanical integrity of the oxide films that form on these alloys is critical for implant survival and long-term stability (65).

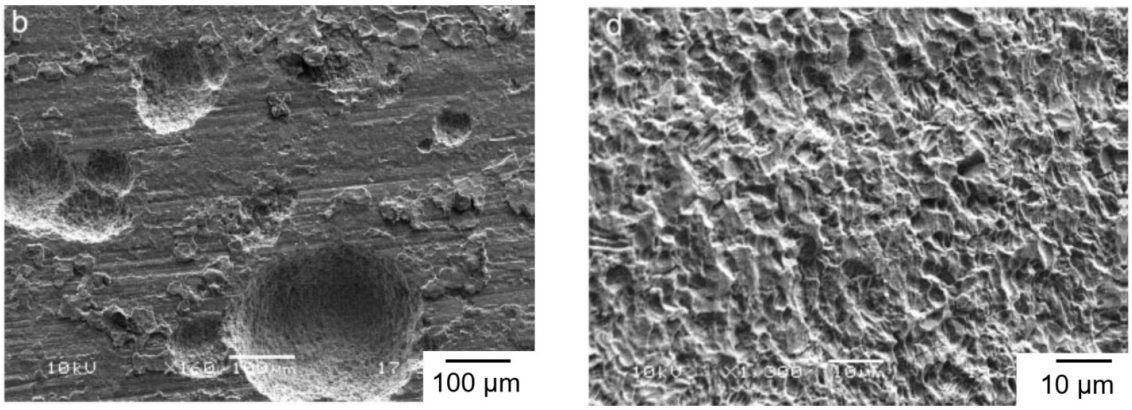

Figure 2-7 SEM images taken on retrieved modular Ti6Al4V hip implants showing signs of localised corrosion with (a) large and deep pits; signs of general corrosion with (b) crystallographic etching of microstructure with etched α grains and selective dissolution of β phase at the modular female taper interfaces as a result of MACC. Figures taken from (66).

2.3 *In vitro* corrosion studies of Zr, Ti and its alloys

2.3.1 Introduction

The physiological environment into which metallic implants are placed varies according to site, time and from patient to patient. However, the peri-implant environment should always be considered to be a complex system which contains inorganic ions, amino acids, protein, living cells and sometimes bacteria (15). This environment interacts directly with the implanted device, and its contents are frequently associated with implant degradation during service. The individual or combined effects of biologically relevant species on corrosion

of Ti as well as binary TiZr alloys are frequently reported. Factors mediating corrosion that have been studied include; F^- ions which can be found in oral hygiene products (67, 68), pH (5, 22), H_2O_2 which can be produced during inflammation (19), tissue fluid proteins such as albumin (69, 70), lipopolysaccharide (LPS) a constituent of Gram-negative bacteria which can be found in implant biofilms (71), inflammatory cells such as macrophages (14) and acidogenic and peroxide producing bacteria (72). In the following sections, the effect these factors that have been suggested to modify and mediate the corrosion of Zr, Ti and its alloys *in vivo*, are reviewed and discussed.

2.3.2 The effect of environmental acidity, chloride and hydrogen peroxide

2.3.2.1 Effect of hydrochloric acid (HCl)

Lowering of pH values could be expected during the inflammation process, as a result of infiltration and activation of inflammatory cells which demands increased energy and oxygen leading to accelerated lactic acid secretion(73-75). Localised acidification could also be expected in the crevice geometry of implants and can be established by crevice corrosion and MACC (section 2.2.3). Retrieved Ti6Al4V hip implants have shown direct evidence of extreme acidification occurring *in vivo* with pH measurements taken immediately on fixture retrieval reported as being as low as 1.7 (59). Local build-up of acidity and chloride ions primarily cause accelerated passive dissolution and/or depassivation and active dissolution of the implant surface. Therefore, HCl is often used to simulate a local occluded cell environment to test *in vitro* the stability of passive films on Ti alloys (44, 76, 77).

Oxide films on Ti are susceptible to destabilization in concentrated reducing acids. Dissolution of air-formed or anodic Ti oxides (TiO_2) has been proposed to either form Ti^{3+} species (e.g. TiOOH) by reducing TiO_2 or direct chemical dissolution to Ti^{4+} species (e.g. TiO^{2+}, Ti $(OH)_3^+$) which would then lead to active dissolution of the bare metal surface and accelerated metal ion release (77). Studies have shown that Ti oxides can be destabilised and chemically dissolved when immersed in deaerated 5 M HCl, as indicated by abruptly decreased open circuit potential (OCP) measurements of CP Ti (Figure 2-8), followed by 'surface activation' where the bare metal surface becomes exposed to the electrolyte with subsequent active dissolution (77). However, such abrupt drops in OCP have shown to be delayed for Ti-50%Zr alloy and such behaviour is not seen for CP Zr (Figure 2-8), which suggests a better resistance to dissolution of Zr oxides in deaerated 5 M HCl (77). As the OCP value of Zr is within the thermodynamically stable range of Zr^{4+} according to the E-pH diagram Figure 2-9 (78), it has been suggested that Zr oxides are kinetically resistant to chemical dissolution (77).

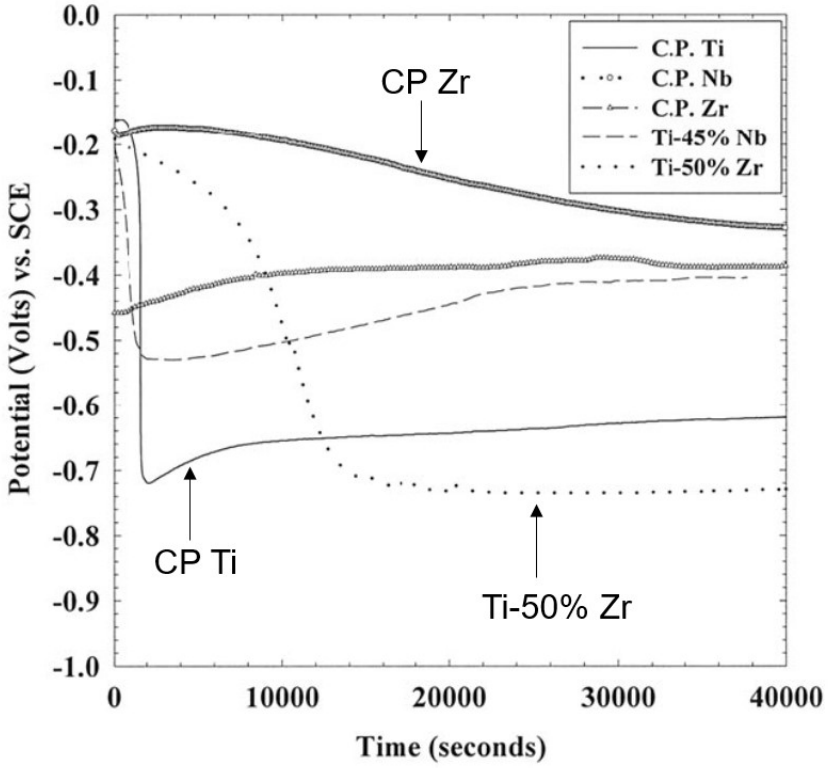

Figure 2-8. Open Circuit Potentials of CP Ti, CP Zr, CP Nb, Ti-45% Nb, and Ti-50% Zr, initially with air-formed oxides in deaerated 5 M HCl at 37 °C. Figures taken from (77).

Dissolution of Ti oxide films has also been shown to increase with a decrease in pH. (77) It was shown that in the concentration range of HCl from 0.1 to 10 M, the higher HCl molarity decreases the time required for surface activation of CP Ti, indicating higher dissolution rates of oxides in the more concentrated HCl solutions. This behaviour can be related to the thermodynamically stable state of Ti (Ti^{3+}) at the relevant potential and low pH (Figure 2-10) (76). For a Ti-50%Zr alloy, it was shown that the OCPs also showed similar features of accelerated ‘surface activation’ with reducing pH, however longer time periods were required, and the minimum molarity of HCl for ‘surface activation’ was also higher, when compared with that of CP Ti (77).

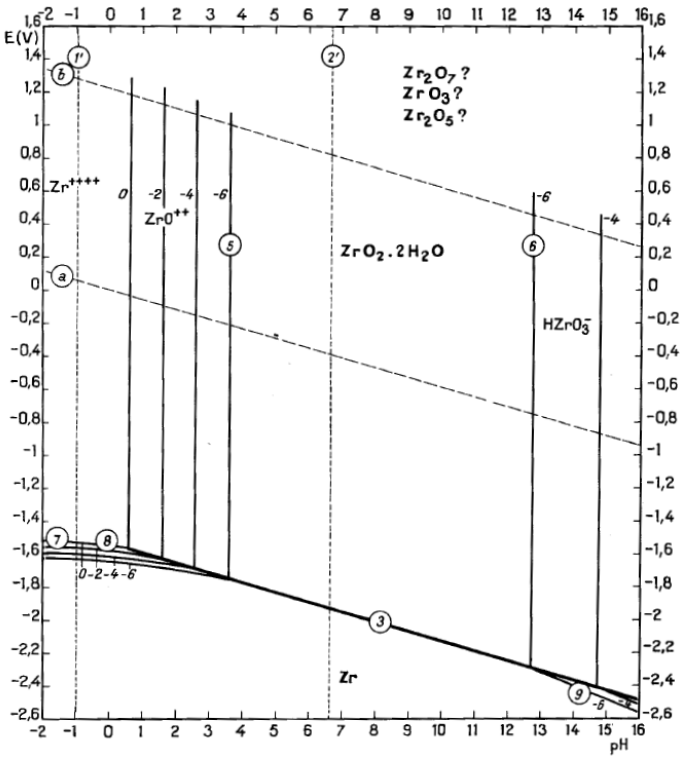

Figure 2-9. Potential-pH (E-pH) equilibrium diagram for Zr-H_2O system at 25 °C. Figure taken from (78).

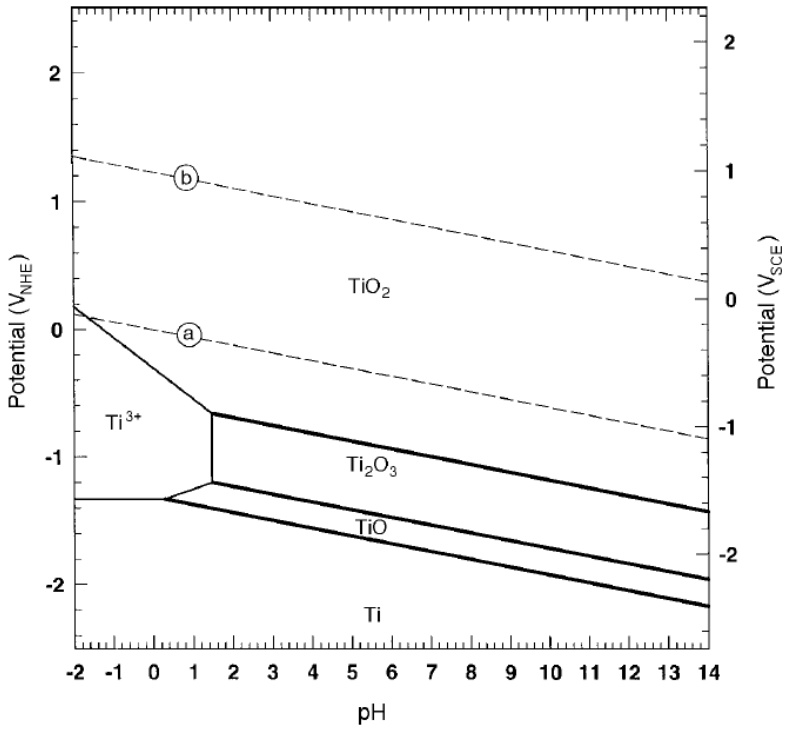

Figure 2-10. Potential-pH (E-pH) equilibrium diagram for Ti-H_2O system at 37 °C. Lines (a) and (b) define the region of water stability. Figure taken from (76).

It has been speculated that the delayed surface activation exhibited by Ti-50% Zr when compared with CP Ti is due to a slower dissolution rate of Zr incorporated within Ti oxides relative to TiO_2 (77). It has been proposed that incorporation of Zr in the Ti oxide may result in an amorphous double oxyhydroxide similar to that found for Mo-Zr, and the oxide film is highly resistant to chemical dissolution because of its thermodynamic and/or kinetic stability where Ti is still active (77).

As a consequence of the 'surface activation' of CP Ti at OCP, the underlying Ti metal surface will be subjected to anodic dissolution in HCl solutions. There is no consensus on whether actively dissolved Ti species exist in the form of Ti^{3+} or Ti^{4+} ions (77, 79, 80). It has been shown that once Ti oxides become dissolved i.e. 'surface activated', the Ti surface undergoes an active/passive transition under anodic polarisation in HCl solution (44). In addition, alloying of Zr in Ti reduces the rate of anodic dissolution, where the net value for critical current density (i_{crit}) of Ti-50% Zr becomes lower than that measured for CP Ti (44). The improved resistance of Ti-50% Zr to active anodic dissolution in comparison with CP Ti has been found not to be attributed to the artefact of a possible enhanced cathodic reaction (44), which promotes passivity such as that observed for Ti-Pd system (81).

2.3.2.2 Effect of hydrogen peroxide (H_2O_2)

Reactive Oxygen Species (ROS) such as hydrogen peroxide (H_2O_2) are produced by immune cells such as neutrophils and macrophages that are found in abundance in inflamed peri-implant tissues (13). Figure 2-11 demonstrates the mechanism of ROS production by phagocytic cells. The generation of ROS

is governed by the NADPH (Nicotinamide adenine dinucleotide phosphate) oxidise complex which is bound to the cell membrane (13). Oxidation of NADPH transfers an electron across the cell membrane and reduces oxygen molecules to superoxide anions. Superoxide anions can further produce more active species such as H_2O_2 by dismutation when the concentration is high enough, otherwise it can be catalysed by oxygen dismutase (82). It was reported that neutrophils, the front line cells in the immune system, can generate significant amounts of superoxide anion with estimated concentrations of 1 M to 4 M in phagosomes and its steady state concentration was estimated to be in µM range as a result of its dismutation to H_2O_2 (83, 84).

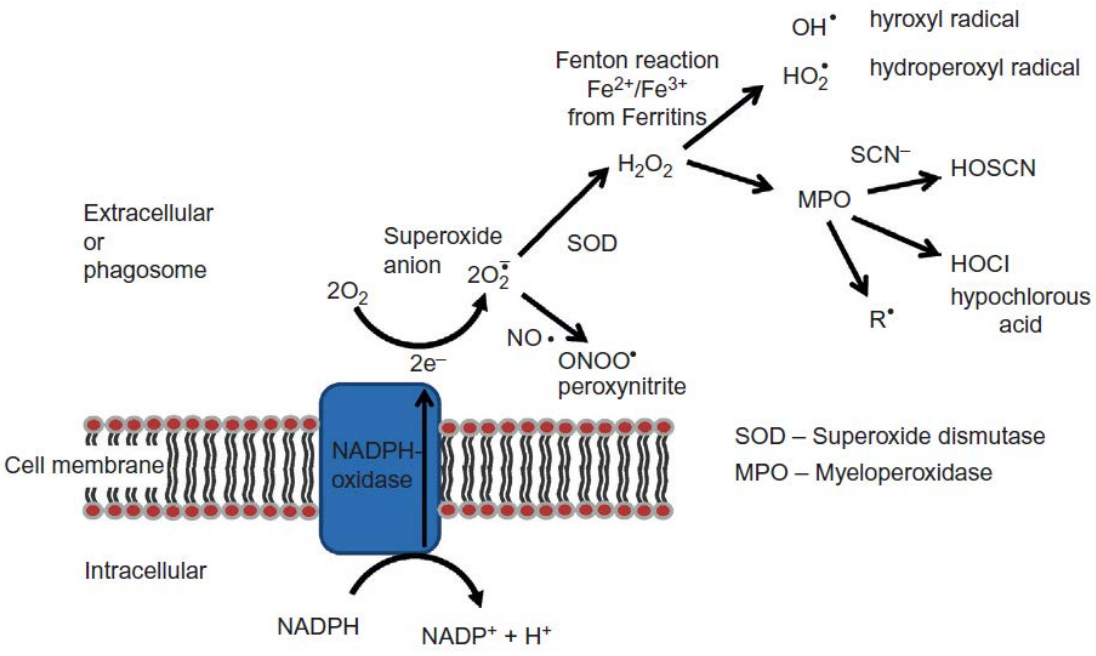

Figure 2-11. Generation of ROS species in mononuclear phagocytic cells. Figure taken from (13).

Due to the nature of the short half-lives of ROS species, and the fact that signal transduction often take place on the subcellular scale over periods of seconds

or minutes, reliable quantitative of ROS detection is difficult and there is a need for detection methods with temporal and spatial resolution (83). An example of spatial variation of H_2O_2 concentration has been shown by the real time mapping of H_2O_2 production across a peroxide producing polymicrobial biofilm. It was shown that concentration of H_2O_2 varied from 31 µM in the bulk electrolyte but increased to 1.6 mM close to the biofilm surface after 8 h (85).

Quantification of the levels of H_2O_2 produced in the peri-implant environment is difficult and there is a great variation of H_2O_2 exposures used in simulated *in vitro* corrosion tests. However, it is accepted that peak concentrations of H_2O_2 can be reached when ROS release is confined in environmental niches, such as sub-cellular phagosomes or extracellularly between and adherent cell and a material surface. H_2O_2 is known as a strong oxidant and acts to modify the corrosion resistance of Ti. Studies that have been carried out to investigate the effects of H_2O_2 on the corrosion of Ti alloys, typically use concentrations ranging from 33 mM to 300 mM of H_2O_2 (17-21, 23).

The redox nature of H_2O_2 means that it can be both oxidised and reduced via the following reactions (78):

$$H_2O_2 + 2H^+ + 2e^- \rightarrow 2H_2O$$ Equation 2-4

$$H_2O_2 \rightarrow O_2 + 2H^+ + 2e^-$$ Equation 2-5

It is expected that H_2O_2 can modify both anodic and cathodic reactions of Ti. DC electrochemical studies have shown that addition of H_2O_2 in 0.9% NaCl

increases OCPs of CP Ti and Ti6Al4V (15, 17), which is dominated by enhanced cathodic reaction rates (17) by Equation 2-5.

Anodic polarisations of Ti also have shown increased passive current densities in the presence of H_2O_2 (27). Furthermore, metal ion release from CP Ti and Ti6Al4V has been shown to be increased with increasing concentrations of H_2O_2 (17-21, 23), attributed to the complexation reaction of Ti (and TiO_2) with H_2O_2 (23, 86). The surfaces morphologies of Ti6Al4V after immersion in saline with addition of different levels of H_2O_2 were observed that the metal surfaces were covered with precipitated corrosion products which seem to be thicker at higher H_2O_2 concentrations (17). Further AFM studies have also revealed preferential attack of the β phase on Ti6Al4V surface by H_2O_2 (17).

Discoloration of Ti surfaces can be observed after incubation in saline with addition of H_2O_2, especially, at acidic pH (18). The discoloration of Ti surfaces is associated with the thickness of oxide films (interference film), and a correlation between discoloration and metal ion release was found for CP Ti (18). Depth profiles using Auger Electron Spectroscopy (AES) on CP Ti specimens after immersion in acidic saline solutions with addition of 150 mM H_2O_2 resulted in10 times higher oxide thicknesses than that of specimens without the presence of H_2O_2 (18), indicating the role of H_2O_2 in enhancing oxide film growth (21).

The surface roughness and topography of CP Ti have also been shown to be modified in the presence of H_2O_2 (22). It was found that surface of Ti after incubation in artificial saliva with the addition of H_2O_2 becomes rougher and

more irregular compared with that of Ti surfaces incubated in artificial saliva alone. It has been further suggested that the increases in surface roughness reached a plateau after 3 days of immersion, during 9 days of incubation period (22).

The interaction between H_2O_2 and surface oxides of Ti has also been studied by electrochemical impedance spectroscopy (EIS). It was observed that the polarisation resistance (R_p) was significantly reduced following introduction of H_2O_2 into an electrolyte of phosphate buffered saline (20, 87), resulting in an enhanced dissolution/oxidation rate. Pan et al. proposed a double oxide film structure of CP Ti following the interaction with H_2O_2, which contains a thin barrier-type of inner layer and porous outer layer (19-21).

To date, the effect of H_2O_2 on the corrosion of Zr is poorly characterised. Interactions between ZrO_2 and H_2O_2 have been investigated by measuring metal ion release and the potentiodynamic behaviour of a Zr_2Sn alloy in artificial saline with and without addition of H_2O_2 has been studied. It was found that in the presence H_2O_2 in artificial saliva, the passive current densities for (thermally-treated) Zr_2Sn alloy (whose oxide was composed of almost stoichiometric ZrO_2) was approximately two magnitudes lower than that of CP Ti and the metal ion release was at least 200-fold less than that of CP Ti (88). Therefore, it can be expected that the interaction between ZrO_2 and H_2O_2 is different from the observation of its complexation with Ti (and Ti oxides).

2.3.3 Effect of proteins

2.3.3.1 Effect of albumin

The metal implant surface is exposed to blood and tissue fluids following implantation which result in rapid adsorption of proteins including albumin onto their surface. Albumin is the most abundant protein (4.2 – 5.3%) in blood plasma and extracellular tissue fluid (26), and is known to interact with metal oxides. Rapid adsorption of albumin onto Ti surfaces has been characterised using infrared spectroscopy and XPS (89, 90). Furthermore, using ^{125}I radio labelling, it was found that albumin absorbs on oxidised Ti surface from the early stages of its immersion with the majority of adsorption taking place within the first few minutes (91).

It is generally agreed that albumin inhibits cathodic reactions of Ti as well as Zr by adsorbing onto the metal surfaces and covering the reaction sites and/or blocking the mass transport of dissolved O_2 (17, 70, 92-95). Many studies have been carried out to investigate the effects of albumin on the corrosion of Ti (92-99). In contrast only a small number of investigations have considered ZrTi binary alloys (100) and CP Zr (70). However, conflicting results are reported. It has been claimed that albumin can increase (17, 92, 96), decrease (94, 95) , or have no effect (98, 101, 102) on the corrosion of Ti. Similar contradictory results were also found for other metallic biomaterials such as stainless steel (103, 104), Mg and Fe (105). The influence of albumin on the electrochemical behaviour of Zr was studied by Wang et al. It was found that albumin increases the corrosion rate and reduces pitting potentials of Zr in PBS attributed to its adsorption and complexation with the metal surface (70). However, a further

study by Mareci et al. reported that albumin seems to act as a protective film and prevent attack of halide ions on ZrTi alloys in a medium of acidified artificial saliva (100).

Metal-protein interactions are generally attributed to two effects: adsorption and chelation. In the case of adsorption, dissolution of Ti has shown to be inhibited by a layer of adsorbed albumin film (94, 95). In the case of chelation, dissolution of Ti can be enhanced by formation of soluble metal-protein complexes (92, 106, 107). It was further found that protein-induced metal ion release is a time dependent process and is determined by adsorption and desorption of metal-protein complexes, which is a rate limiting process and depends on several factors such as the ionic strength and the protein concentration (108, 109).

Contradictory evidence exists in the scientific literature regarding the role of albumin on the corrosion of Ti and Zr alloys. Further studies are required to be carried out to understand these complex systems since both surface properties and the behaviour of the adsorbed protein are likely to change over time (106).

2.3.3.2 The effect of albumin and hydrogen peroxide (H_2O_2)

Whilst the effect of albumin and H_2O_2 on corrosion of Ti (and its alloys) have been studied individually, limited work has considered the effects of exposures to the combination of species on corrosion/oxide film properties of Ti. It is known that exposing Ti surfaces to H_2O_2 modifies, subsequent interactions with adsorbed proteins such as albumin: Nagassa et al. showed H_2O_2 pre-treated Ti, enhanced the adsorption of plasma proteins to its surface, and the efficiency of

protein adsorption was correlated with surface roughness (110). Sousa et al. demonstrated differential binding affinities of albumin to a sputtered TiO_2 surface when compared with a TiO_2 surface that had been modified by H_2O_2 (89). It was shown that the TiO_2 surface treated by H_2O_2 absorbed less albumin but with a higher work of adhesion than that of the sputtered TiO_2 surface, which was attributed to its more hydrophilic surface properties (89). It was further observed that exchangeability of the adsorbed albumin changed with time: After 24 h the adsorbed albumin molecules on the H_2O_2-treated TiO_2 surface were less exchangeable than those adsorbed on the sputtered TiO_2 surface, however, after 72 h nearly all the adsorbed albumin molecules effectively exchanged with other albumin molecules (89). This observation suggests that longer times are needed for exchange of albumin molecules adsorbed on surface of H_2O_2-TiO_2 complexes and this should be accounted for in experiments investigating the influence of albumin on corrosion behaviour.

The effect of albumin and H_2O_2 on the corrosion of Ti6Al4V has been studied directly, by measuring metal ion release after long-term incubations (17). Yu et al. showed that the rate of metal ion release was significantly higher in the presence of both albumin and H_2O_2 than in the presence of either species alone (17). However, short-term electrochemical studies showed that albumin inhibited both anodic and cathodic reaction rates possibly due to an adsorption effect (17). The contradictory observation can be partially explained by a proposed mechanism illustrated by the Evans diagram reproduced in Figure 2-12. It can be seen that the anodic and cathodic reaction of Ti6Al4V in physiological saline (solid black line) gives an intersection of point A which

defines E_{corr} and i_{corr}. Addition of H_2O_2 are proposed to increase both the anodic and the cathodic reaction of Ti6Al4V (dashed blue line), with an intersection of point C in the passive region giving a higher E_{corr} and higher i_{corr}. Addition of albumin and H_2O_2 slightly reduces the anodic reaction and supresses the cathodic reaction taking the potential into an 'active' region of Ti, with the interaction point of D, leading to much higher value of i_{corr}.

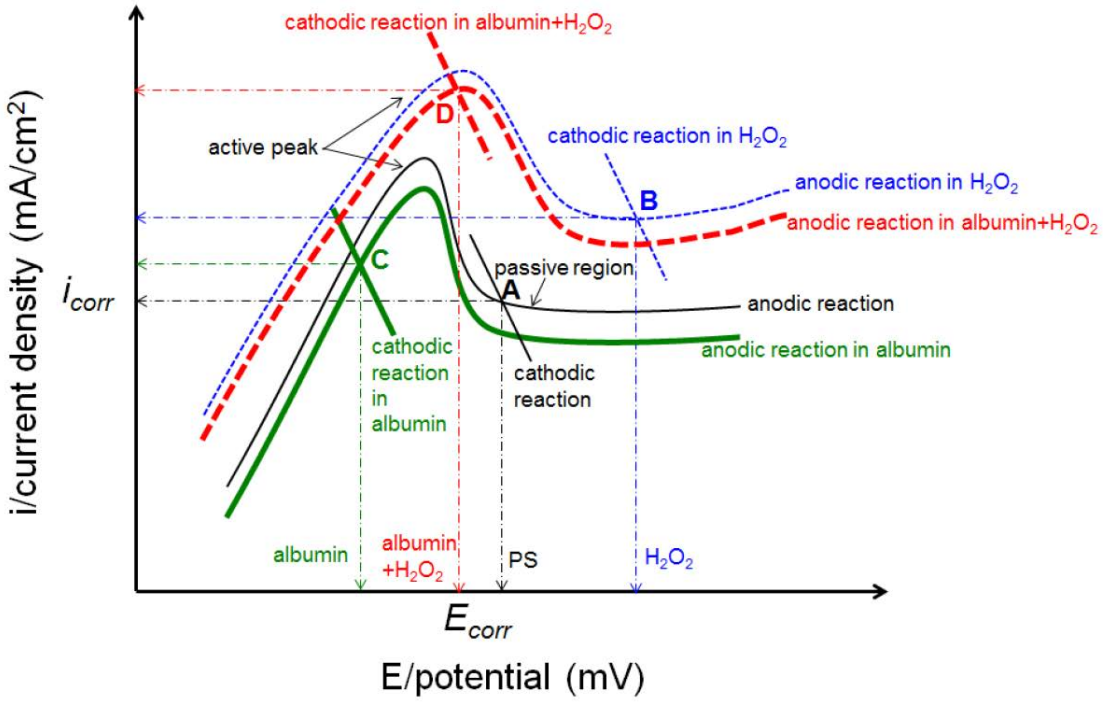

Figure 2-12. Schematic Evans diagram to illustrate effect of H_2O_2, albumin and combination of the two species on corrosion potential (E_{corr}) and corrosion current density (i_{corr}) of Ti6Al4V in physiological saline (0.15 M NaCl) (17).

2.3.4 Effect of cellular induced corrosion

Upon insertion, the metal implant comes directly into contact with the host tissues. Initial implantation is associated with inflammation with rapid infiltration of inflammatory cells dominated by neutrophils. In the long term implants can often be associated with chronic inflammation amongst which macrophages can

be abundant (111). Macrophages are innate immune cells that arise from monocytes and are responsible for phagocytosis of microbes and debris during which ROS species are generated (13). Macrophages can be differentiated into different functional phenotypes including a pro-inflammatory M1 state and a tissue-repair M2 state (13, 112). M1 macrophages differentiate in order to counter an external challenge such as microbes and if present, implant debris (113). In the more advanced stages of inflammation, the macrophage population tends to shift towards an M2 phenotype which suppress pro-inflammatory cytokines and has a functional focus on tissue remodelling and repair (113). M1 and M2 phenotypes of macrophages are associated with differential ROS release. In theory M1 macrophages are more active and tend to trigger an enhanced bactericidal response which involves enhanced ROS production when in contact with pathogen whereas M2 macrophages are associated with functions of wound healing and tissue reconstruction accompanied by reduced ROS production (114).

Osteoclasts (OC) are multinucleated and are responsible for bone resorption. They have long been debated to corrode implant surfaces(115). Osteoclasts are often identified by their expression of tartrate-resistant acid phosphatase (TRAP) (116), which is essential for their function of bone resorption, and are reported to produce hydrochloric acid (117) and ROS species (118). It has been demonstrated that *in vitro* osteoclast precursors can grow and differentiate towards mature osteoclasts on the Ti surface, which are able to directly cause corrosion of Ti, as detected intracellularly (115). It was suggested that functional

OC can generate a low pH in resorption compartment, which could destabilise the oxide film and cause corrosion.

The effect of inflammatory cell-induced corrosion is increasingly studied, introducing a new and critical element on interaction between the implant and host environment which has not been previously fully appreciated. Limited work has been carried out on macrophages induced corrosion of Ti alloys (14, 119). Mu et al. showed Ti metal ion release was increased by the presence of macrophages and further accelerated by the presence of macrophages with phagocytosed particles (14). ROS species such as superoxide anions and H_2O_2 are known to accumulate in the micro-crevice environment between the adhered cell the metal surface, promoting dissolution of Ti metal surface(14). In contrast, Lin et al. reported that cultures of Ti6Al4V with macrophages resulted in reduced corrosion (119). However, it was pointed that longer testing times were needed to better approximate *in vivo* conditions. To date, no work has been carried out comparing the effects of macrophage phenotype, associated with different stages of peri-implant inflammation, on the corrosion of Ti and TiZr alloys.

2.4 Clinical failure and biological impact of implant metal release

2.4.1 Failure of Ti dental implants

The failure of dental implants due to biological causes, for instance osseointegration manifested implant mobility, either occurs early (< 6 months) following initial surgical implantation, or after several years of successful use as

a consequence of the development of chronic peri-implant inflammation. Early dental implant failures, are associated with a failure of osseointegration (120) which can be attributed to post-surgical infection, or impaired bone healing that is influenced by the host response and by surgical variables (121, 122). In contrast, chronic biological failures of osseointergrated dental implants, such as peri-implant inflammation, are often associated with biological responses, which are not well-defined and remain poorly understood. There is however consensus that the prevalence of peri-implant inflammation is high, affecting up to 48% of dental implants (123). Peri-implant diseases are classified as either peri-implant mucositis or peri-implantitis. Peri-implant mucositis refers to establishment of a reversible inflammatory lesion in the peri-implant mucosa (9). Peri-implantitis is diagnosed with an inflammatory response around an implant, including soft-tissue inflammation and progressive loss of supporting bone (124, 125), which can further lead to failure of osseointegration and loss of the implant. Peri-implant implant inflammatory diseases are understood to be driven by the host-immune response to microbial colonisation of the implant surfaces, however there is increasing evidence that implant derived products act as immunomodulators and may influence the persistence of inflammation (116).

2.4.2 Release and toxicity of metal degradation products

Interactions between metallic biomaterials and local biology environment should always be reminded that are in two-ways: corrosion causes biology and biology causes corrosion (13). When the implanted device is conformed to degrade in the complex physiological environment, degradation products generated will

adversely cause potential damaging/toxic effects on human tissues and/or cells. The tissue reaction can be anything ranging from mild response e.g. discolouration of the surrounding tissue to a severe response such as inflammatory reactions resulting in pains and osteolysis (64). The biological risks of metal ion release include wear debris, free metal ions, inorganic metal salts or oxides, and complexes formed between metallic species and organic biomolecules (45).

2.4.2.1 Metal ions, debris and wear particles

In many cases, metal ion release is related to the combined mechanical and chemical effects such as MACC (see section 2.2.3). Metal ions can be released through remaining oxide films and furthermore when surface oxide films are disrupted by mechanical wear, where the amount of release is governed by regeneration of oxide films (126). Toxicity of metal ions is associated with their subsequent interaction with biomolecules in extracellular environment (126). Released free metal ions can be transformed depending on their solubility (1). It was reported that Ti ions are highly reactive and once released it can immediately combine with a water molecule or an anion near the ion to form oxide, hydroxide or inorganic salt, which are less toxic compared with that of metal bonded biomolecule complexes (126) or Ti ion bonded serum transferrin in blood (8).

Metal debris and wear particles have been identified in small micron and sub-micron size from retrieved peri-orthopaedic prosthesis (59, 127). Particles of corrosion products were found in peri-prosthetic tissue as well as those within macrophages and foreign-body giant cell. As-produced wear particles at the

interface of bone cement and the Ti6Al4V stem implant became phagocytosed by macrophages, and when a sufficient amount of wear particles is given, macrophages accumulate into granulomas and release inflammatory mediators and stimulate bone resorption with consequent osteolysis and aseptic loosening (59). Whilst release of metal ions and generation of metal debris were identified and have been associated with unfavourable body host responses, both Zr and Ti degradation products are considered to be relatively more biocompatible when compared with those of stainless steel or of CoCrMo alloy (128).

2.4.3 Current understandings of *in vivo* metal degradation

Whilst it has been generally accepted that degradation of metal implants is associated with complexity of chemical and mechanical processes such as tribo-corrosion and MACC, it has been reported that metal degradation products can be generated when the implant devices are not subjected to significant mechanical wear. Addison et al. observed a scattered and heterogeneous distribution of Ti speciation including fine metallic fragments and oxides (both anatase and rutile) in inflamed tissues taken from around failing skin-penetrating Ti BAHA (bone anchored hearing aid) implants (7). The quantities, size and speciation of Ti debris were demonstrated to be pro-inflammatory in nature. The degradation products were proposed to be produced by micro-motion and localised corrosion in surface crevices (7). This observation is also supported by in-situ synchrotron characterisation of dissolving Ti artificial corrosion pits, which simulated the process of localised corrosion such as pitting, and inside the pit cavity metallic Ti fragments and

TiO_2 were found to be generated by purely electrochemical process. Metal fragments were proposed to be generated by localised undercutting process where base metal is undermined during localised corrosion and TiO_2 was produced by reaction of free Ti ions and the electrolyte (129). Therefore, despite concerns over the likely biological effects of released metal ions and debris as a consequence of wear and/or corrosion process, the mechanism underpinning *in vivo* release of Ti ions and particles need to be carefully investigated to understand premature loss of implanted devices.

2.5 Current standards of corrosion testing of biomedical materials

Current ASTM standards on corrosion testing of biomedical materials include electrochemical measurements in standard testing solutions such as 0.9% NaCl, phosphate buffered saline, Ringer's and Hanks (130-134). OCPs, anodic polarisations and cyclic (forwards and reverse) potentiodynamic polarisation are commonly measured in *in vitro* tests of corrosion of metallic biomaterials, to obtain reliable results from controlled methods and enable cross-comparison of the behaviours of different metallic biomaterials to be made (130, 132).

However, extrapolation of such *in vitro* standard testing is often difficult, and may result in underestimation of corrosion that can occur *in vivo* (17). For instance biological factors encountered in peri-implant environment including cells and proteins are not considered in the artificial physiological electrolytes, although reported to modify the corrosion resistance of implant surfaces; standard electrochemical tests are designed to reach conditions that cause severe breakdown of the testing materials (e.g. at very high potentials) that may

not be encountered *in vivo*; degradation *in vivo* is a slow and continuous process however the standard electrochemical testing is often associated with short term periods. Therefore, it is important that the corrosion resistance of metallic biomaterials should not be only assessed using standard short-term electrochemical testing, but factors that mediate corrosion including solution chemistry (sections 2.3.2-2.3.4) and extended time periods (135) should be considered when predicting *in vivo* performance.

2.6 Synchrotron X-ray radiation techniques

2.6.1 Introduction

A synchrotron light source is used to generate light of high brilliance, usually in the form of X-rays. A schematic diagram of a synchrotron is shown in Figure 2-13. Electrons are generated by an electron gun and accelerated by a linear accelerator, the Linac into a booster ring. The booster ring further accelerates the electrons to their final energy following which they are introduced into a storage ring, which maintains their energy. The storage ring is equipped with an array of bending magnets, focusing magnets and insertion devices (third generation of synchrotron radiation facility), which forces the path of electrons to change and which results in the emission of X-rays which are then directed toward beamlines.

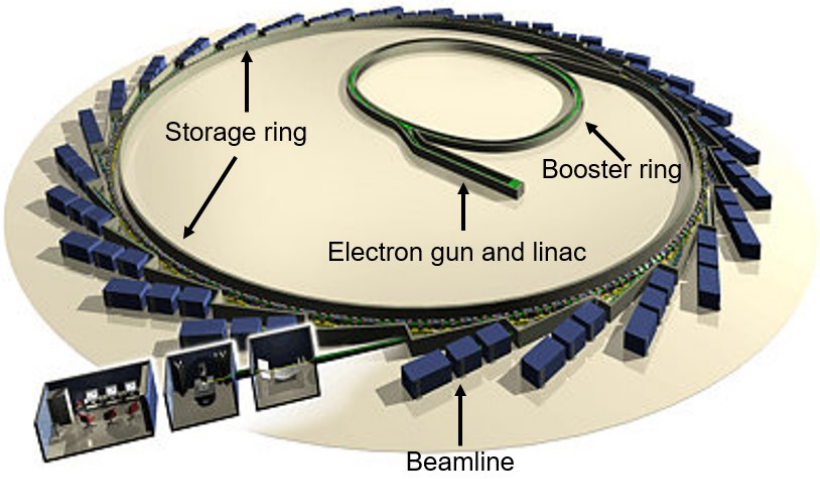

Figure 2-13. A schematic diagram of synchrotron radiation facility (136).

2.6.2 X-ray diffraction (XRD)

Synchrotron X-ray measurements have been widely used in corrosion systems to obtain structural and speciation information of the corrosion species formed in wet environments (137-140). Rayment et al. developed the experimental approach to enable in-situ X-ray diffraction measurements to be obtained on salt layers formed on the dissolving interfaces of Ni, Fe and stainless steel, which were controlled electrochemically on ‘artificial pit’ electrodes (137). ‘Artificial pits’ have been developed to provide a simple and reproducible geometry which allows modelling of localised corrosion processes such as the pitting of stainless steel (141). The approach provides access to regions of interest at or close to a corroding interface by a fine beam of synchrotron X-rays (137). X-ray diffraction measurements are then used to obtain structural information at identifiable and discrete regions within the artificial pit. Diffraction measurements allow characterisation of species including its chemistry and

structure to be made in-situ in wet environments, with the potential to measure transient events on timescales as short as 10 ms (137).

2.6.3 X-ray absorption spectroscopy (XAS)

X-ray absorption spectroscopy (XAS) includes the measurement of transitions of electrons of the metal from core states to excited states, known as X-ray absorption near edge structure (XANES), and to the continuum, which is known as extended X-ray absorption fine structure (EXAFS) (142). From Figure 2-14, XAS spectra is characterised by sudden increases in absorption at specific X-ray photon energies characteristic of the absorbing element. The sudden increases of absorption energy are known as absorption edges. The absorption edge, post-edge peaks as well as pre-edge characteristics featured in XANES spectra provide information of the oxidation state and coordination environment of the metal atoms (142). The significant advantage of XAS over XRD is that the local structural information of the element can be obtained even from disordered samples such as solution species (142).

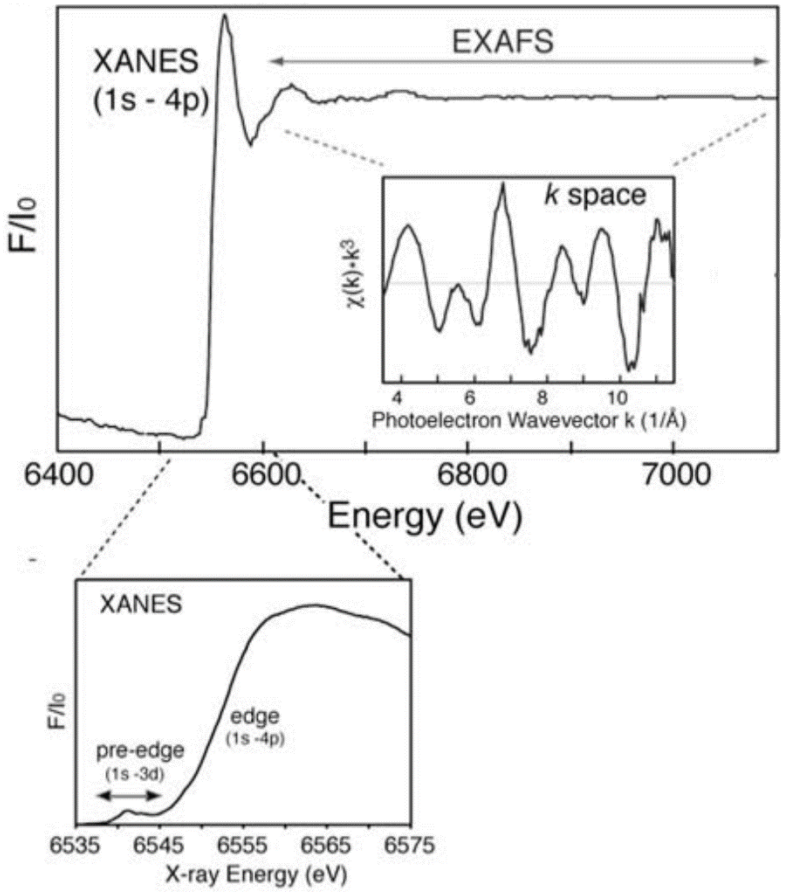

Figure 2-14. An example of Mn K edge XAS spectra illustrating XANES and EXAFS regions. Figure taken from (142).

2.7 Summary

Commercially pure (CP) Ti and Ti6Al4V are commonly used for dental implants. However, for specific applications such as small diameter dental implants, CP Ti is susceptible to mechanical failure. Ti6Al4V is currently the most commonly used alternative to CP Ti for dental implants and whilst it possesses enhanced mechanical properties including yield strength, there remains concern over the biological effects of its constituent alloying elements, Al and V. Binary TiZr alloys have been developed as an alternative to Ti6Al4V and possess improved mechanical properties with corrosion resistance and biocompatibility reported to be at least equivalent to that of CP Ti.

Although electrochemical studies have been carried out characterising the corrosion resistance of TiZr alloys with discrete compositions, there is a lack of previous investigation into the impact of systematic additions of Zr on the corrosion of Ti. The corrosion of TiZr alloys has been studied in a limited number of electrolytes such as artificial saliva, but their behaviour in more aggressive chemical species such as HCl and H_2O_2 is yet to be fully characterised. The role of cellular mediated corrosion by inflammatory cells such as macrophages has been studied on Ti surfaces, but to date no such similar characterisation has been performed for TiZr. Previous studies into the corrosion environments induced by macrophages, have failed to control for variations in their phenotype which is seen in the peri-implant tissues and determines their ROS production behaviour. Accordingly, **aim 1** of this thesis is to investigate systematically, the effect of Zr additions on the corrosion of Ti. Given the variation in the corrosion of Ti reported in different electrolytes, a

secondary aim is to characterise the corrosion behaviour of TiZr binary alloys in HCl solutions (to allow comparison with previously reported data), in physiological saline with absence and presence of H_2O_2, and in cellular corrosion conditions with differentiated M1 or M2 phenotypes of macrophages.

A recent study has shown that albumin, the most prevalent protein in blood and extracellular tissue fluid, accelerates the corrosion of Ti6Al4V in the presence of H_2O_2. The behaviour was not predicted by corrosion measurements following exposures of Ti6Al4V to albumin or H_2O_2 in isolation, but did not take into account potential temporal variations that may occur. Therefore, **aim 2** of the thesis is to understand the mechanism of the apparent synergistic effect of H_2O_2 and albumin on the corrosion of Ti6Al4V, and how their interactions with the Ti surface might be influenced by time. This work aims to better estimate the corrosion resistance of Ti6Al4V in an improved approximation of the peri-implant environment under inflammatory conditions.

In this thesis, the impact of Zr additions on the corrosion resistance of Ti explored, however there is an insufficient understanding of the localised corrosion of unalloyed Zr that may be expected *in vivo*. Accordingly, **aim 3** of the thesis is to characterise the corrosion behaviour of Zr, and the corrosion products formed, in a simulated physiological environment. The aim is to characterise both the solution chemistry and corrosion products in Zr artificial pits which are used as study model of pitting corrosion, in physiological saline with and without addition of H_2O_2 and/or albumin.

3 MATERIALS AND METHODS

3.1 Materials

Binary TiZr alloy rods (diameter 10 mm) containing 5, 15, and 50% Zr (at%) were commercially sourced (American Elements®, USA). These are referred to as Ti5Zr, Ti15Zr, Ti50Zr, respectively. All Grades were cast and melted at least three times to ensure homogeneity. CP Ti (ASTM, Grade 2, Titanium Products Ltd, UK)) discs (diameter 10 mm and thickness 1 mm) and CP Zr (Grade 702, GoodFellow, UK) rod (diameter 10 mm) were obtained. The compositions of the five alloys are listed in Table 3-1.

Ti6Al4V (ASTM Grade 5) was commercially sourced in disc shape specimens of 14 mm diameter and 1.2 mm thickness (Titanium Products Ltd, UK). The composition (max. wt%) was 0.05 N, 0.08 C, 0.015 H, 0.3 Fe, 0.2 O, 3.5-4.5 V, 5.5-6.8 Al, with the balance Ti.

Zr foil (25 µm thickness) was commercially sourced (Advent Research Materials, UK) in temper annealed condition with 99.8%wt Zr.

Table 3-1 The composition (wt%) of TiZr binary alloys (Certificate of Analysis, American Elements®), CP Ti (Grade 2) and CP Zr (Grade 702) (manufactures compositional certificates), (-, is not detected).

Alloys	Fe	Ni	Mg	Al	Si	Cu	Hf	Cr	C	O	N	H	Zr	Ti
CP Ti	0.03	-	-	-	-	-	-	-	0.01	0.13	<0.01	0.002	-	Bal.
Ti5Zr	0.075	0.002	0.002	0.018	0.005	0.016	-	-	< 0.01	< 0.08	-	-	9	Bal.
Ti15Zr	0.069	0.002	0.002	0.016	0.005	0.015	-	-	< 0.01	< 0.08	-	-	25	Bal.
Ti50Zr	0.048	0.002	0.003	0.012	0.007	0.009	-	-	< 0.01	< 0.08	-	-	66	Bal.
CP Zr	0.07	-	-	-	-	-	2.36	0.01	0.015	0.11	0.007	0.002	Bal.	-

3.2 Sample and surface preparation

All alloys were machined into 1 mm thickness for subsequent characterisations and testing. Specific sample and surface preparations, for different characterisation methods or measurements, are described in the following subsections.

3.2.1 Samples for metallographic characterisation

Samples for optical and electron microscopy characterisation were hot-mounted in conductive Bakelite resin (Struers, UK), then wet polished using sequentially 400, 800, 1200, 2500, and 4000 grit SiC abrasive grinding papers (MetPrep, UK). Final finishing was undertaken using OP-S colloidal silica suspension (0.04 μm) (Struers, UK) on an MD-Chem cloth (Struers, UK) to obtain a consistent mirror surface finish. All samples were rinsed and sonicated with deionised water (>15 MΩcm, Millipore, USA) and methanol, respectively for 10 min at each stage. Finally samples were dried in an air stream before further characterisation.

Prior to optical and microscopy characterisation, the as-polished CP Ti, Ti5Zr and Ti15Zr samples were etched in Kroll's agent (2% HF, 6% HNO_3 and 92% H_2O). Ti-50Zr was etched separately in diluted Kroll's agent (0.5% HF, 5% HNO_3, balanced with H_2O). CP Zr and Ti6Al4V samples were characterised in an as-polished surface condition.

3.2.2 Samples for electrochemical measurements

Samples for electrochemical tests were cold-mounted in a non-conductive resin (VARI-SET, MetPrep, UK), where an electrical cable was connected to the non-exposed sample surface with silver paint and conductive copper tape prior to the embedding in epoxy resin to maintain the electrical contact. The mounted samples were polished to mirror surface finishes using the methods described in section 3.2.1. The surfaces of prepared samples were rinsed with deionised water and 100% methanol and dried in an air stream. To ensure consistency in the surface oxide layer formed on different samples, each sample was exposed in ambient laboratory air for a fixed time of 15 min following final surface polishing, prior to the electrochemical characterisation.

3.2.3 Samples for cell culture immersion tests

Samples for immersion measurements in cell culture were prepared by wet polishing from 400, 800, 1200 to 2500 grit and finished with 4000 grit using endotoxin free water (sterile filtered, <0.005 EU/mL, Sigma Aldrich, UK) as the lubricant. Polished discs were then sonicated with methanol and endotoxin free water for 10 min sequentially in sterilised glassware.

3.2.4 Samples of Zr artificial pits for *in situ* synchrotron characterisation

Zr foil artificial pits and electrochemical cells were prepared according to the method described by Rayment et al. (137). The working electrode was made of 25 µm thick, 3 mm wide strips of Zr foil, which were embedded in Araldite epoxy resin and attached to a PVC plastic reservoir by Kapton adhesive tape. The

reservoir contained a Ag/AgCl reference electrode, a Pt wire auxiliary counter electrode and 20 mL electrolytes. A schematic diagram is shown in Figure 3-1.

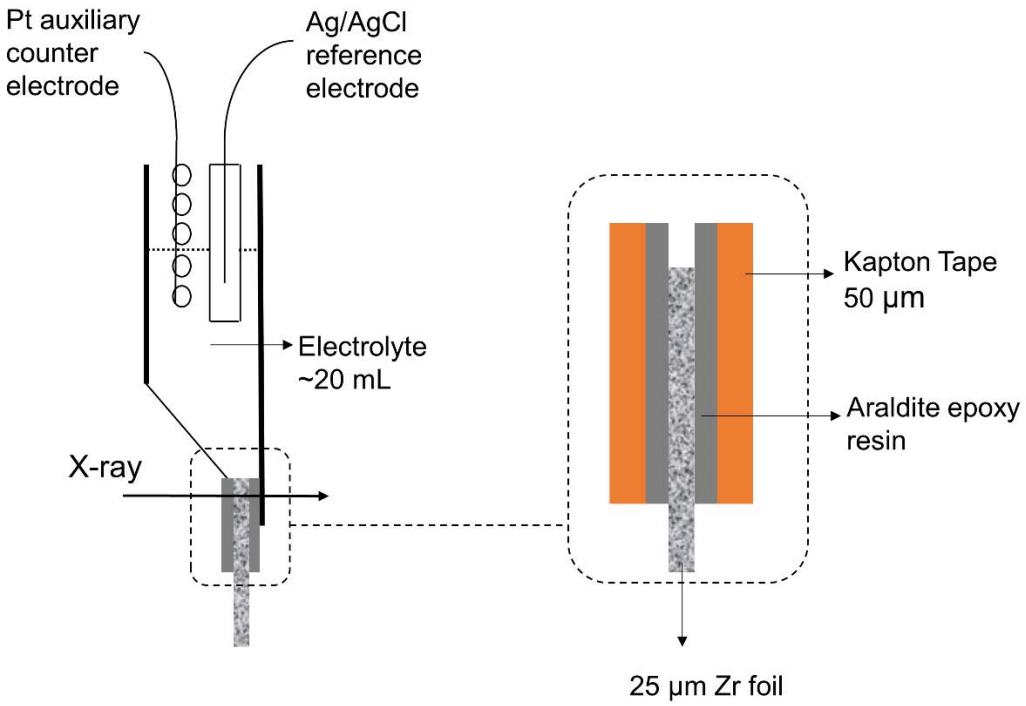

Figure 3-1. Schematic diagram of a Zr artificial pit and electrochemical cell for in-situ characterisation of corrosion using synchrotron X-ray methods.

3.3 Electrochemical measurements and testing solutions

3.3.1 General procedure

A standard, double wall three-electrode cell was used for both direct current (DC) and alternating current (AC) electrochemical tests. Cold mounted and surface prepared (section 3.2.2) electrochemical samples were used as the working electrode. Pt mesh was used as the counter electrode and a Saturated Calomel Electrode (SCE) was used as the reference electrode. The cell was maintained at a temperature of 37 $\pm$ 1 °C by a circulating heated water jacket supplied from a calibrated water bath (Bennett Scientific Ltd, UK).

A Gill AC potentiostat (ACM instruments, UK) was used for DC electrochemical tests (potentiodynamic and potentiostatic polarisations) and a Gamry PCI4 potentiostat (Gamry instruments, USA) was used for AC electrochemical tests (Electrochemical Impedance Spectroscopy). All electrochemical tests were repeated at least two times using newly prepared samples and solutions, to confirm the consistency of the measurements.

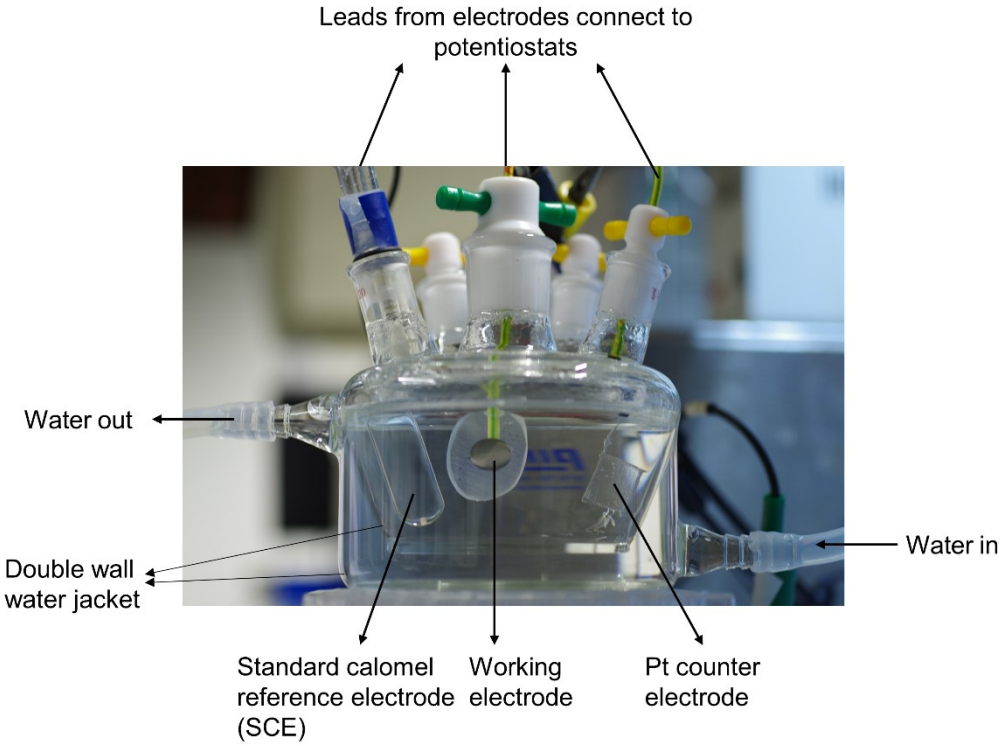

Figure 3-2. Illustration of the standard double wall three-electrode cell used in this study.

3.3.2 Potentiodynamic Polarisation

3.3.2.1 Ti, Zr and TiZr binary alloys

Naturally aerated 2 M HCl solutions were prepared from reagent grade HCl (30 wt% in H_2O, Fisher Scientific, UK) and diluted with deionised water. Physiological saline (0.15 M NaCl, 0.9 wt%) was prepared by dissolving NaCl (Sigma Aldrich, UK) in deionised water. H_2O_2 (30 wt % in H_2O, Sigma Aldrich, UK) was added to 0.9% NaCl solutions to give a concentration of 0.1 M. The reagent 30 wt% H_2O_2 solutions) were stored at 4 $\pm$ 2 °C to keep fresh.

The Open Circuit Potential (OCP) of samples including CP Ti, Ti5Zr, Ti15Zr, Ti50Zr and CP Zr were measured following immersion in the previously described test solutions for 1 h. Anodic polarisations were then performed from -50 mV (vs. OCP) at a scan rate of 1 mV/s. Cathodic polarisations were also performed, separately, after 1 h immersion at OCP in the testing solutions from 50 mV (vs. OCP) at a scan rate of 1 mV/s.

3.3.2.2 Ti6Al4V alloy

Physiological saline (0.9% NaCl, 0.15 M) solutions were again prepared by dissolving NaCl in deionised water. H_2O_2 (30 wt.% in H_2O, Sigma Aldrich, UK) was added to 0.9% NaCl to give a concentration of 0.1% (0.03 M). Bovine serum albumin (≥98%, lyophilized powder, Sigma Aldrich, UK) was dissolved in 0.9% NaCl containing 0.1% H_2O_2 to provide a concentration of 4% albumin.

OCPs of Ti6Al4V samples were measured by immersing samples in the previously described testing solutions for 1 h, followed by anodic polarisations from -50 mV (vs. OCP) at a scan rate of 1 mV/s.

3.3.3 Potentiostatic Polarisation

3.3.3.1 Ti, Zr and TiZr binary alloys

The effect of H_2O_2 on dissolution rate was studied by performing potentiostatic polarisation at 500 mV (vs. SCE) following 1h immersion at OCP in 0.9% NaCl. At 1000 s, a solution of 0.9% NaCl containing H_2O_2 was added to generate a final concentration of 0.1 M H_2O_2, which was stirred to ensure complete mixing. Further experiments were performed in parallel where the solution was stirred at the same time points without any addition of H_2O_2, to control for any effect of electrolyte agitation on the recorded measurements.

3.3.3.2 Ti6Al4V alloy

To study the effect of H_2O_2 and the combination of albumin and H_2O_2 species on dissolution rate, potentiostatic polarisation was performed at 400 mV (vs. SCE) after 1 h immersion at OCP in 0.9% NaCl, followed by sequential additions of 0.1% H_2O_2 with and without 4% albumin. Solutions were stirred during the addition of species to ensure complete mixing. A solution of 0.9% NaCl containing H_2O_2 was added at ~0.6 h to give a final concentration of 0.1% H_2O_2 and a solution of 0.9% NaCl containing albumin was added at ~0.74 h to give a final concentration of 4% albumin. The control solution without any addition of species was stirred at the same times to ensure consistency in the experimental approach.

To measure metal release at constant potentials, Ti6Al4V samples were potentiostatically polarised at 90 or 200 mV (vs. SCE) for 24 h after 1 h

immersion at OCP in 0.9% NaCl with presence of 0.1% H_2O_2 or a combination of 0.1% H_2O_2 and 4% albumin.

3.3.4 Electrochemical Impedance spectroscopy (EIS)

EIS measurements were performed on Ti6Al4V samples at OCP in the same solutions as described in section 3.3.2.2, perturbing with a 10 mV RMC AC signal with a wide frequency range from 10^{-3} to 10^5 Hz. The acquisition rate was 10 points per decade. Measurements were taken following immersion in the solution at 24 h intervals up to 120 h. Additional samples were held at constant potentials of 40, 90, 110, 150, or 200 mV (vs. SCE) for 20 h after which EIS was measured at the constant potential. A two-time constant electrical circuit (Figure 3-3) was used to fit the EIS data, which consisted of two parallel Constant Phase Element (CPE) and resistor pairs in series with solution resistance (R_s). (77, 143). Fitting of the EIS data was performed using Gamry Echem Analyst software employing the simplex algorithm method, and the quality of fitting was judged by a chi-squared test (χ^2) < 0.001. Quantitative parameters were obtained. Polarisation resistance was calculated from the sum R_{hf} and R_{lf}, corresponding to the resistances of the inner compact and outer porous passive layer respectively.

The capacitance (C) was converted from the CPE component (Y_0, Figure 3-3) using the Mansfield equation (144):

$$C = Y_0(\omega''_m)^{a-1} \qquad \text{Equation 3-1}$$

where ω''_m is the angular frequency at which the imaginary part of impedance has a maximum (144), 'Y_0' is the CPE parameter and its physical significance is

not often discussed (144), and 'a' has no real physical bases and its value varies between 0 to 1. For an ideal capacitor a=1 and $C=Y_0$.

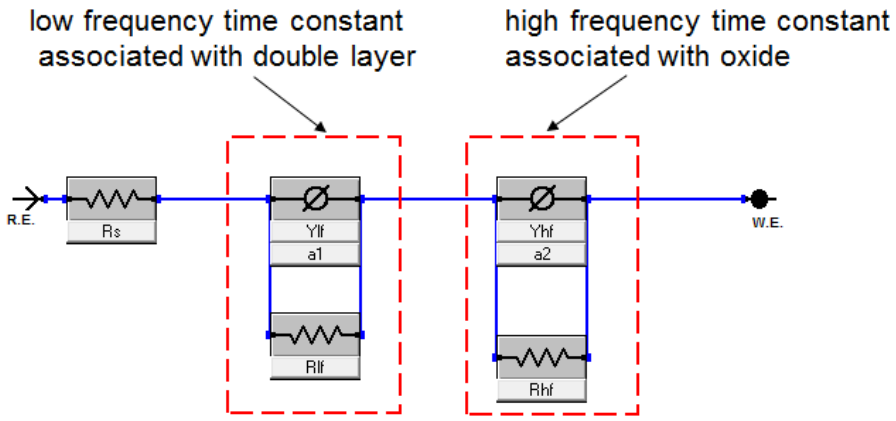

Figure 3-3. Equivalent two-time constants circuit in generation of simulation data.

R.E. refers to reference electrode; W.E. refers to working electrode; R_s refers to solution resistance; Y_{lf} and Y_{hf} refer to CPE component at low frequency (lf) and high frequency (hf) respectively; R_{lf} and R_{hf} refer to resistive component at low frequency (lf) and high frequency (hf) respectively.

3.3.5 Electrochemical measurements of Zr artificial pits and bulk Zr samples

The electrochemical cell used for Zr artificial corrosion pit measurements is shown in Figure 3-1. 20 mL of electrolyte was used which contained 0.9% NaCl with or without addition of 0.1 wt.% H_2O_2 (30 wt.% in H_2O, Sigma Aldrich, UK), or 4 wt.% albumin (≥98%, lyophilized powder, Sigma Aldrich, UK), or their combination. Prior to in-situ synchrotron characterisation, the working electrode (Zr foil) was electrochemically dissolved at 0.8 V (Ag/AgCl) for 3 h at an ambient

temperature of 23 ± 1 °C. The potential was controlled by a potentiostat (Ivium Compactstat, Netherlands).

Complementary electrochemical measurements on bulk Zr samples were carried out in the same electrolytes as those used in the artificial pit experiments. Samples with surface prepared according to section 3.2.2, were immediately immersed in the solutions followed by OCP measurements for 1 h at 37 °C. Anodic polarisations were performed after 1 h at OCP scanning from -50 mV (vs. OCP) at a rate of 1 mV/s. The current limit was set at 1 mA/cm^2 following which the measurement was stopped. Samples after anodic breakdown were stored in a desiccator prior to SEM characterisation.

3.4 Immersion tests

3.4.1 Corrosion (ion release) in macrophage cell culture

Surface prepared metal discs including CP Ti, Ti5Zr, Ti15Zr, Ti50Zr and CP Zr (section 3.2.3) were sterilised by incubating in 70% ethanol for 1 h followed by rinsing in endotoxin free RPMI-1640 medium (R8758, Sigma Aldrich, UK). Sterilised discs were placed into 24 well plastic plates which had been pre-blocked with RPMI-1640 medium supplemented with 10% fetal bovine serum (FBS) overnight. A culture medium of RPMI-1640 with addition of 10% fetal bovine serum (FBS), amphotericin B (2.5 µg/mL), penicillin (100 units/mL), streptomycin (100 µg/mL) and phorbol 12 myristate 13 acetate (PMA) (10 ng/mL) was prepared. THP-1 cells, a human monocytic cell line, were differentiated into macrophage-like cells using PMA. To differentiate THP-1 cells

into M1 and M2 phenotypes (representative of their more or less active state respectively), the bulk medium was supplemented by lipopolysaccharide (LPS) (100 ng/mL) and interferon gamma (IFN-γ) (50 ng/mL) to differentiate a M1 phenotype, or interleukin 4 (IL-4) (10 ng/mL) to differentiate a M2 phenotype (145). THP-1 cells were grown to passage 15 and the initial cell density was counted using a light microscope (LeitzLaborlux S, Germany) and a haemocytometer (Neabauer, Reichart, Germany). The viability of THP-1 cells was determined using Trypan Blue exclusion (Sigma Aldrich, UK) and was typically >95%. A starting concentration of $6.7x10^5$ cell/mL was used. 1.5 mL of the cell suspension was incubated in wells with each metal disc. Cell culture medium was also incubated with the metal samples as a control condition. Control groups with no metal discs were also prepared in parallel, containing 1.5 mL of M1 cells with the bulk medium, 1.5 mL of M2 cells with the bulk medium and the bulk medium alone, respectively. Six groups of incubation assays, with triplicated samples for each group, were incubated in a thermostatic incubator at 37 °C, 5% CO_2 and 100% humidity. After 4 days of incubation, 1 mL of medium was removed from each well and replaced with 1 mL of fresh medium with appropriate cytokines. The extracted media from the wells were individually stored and frozen at -20 °C. This process was repeated 3 times for each consecutive 4 day period. At the end of 13 days incubation, 60 µL of the cell lysing agent, 10% sodium dodecyl (lauryl) sulphate (SDS) was added into all wells (including the control groups) and 1.5 mL medium which included supernatants and cell lysates were collected from each well and frozen at -20 °C.

For inductively coupled plasma-mass spectroscopy (ICP-MS) analysis, the 3 media aliquots (3 mL) collected during the incubation and the 1.5 mL aliquot collected at the end of incubation were pooled together, from which 3.4 mL was taken for solution analysis. The remaining media (~1.1 mL) was reserved as a contingency for potential verification assays.

3.4.2 Incubation of Ti6Al4Vin H_2O_2 and/or albumin containing solutions to investigate morphology of surface oxide layer

Ti6Al4V discs were mirror polished on both sides using the methods described in section 3.2.1 and ultrasonically cleaned with deionised water and methanol for 10 min respectively. The prepared discs were incubated in saline with 10% H_2O_2 solution for 3 days in thermostatic chamber at 37 $\pm$ 1 °C. The H_2O_2 treated samples were then transferred to 0.1% H_2O_2 saline solutions with and without addition of 4% albumin for 7 days. Following the immersion period, surfaces were visualised using methods described in section 3.6.2

3.4.3 Quantification of metal release

3.4.3.1 Determination of metal release of Ti, Zr and TiZr samples in cell culture

The retrieved pooled sample solutions (section 3.4.1) were kept frozen at -20 °C prior to analysis. The elemental concentrations of Ti and Zr in the retrieved samples were quantified from the undiluted sample solutions using a Thermo iCAP™ 7000 ICP-AES (inductively coupled plasma-atomic emission spectroscopy) system (Thermo Fisher Scientific, UK), which was calibrated against serially diluted Ti and Zr standards (Fisher Scientific, UK). ICP-AES

determines the elemental concentration by using inductively coupled plasma to excite atoms and ions which emit electromagnetic radiation at wavelength characteristic of a particular element. The system was rinsed with 10% HNO_3 in between each sample analysis. The detection limit was 0.3 ppb for Ti and 0.4 ppb for Zr.

3.4.3.2 Determination of metal release from Ti6Al4V polarised at constant potentials

Solutions were retrieved following potentiostatic measurements (section 3.3.3.2) and elements of interest (i.e. Ti, Al, V) were detected using inductive coupled plasma mass spectroscopy (Agilent 8800 ICPMS triple quad, Butterworth Laboratories, UK). The working quantitation limit for Ti was 10 µg/L, Al was 100 µg/L and V was 10 µg/L. 5 mL sample aliquots were measured and diluted up to 1000 mL with water and diluent containing 1.5 mL of Triton-x-100, 0.15 mL of 20% ammonia and 15 mL of 1.4 mM EDTA. The elemental concentration for each solution were compared across the potentials through one-way analysis of variance (ANOVA) at a significance level of $\alpha=0.05$.

3.5 *in situ* characterisation of Zr artificial corrosion pit using synchrotron X-ray methods

3.5.1 X-ray diffraction

Established ‘growing’ Zr artificial pits (section 3.3.5) were characterised in-situ using X-ray diffraction measurements, which were conducted at the micro-focus spectroscopy beamline, I18 at the Diamond Light Source (Harwell, Oxford, UK) (146) An incidence energy of 17,950 eV (corresponding to a wavelength of

0.691 Å) and beam spot size of 3 µm (v) x 10 µm (h) were used. Measurements were taken with a CCD detector (2x1 sCMOS camera, Photonic Science, UK) providing a pixel size resolution of 26 µm x 26 µm. The electrochemical cell was mounted on a precision positioning stage which allows diffraction measurements to be taken at any location with respect to the corroding metal solution interface. Prior to measurements, the metal solution interface was focused and the sample was positioned where the incident X-ray beam was positioned in the electrolyte above any formed corrosion products. Diffraction patterns were collected from the electrolyte towards the metal solution interface by moving the sample stage at 100 µm increments. A schematic diagram (Figure 3-4a) illustrates the approach which enabled the measurements of all different regions of the corroding interface to be made. Corrosion products close to the dissolving metal interface were also measured with a reduced step size of 10 µm (Figure 3-4b) enabling changes at a higher spatial resolution to be identified. Both sets of diffraction measurements were repeated in each electrolyte solution. The exposure time was limited to 30 s to reduce beam damage. The position of each diffraction pattern is correlated with a ‘live’ optical image of the corroding artificial pit to allow exact correlation of the diffraction pattern relative to the moving (due to continued corrosion) metal-electrolyte interface. X-ray diffraction patterns were integrated and analysed in DAWN (Version 2.0.0, 2010-2016) (147) and fullprof software (Version 3.00, 2015) (148).

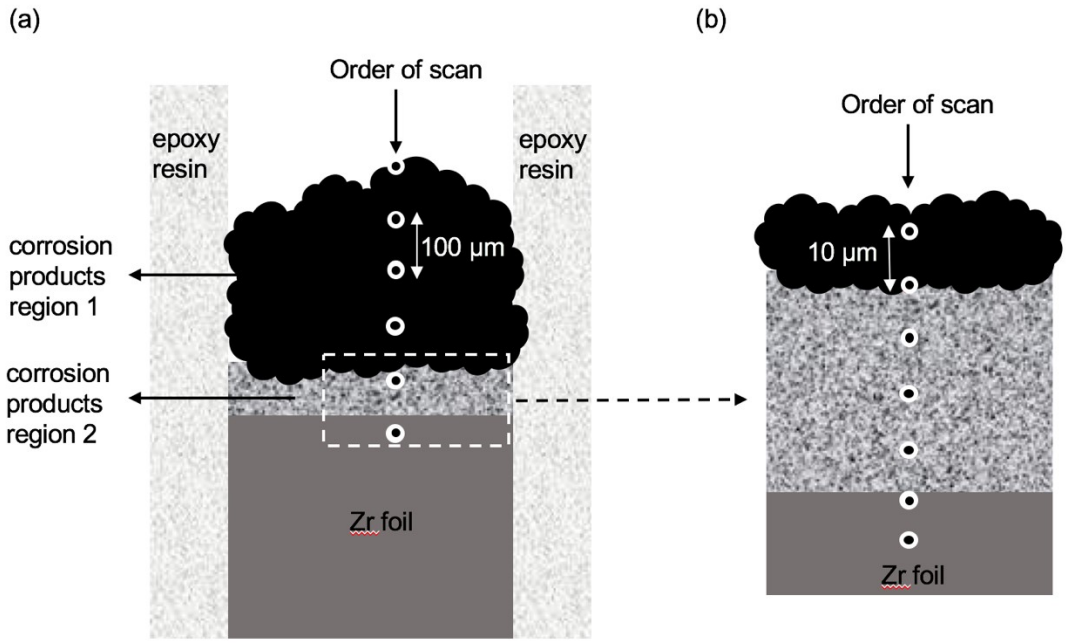

Figure 3-4. Schematic diagram of the XRD scan path through different regions of corrosion products inside Zr artificial pit. (a) order of a coarse XRD scan at 100 µm spacing from electrolyte through corrosion products into Zr foil; (b) order of a fine XRD scan at 10 µm spacing through corrosion products region 2 close to dissolving metal interface.

3.5.2 X-ray absorption near edge structure (XANES)

XANES was used to study solution Zr species. XANES measurements were taken for Zr standard compounds and at various regimes at the artificial pit in a fluorescence geometry using the same beamline, I18, immediately following XRD measurements. A Zr reference foil was used for energy calibration for the XANES measurements. Zr reference compounds included ZrO_2 (98.5%, Fisher Scientific, UK), $ZrOCl_2 \cdot 8H_2O$ (reagent grade 98%, Scientific Laboratory Supplies, UK) and $Zr(OH)_4$ (97%, Sigma-Aldrich, UK), were prepared from the as-received powder form.

XANES spectra were obtained using a Si (111) double crystal monochromator which produced a focused X-ray beam with energy ranging from 17,900 eV to 18,400 eV. The beam spot size was maintained at 3 µm (v) x 10 µm (h). Fluorescence data were collected using a 4-element Vortex Si drift detector. To maximize the signal to noise ratio, 206 energy points were used across the absorption edge with an irradiation time of 1s per point. The resulting spectra were background corrected and normalised using Athena software (Version 0.9.24) (149).

3.6 Surface characterisation

3.6.1 Surface coverage of cells on Ti, Zr and TiZr substrates

Cell adherence and the cell morphologies of THP-1 cells on each metal substrate including CP Ti, Ti5Zr, Ti15Zr, Ti50Zr and CP Zr were characterised using a Zeiss EVO MA-10 (Carl Zeiss, Germany) scanning electron microscope (SEM) in secondary electron mode with an energy of 10 keV. Surface coverage of cells (which was considered to reflect the percentage of the surface exposed to cell-generated ROS conditions) was examined by SEM imaging of the retrieved metal substrates after culturing with unstimulated THP-1 cells for 7 days for each alloy composition. The morphologies of M1 and M2 phenotypes of THP-1 cells were characterised on retrieved CP Ti substrates after culturing with the cells in their respective media for 24 h. All the retrieved discs were prepared by fixation and dehydration prior to SEM characterisation. The retrieved metal substrates with adhered cells were washed with Hank's balanced salt solution gently 3 times and fixed by incubation in 1.5 mL of 2.5%

glutaraldehyde (EM Grade, Agar Scientific, UK) in 0.1 M sodium cacodylate for 10 min at room temperature. The disks were then dehydrated by sequential immersion in 1 mL of 20, 30, 40, 50, 60, 70, 90, 95, 100% (twice) ethanol for 10 min, followed by incubating with 0.2 mL of hexamethyldisilazane which was allowed to evaporate overnight.

Image analysis on standardised SEM images (cell morphology and surface coverage) was performed using Fiji software (ImageJ, National Institutes of Health, USA) using a previously validated method (150). Briefly, the cells were segmented from the surface using Trainable Weka Segmentation with segmentation filters previously described in (150). The training features include Gaussian blur, sobel filter, hessian, difference of Gaussians and membrane projections, mean, minimum, maximum and median. Other settings were unchanged from the default including membrane thickness 1, membrane patch size 19, minimum sigma 1.0, and maximum sigma 16.0.

The segmented images were converted into binary images so that the histogram of pixels corresponding to cells could be calculated. Objects that were less than 30 pixels in size were assumed to be noise and were removed using ‘Analyse Particles’ plugin (150). The cell spread area was then calculated by percentages of number of pixels. Differences between samples were detected using a one-way analysis of variance (ANOVA) at a significance level of $\alpha=0.05$.

3.6.2 Surface morphology of Ti6Al4V and Zr after corrosion

Ti6Al4V samples preceeding and following incubation (section 3.4.2) in H_2O_2 and/or albumin containing solutions were examined by SEM JEOL 6060 (Japan Electron Optics Laboratory Ltd., Japan) using an acceleration voltage of 20 kV in both secondary electron (SE) and back scattered electron (BSE) mode. Energy Dispersive X-ray spectroscopy (EDX) (Oxford instruments, UK) was used to analyse these compositions of surface corrosion products.

Top-down surface morphology of an in-situ grown Zr artificial pit (section 3.3.5) and bulk Zr samples following anodic breakdown (section 3.3.5) were examined by SEM in secondary electron mode using a JEOL 7000 (Japan Electron Optics Laboratory Ltd., Japan) with an operating energy of 20 keV. The corroded Zr artificial pit which was previously embedded in epoxy was immersed into methanol for 10 min to allow the epoxy resin to be removed. The exposed foil was cleaned with methanol and deionised water in an ultrasonic bath for 10 min respectively, followed by mounting on an Al sample stub with the corrosion interface facing upwards.

3.7 Transmission electron microscopy

Zr corrosion products from an established artificial pit were collected and characterised by Transmission Electron Microscopy using a FEI Talos^{TM} system with an operating energy of 200 keV in conjunction with an energy dispersive x-ray spectroscopy (EDS) detector for high resolution morphology characterisation and chemical analysis. Corrosion products were collected from

a Zr artificial pit which was grown at 0.8 V (Ag/AgCl) in 0.9% NaCl for ~3 h ambient temperature. The collected corrosion products were rinsed with deionised water into a 30 mL plastic tube, where settlements of corrosion products were obtained after 24 h. The supernatant was discarded and the pellet of corrosion products was dispersed onto a gold TEM sample grid using a microliter syringe. The TEM sample grid with deposited corrosion products was placed in a desiccator before characterisation.

4 THE EFFECT OF ZR ADDITION ON THE CORROSION OF TI IN SIMULATED PHYSIOLOGICAL CONDITIONS

4.1 Introduction

The aim of the work described in this chapter is to systematically investigate the effect of Zr additions to Ti on its corrosion resistance in simulated physiological solutions that may be encountered in the peri-implant environment. These measurements are complemented by preliminary work on cellular induced corrosion by studying metal ion release associated with inflammation. The rationale behind the work is to address the knowledge gap regarding the corrosion resistance of new TiZr binary alloys, which have been developed to provide improved mechanical properties for small diameter implants, in a better approximation of peri-implant environment.

In this work, the effect of systematic additions of Zr (ranging from 0, 5, 15, 50 through to 100 at%) on the corrosion of Ti was studied in solutions that could represent conditions encountered in the peri-implant environment. 2 M HCl was used to simulate localised acidification as a result of processes such as mechanically assisted crevice corrosion (MACC). H_2O_2 was used to simulate inflammatory environment where Reactive Oxygen Species (ROS), including H_2O_2, are produced by immune cells and certain bacteria which form implant surface biofilms. The inflammatory environment was approximated by the introduction of 0.1 M H_2O_2 in 0.9% NaCl (ASTM standards) in this study. To simulate complex corrosion conditions as a consequence at cellular modification of the immediate implant environment, THP-1 cells, a human

monocytic cell line, were induced into a pro-inflammatory M1 phenotype or into a tissue-repair M2 phenotype to mimic the different functional behaviour of macrophages during acute and chronic stages of inflammation. The corrosion behaviour of the five types of alloys (CP Ti, Ti5Zr, Ti15Zr, Ti50Zr and CP Zr) were characterised by electrochemical measurements including Open Circuit Potential (OCP), potentiodynamic polarisations (anodic and cathodic) as well as potentiostatic polarisations (anodic) in solutions including 2 M HCl, or 0.9% NaCl with and without the presence of H_2O_2. The corrosion of the five different alloy compositions were also characterised in the presence of stimulated THP-1 cells (M1 or M2 phenotypes), by measuring metal release over long-term incubation in this cellular environment. Factors influencing metal release such as cell adherence and surface coverage on the different substrates, as well as cell morphologies in M1 or M2 phenotypes were characterised using SEM combined with quantitative image analysis and therefore correlated with corrosion measurements.

4.2 Microstructure Characterisation

Optical micrographs of etched CP Ti and binary TiZr alloys discs are shown in Figure 4-1. CP Ti consists of equiaxed α grains. Ti5Zr has coarse as-cast grains within which there are primary α lamellae in colonies. With increases in Zr content, as shown in the case for Ti15Zr and Ti50Zr, finer needle-type structures are exhibited. The acicular structure identified in Ti-50Zr is characteristic of martensite, which is often formed by diffusionless transformation.

As-polished CP Zr and TiZr alloy discs were examined by SEM under BSE mode. Alloy partitioning can be observed on the Ti5Zr and Ti15Zr surfaces (Figure 4-2), where the brighter (whiter in the Figure 4-2) area of lath boundaries were associated with higher concentrations of Zr confirmed by EDX. The as-polished Ti50Zr surface showed a finer needle-type structure which is consistent with its etched structure. The CP Zr surface showed features of α grains with a uniform distribution of second phase particles with a size of 1-5 μm (Figure 4-2). A higher resolution BSE image of the second phase particles can be found in Figure 4-3a and a confined area was analysed by EDX (marked with a solid red box). The spectrum from the analysed area showed peaks of Zr, Fe and Hf. Elemental mapping of the three elements revealed that the particles are enriched in Fe and depleted in Zr. The consolidated map of all elements showed that the analysed area consisted of Fe-rich second phase particles distributed in a matrix of Zr with a minor concentration of Hf.

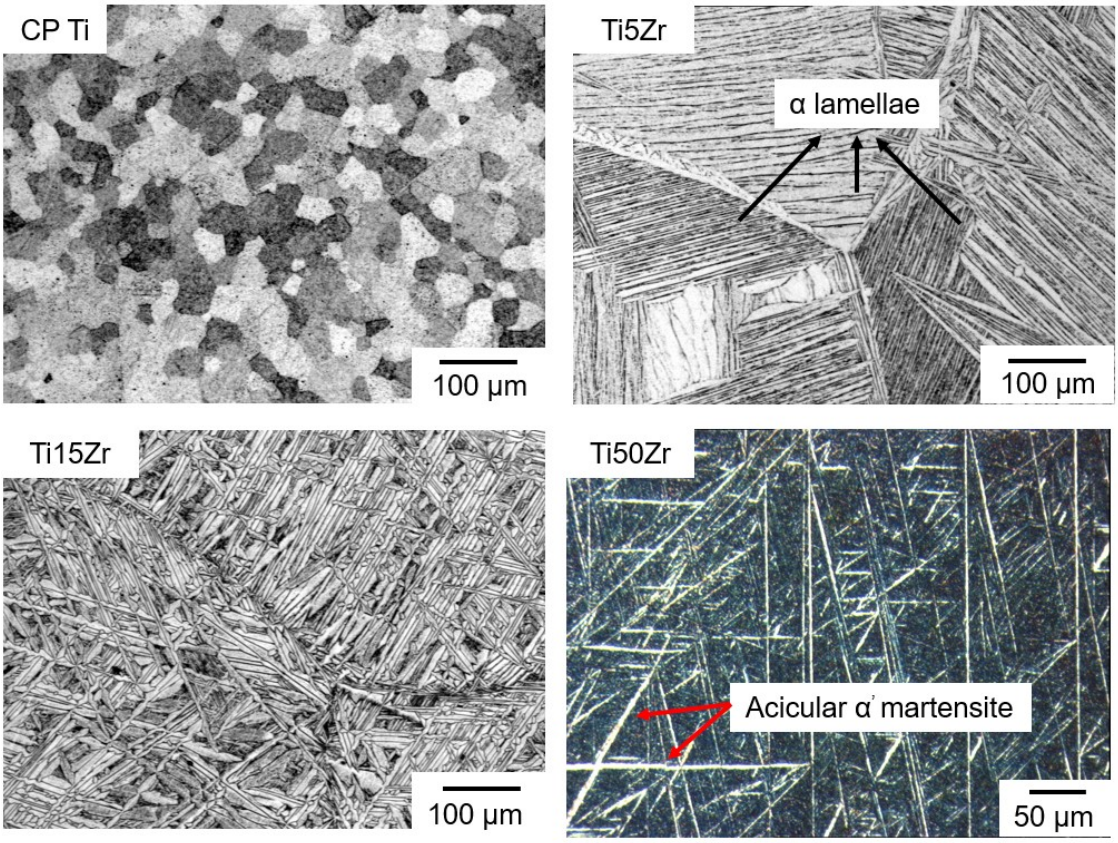

Figure 4-1. Optical microscopy images of the etched surfaces of CP Ti G2, Ti5Zr, Ti15Zr and Ti50Zr (Zr in at %). Microstructure of Ti50Zr was characterised under a polarised optical microscope.

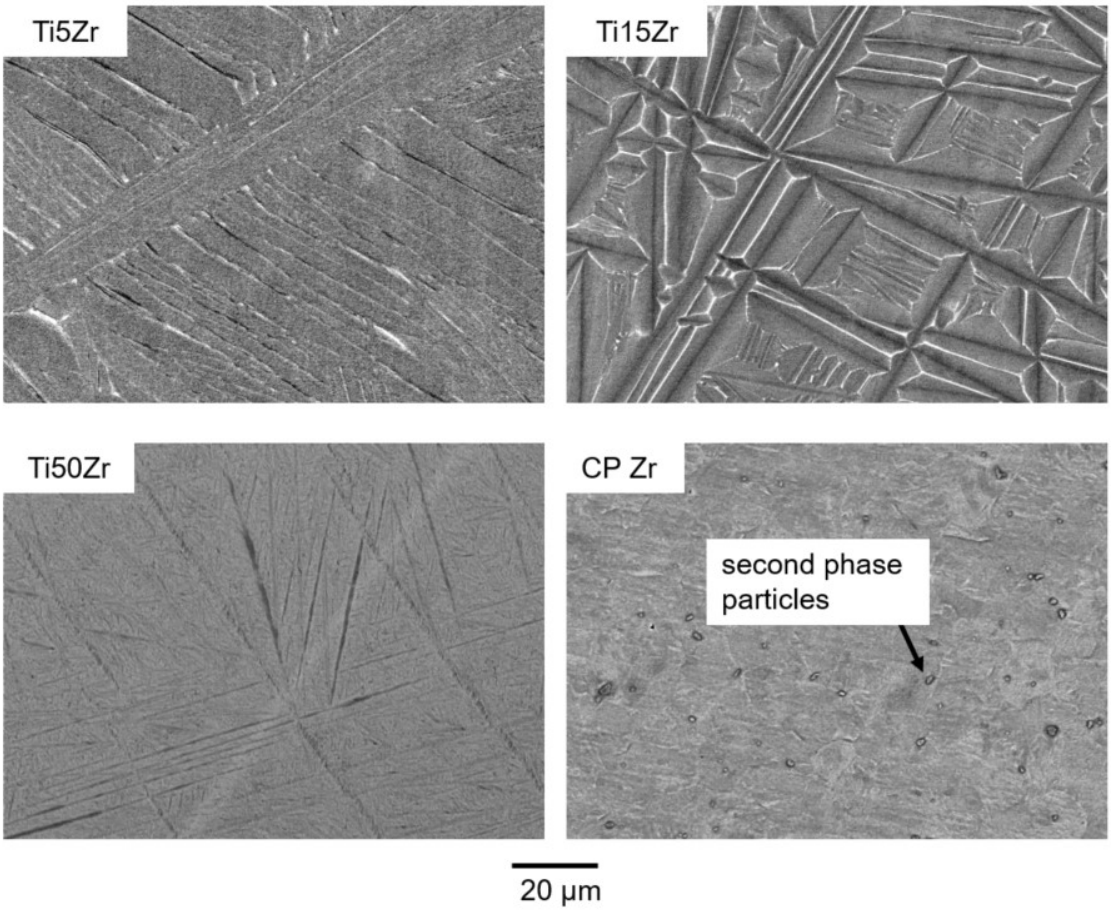

Figure 4-2. BSE images of as polished surfaces of the TiZr alloys (Ti5Zr, Ti15Zr, Ti50Zr) and CP Zr.

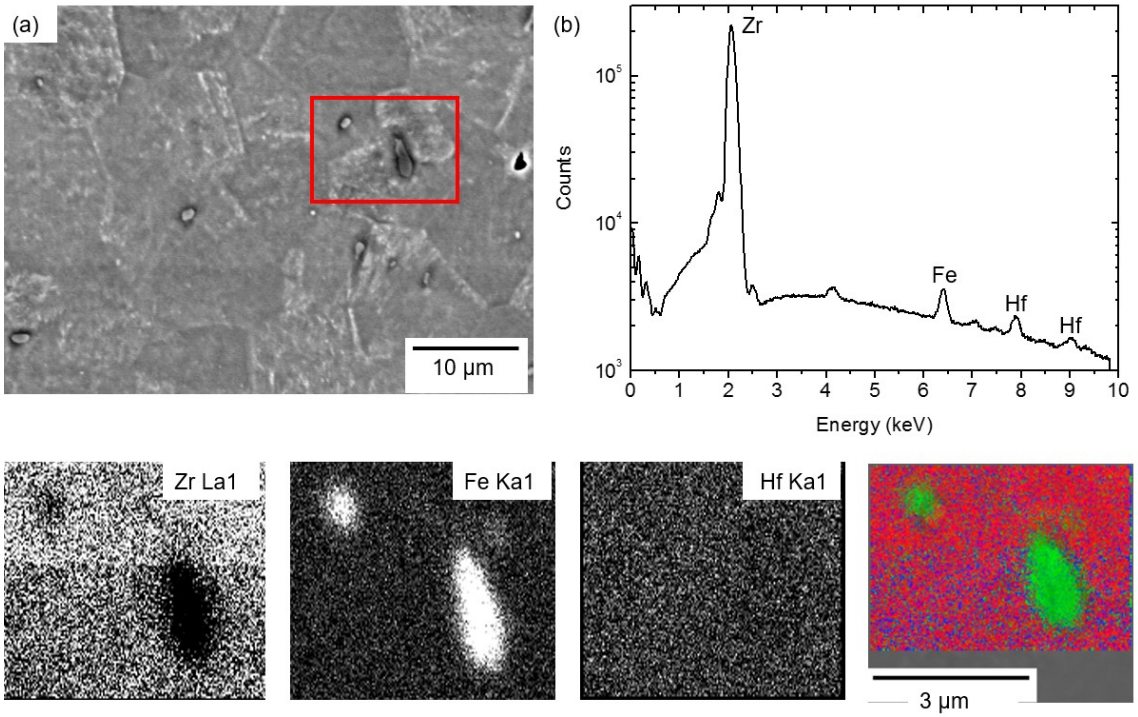

Figure 4-3. (a) Higher resolution BSE image of second phase particles on the CP Zr surface. A selected area containing particles is labelled (solid red box) and examined by EDX with spectrum shown in (b). Elemental maps of Zr (Lα 1), Fe (Kα 1) and Hf (Kα 1) and the consolidated mapping are shown at the bottom.

4.3 Corrosion behaviour in HCl

Open circuit potentials (OCPs) of CP Ti, TiZr binary alloys and CP Zr in 2 M HCl solutions are shown in Figure 4-4. The OCP for CP Ti showed rapid decease with time from ~ -350 mV, then settled close to -650 mV, consistent with a depassivation. Ti5Zr also showed an abrupt decrease in OCP, but the timescale was significantly longer than that for CP Ti and the OCP after 1 h was slightly higher at ~-600 mV. Ti15Zr showed a much more gradual decrease in OCP to ~-400 mV whereas Ti50Zr and CP Zr both showed a gradual increase in OCP to ~-300 mV and ~-230 mV, respectively indicating surface passivation.

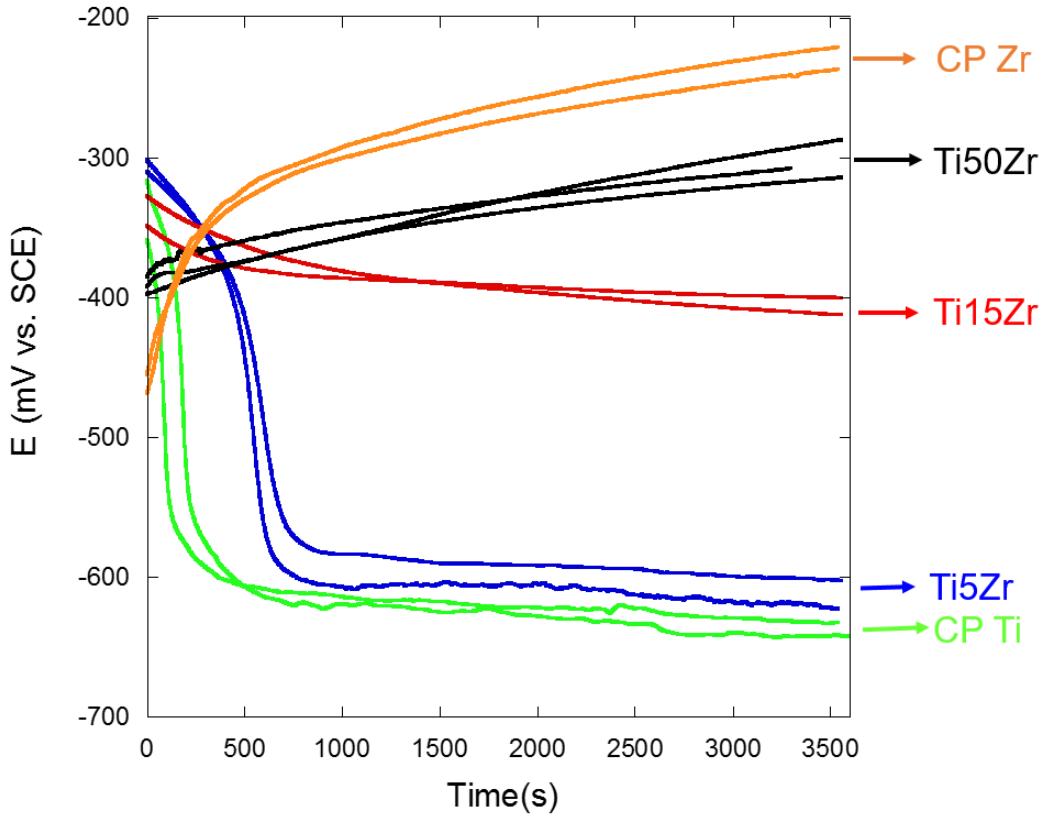

Figure 4-4. Open Circuit Potentials of CP Ti, Ti5Zr, Ti15Zr, Ti50Zr alloys and CP Zr with naturally air-formed oxides in 2 M HCl for 1 h at 37 °C

Anodic polarisation curves of the alloys after 1 h immersion in 2 M HCl solutions at OCP are shown in Figure 4-5. CP Ti exhibited a clear active/passive transition at -500 mV with an anodic peak of critical current density (i_{crit}) of ~60 µA/cm^2, whereas Ti5Zr showed a similar active passive transition but with a reduced i_{crit} of ~40 µA/cm^2. There is no sign of any increased current density at high potential associated with pitting corrosion. Ti15Zr did not show an active-passive transition but instead showed only a passive region with a passive current density of ~10 µA/cm^2 without any sign of pitting corrosion at potentials up to 1.4 V. Ti50Zr showed similar passive behaviour with a lower passive current density of ~5 µA/cm^2 compared with Ti15Zr, however it was susceptible to pitting corrosion, shown by a sudden increase in current at higher

potential. The pitting potential was variable with one value 640 mV and the other above 1000 mV. Similarly, CP Zr was even more susceptible to pitting at much lower potentials at approximately 100 mV.

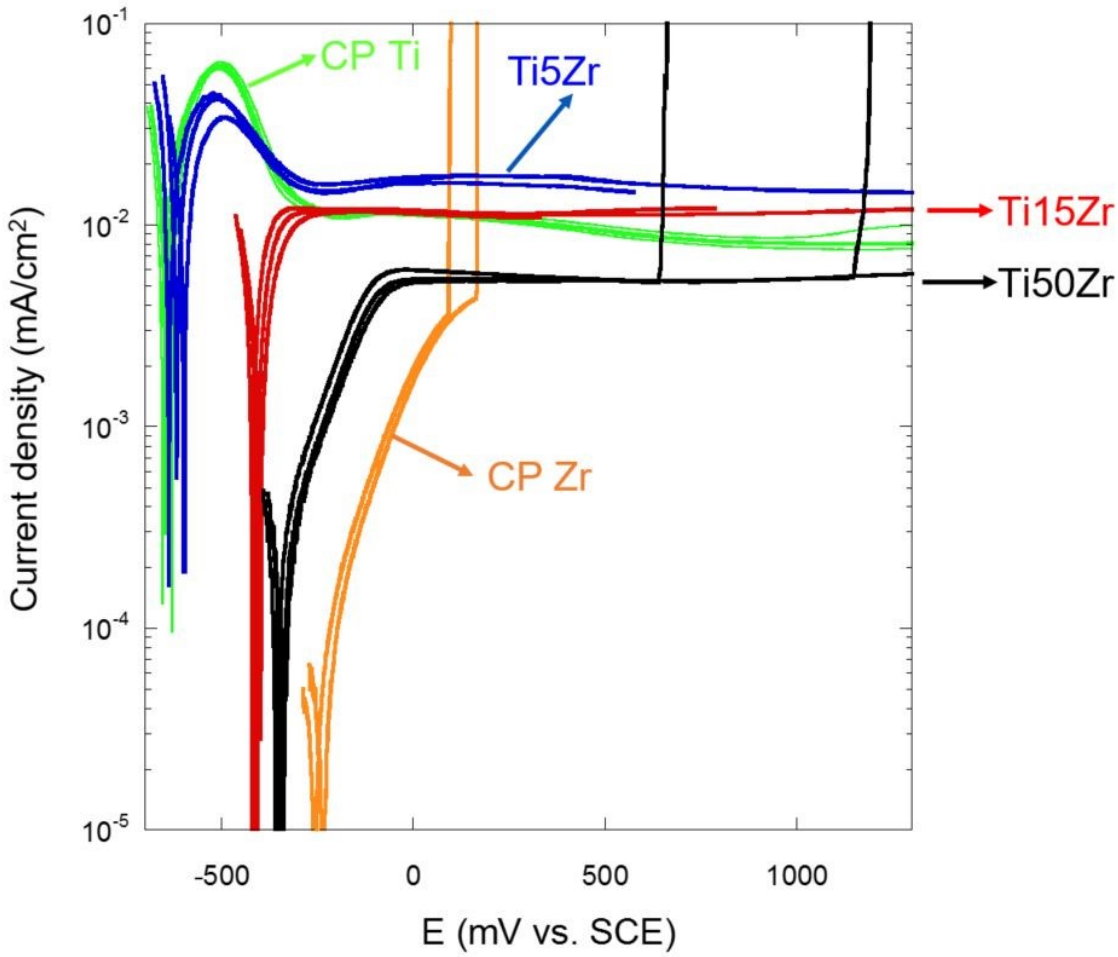

Figure 4-5. Anodic polarisation of CP Ti, Ti5Zr, Ti15Zr, Ti50Zr alloys and CP Zr in naturally aerated 2 M HCl at 37°C after 1 h immersion at OCP. Scan rate was 1 mV/s.

Pits on surfaces of Ti50Zr and CP Zr after anodic polarisation are examined by SEM and are shown in Figure 4-6. The Ti50Zr sample shows a pit that is irregular in shape with faceted boundaries. The pit appeared to have developed from the edge of the sample. At higher magnification, acicular structures can be seen inside of the pit that are similar to the etched structure (Figure 4-1). The

CP Zr sample showed circular pit patches where some were in the centre and others had grown into the edge. At higher magnification, a rough morphology was observed within the corroded area.

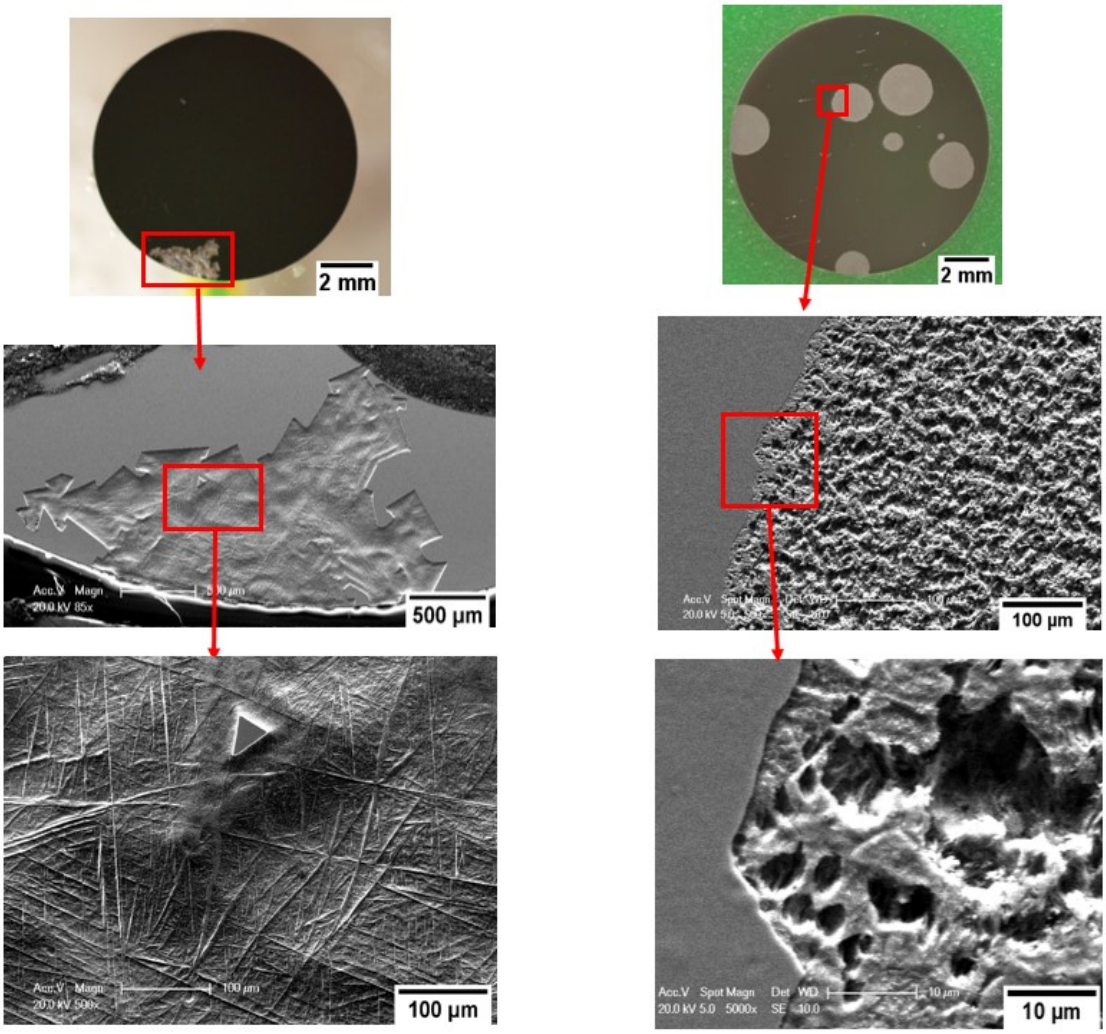

Figure 4-6. SEM images of pits on surfaces of Ti50Zr (left) and CP Zr (right) after anodic breakdown in 2 M HCl solutions at 37 °C.

4.4 Corrosion behaviour in physiological saline with and without H_2O_2

The OCP as a function of time were measured for CP Ti, TiZr alloys and CP Zr in 0.9% NaCl with and without addition of 0.1 M H_2O_2. For all of the measurements, the OCPs gradually increased during the 1 h immersion period,

indicating increased passivation. The OCPs of Ti15Zr are shown in Figure 4-8 as an example. It can be seen that in 0.9% NaCl, the OCP of Ti15Zr was gradually increased during the 1 h immersion period, and this was associated with passive film development and reduced anodic current density. Addition of H_2O_2 in 0.9% NaCl increased the OCP of Ti15Zr, which gradually increased during the immersion course, similar to those observed in a H_2O_2 free system. Figure 4-8 shows the OCP at 1 h as a function of Zr concentration. It can be seen that in both solutions, the OCP is significantly higher in the presence of H_2O_2. Both in the presence and absence of H_2O_2, addition of 5% Zr decreases the OCP significantly, with a further decrease for Ti15Zr, and smaller decreases for higher Zr levels.

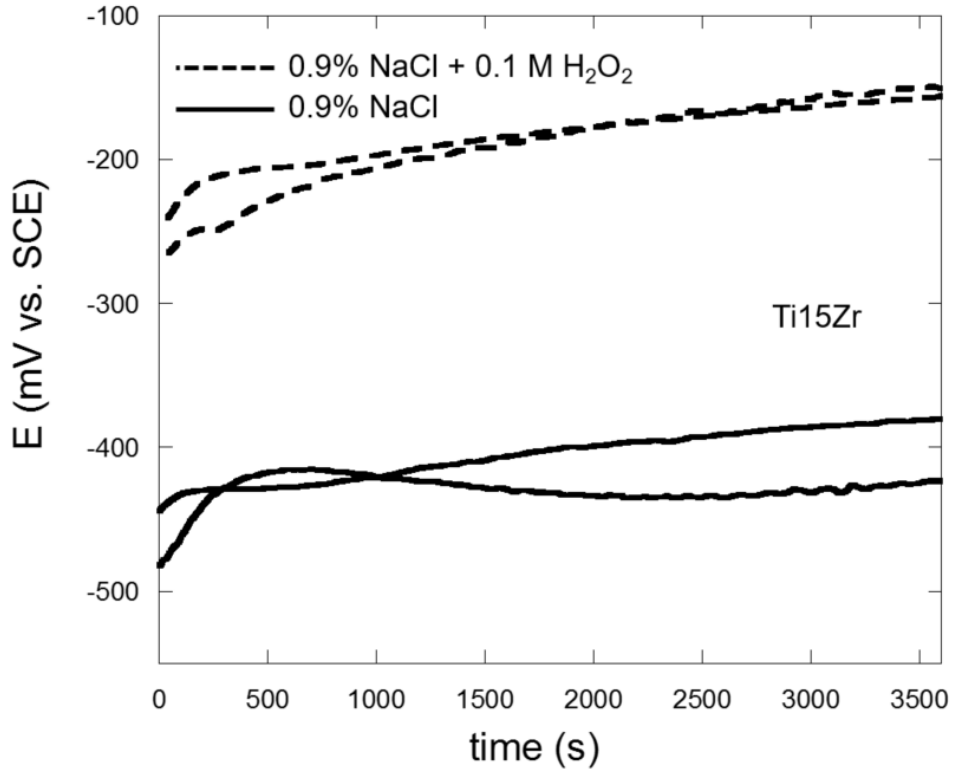

Figure 4-7. Open Circuit potentials of Ti15Zr after 1 h immersion in 0.9% NaCl with and without addition of 0.1 M H_2O_2 at 37 °C.

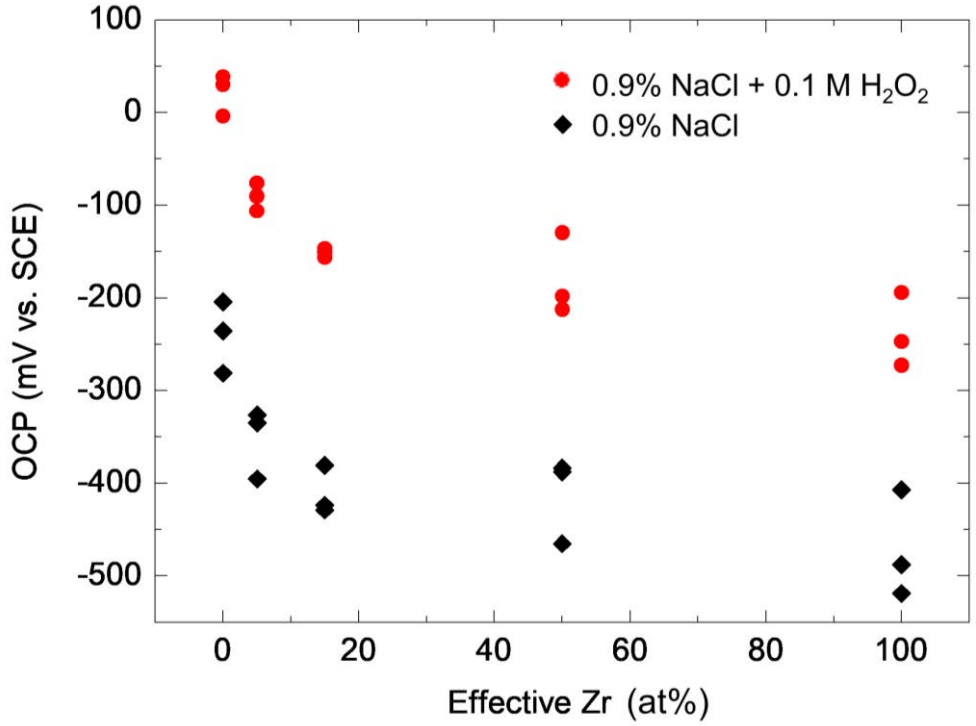

Figure 4-8. OCPs of CP Ti, TiZr binary alloys (Ti5Zr, Ti15Zr, Ti50Zr) and CP Zr in physiological saline (0.9% NaCl) with or without addition of 0.1 M H_2O_2 after 1h immersion at 37°C. The x-axis is the effective Zr concentration (at%) in each tested alloy. All data is shown.

Anodic polarisation curves of CP Ti, TiZr alloys and CP Zr were measured in 0.9% NaCl solutions with and without addition of H_2O_2 (Figure 4-5). In 0.9% NaCl solution alone, it was found that CP Ti, Ti5Zr and Ti15Zr showed spontaneous passivation with passive current densities at a similar level (5 µA/cm^2) and no anodic breakdown was observed for potentials up to 1000 mV. Ti50Zr and CP Zr also showed spontaneous passivation with a similar passive current density but both were susceptible to pitting at potentials > 500 mV. In 0.9% NaCl with addition of 0.1 M H_2O_2, spontaneous passivation was again observed in CP Ti, Ti5Zr and Ti15Zr and the passive current densities were increased by up to 3 µA/cm^2 with respect to the level of 5 µA/cm^2 as observed in the H_2O_2 free solutions. However, for Ti50Zr and

CP Zr, such increases were not observed and passive current densities were slightly reduced compared with these in the H_2O_2 free solutions. Pitting behaviour was observed at high potentials (close to 1000 mV) in both Ti50Zr and CP Zr, indicating a similar susceptibility of anodic breakdown of the passive films in 0.9% NaCl regardless of the presence or absence of H_2O_2.

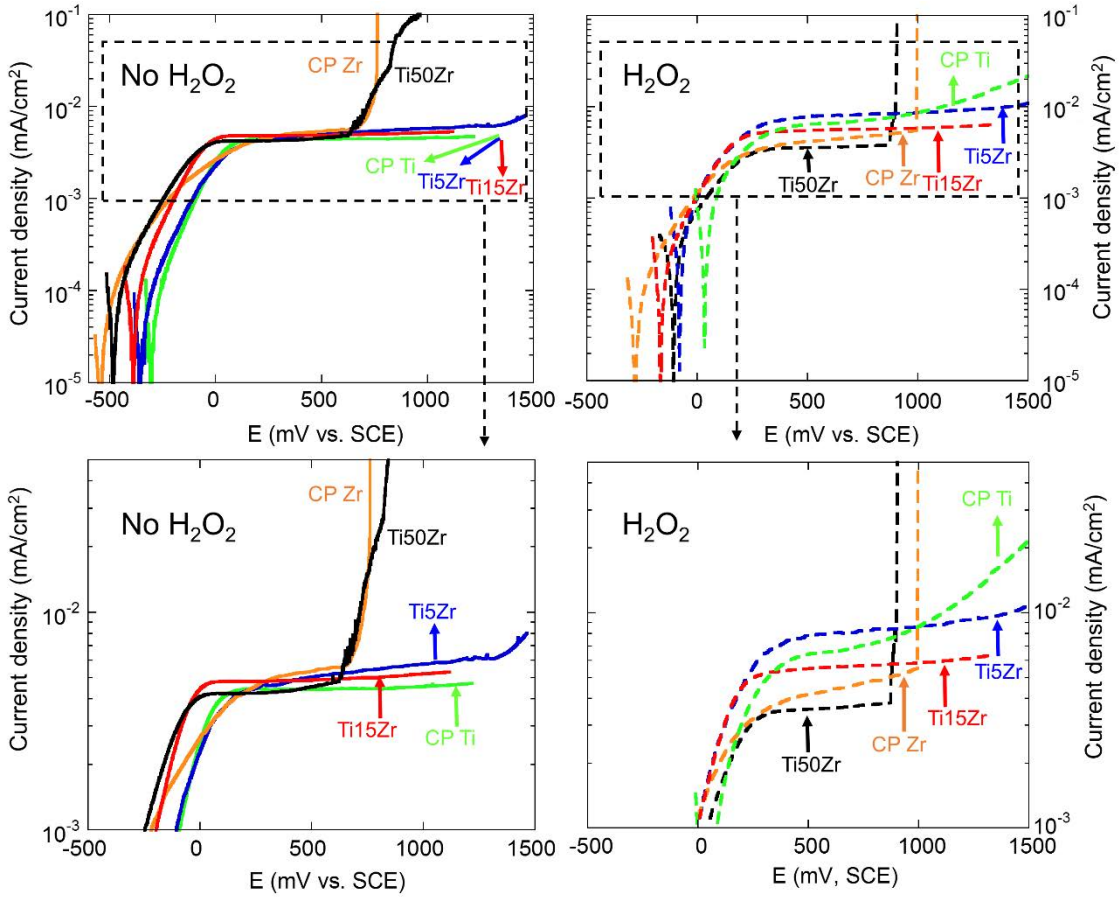

Figure 4-9. Anodic Polarisation of CP Ti, Ti5Zr, Ti15Zr, Ti50Zr alloys and CP Zr in 0.9% NaCl with and without addition of 0.1 M H_2O_2 at 37 °C after 1 h immersion at OCP. Scan rate was 1 mV/s.

Cathodic polarisations of CP Ti, TiZr alloys and CP Zr were measured in 0.9% NaCl with and without addition of H_2O_2, and are shown in Figure 4-10. It was observed that in 0.9% NaCl alone, the addition of Zr to Ti reduced the cathodic current density. In 0.9% NaCl with the addition of 0.1 M H_2O_2, the rates for cathodic reactions were increased for all alloys due to reduction of H_2O_2.

Addition of Zr to Ti decreased the cathodic reaction rates in solutions of 0.9% NaCl containing H_2O_2.

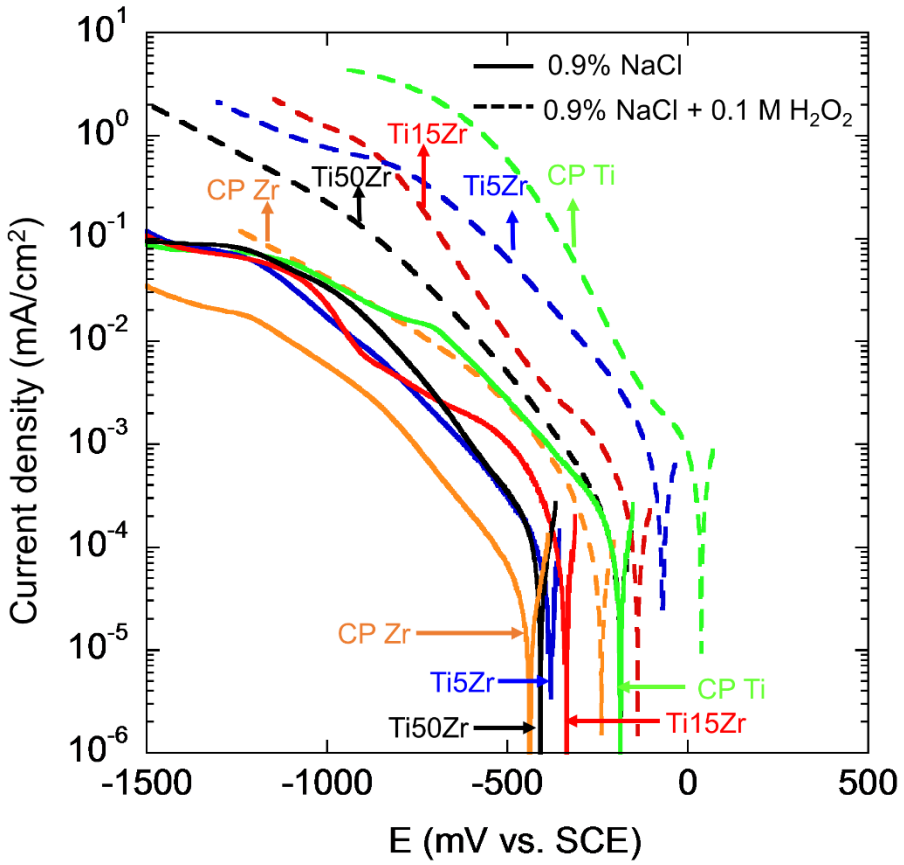

Figure 4-10. Cathodic polarisation of CP Ti, Ti5Zr, Ti15Zr, Ti50Zr alloys and CP Zr in 0.9% NaCl, with and without addition of 0.1 M H_2O_2, at 37 °C after 1 h immersion at OCP. Scan rate was 1 mV/s.

Potentiostatic polarisation measurements of CP Ti and binary TiZr alloys were carried out in 0.9% NaCl at 500 mV (vs. SCE) which is a potential in the passive region (for all substrates) according to previous anodic polarisation measurements (Figure 4-9). At ~1000 s, in some cases H_2O_2 was added to give a final concentration of 0.1 M H_2O_2 in 0.9% NaCl, and all solutions were stirred at this point. CP Zr underwent pitting after polarisation and is therefore not included in Figure 4-11. For all alloys in solutions that were only stirred, without addition of H_2O_2 (solid lines in Figure 4-11), the current density continued to

decrease, consistent with a growing passive film. When H_2O_2 was added, the current densities for CP Ti and Ti5Zr started to increase (broken lines in Figure 4-11), suggesting that the passive films became less protective. The increase in current density following addition of H_2O_2 was less for Ti15Zr, and for Ti-50Zr, the effect of H_2O_2 was completely suppressed.

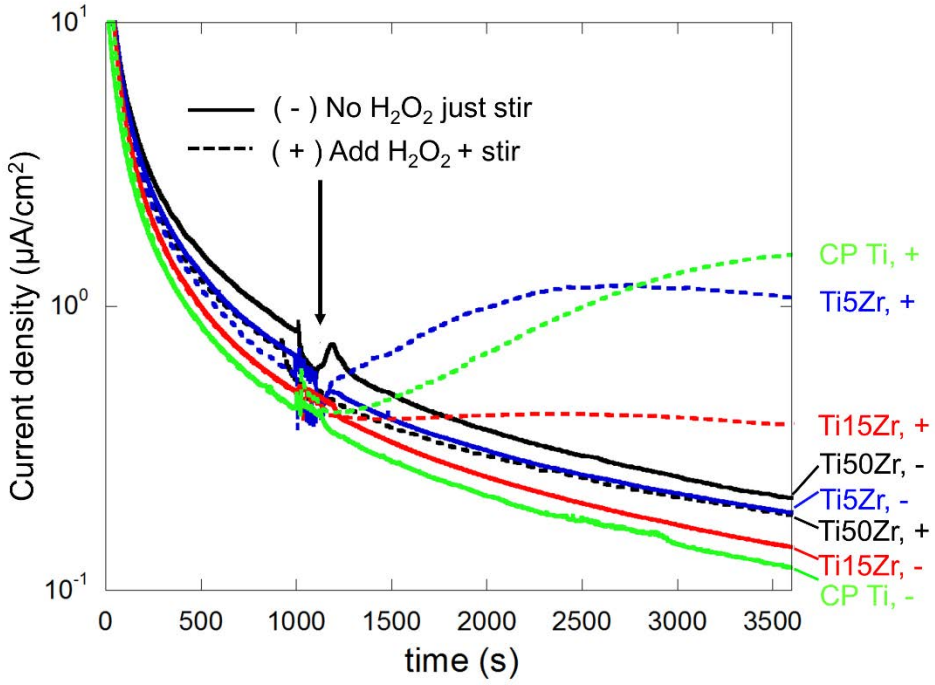

Figure 4-11. Current density as a function of time for CP Ti, Ti5Zr, Ti15Zr, Ti50Zr and CP Zr under potentiostatic control at 500 mV (vs. SCE) in 0.9% NaCl after 1 h immersion at OCP, 37 °C. For some experiments, H_2O_2 was added to the solution to give a final concentration of 0.1 M H_2O_2 at 1000 s (broken lines), and in all experiments, the solution was stirred just after 1000 s.

4.5 Metal ion release associated with THP-1 culture

4.5.1 THP-1 cell adherence

Unstimulated THP-1 cells cultured on the surfaces of CP Ti, TiZr binary alloys and CP Zr and were found to be adherent after 7 days of incubation (Figure 4-12 (a), (d), (g), (j), (m)). The morphology of adherent THP-1 cells was

observed to be clustered, and circular-shaped (Figure 4-12 (c), (f), (i)). Spreading of the cells can be seen in Figure 4-12 (l) and (o), demonstrating distinct lamellopodial extensions (151). Quantitative image analysis of adherent THP-1 cells on Ti, Zr, TiZr surfaces confirmed minor differences in surface coverage between different substrates, varying from 74% to 92% between the five types of alloys.

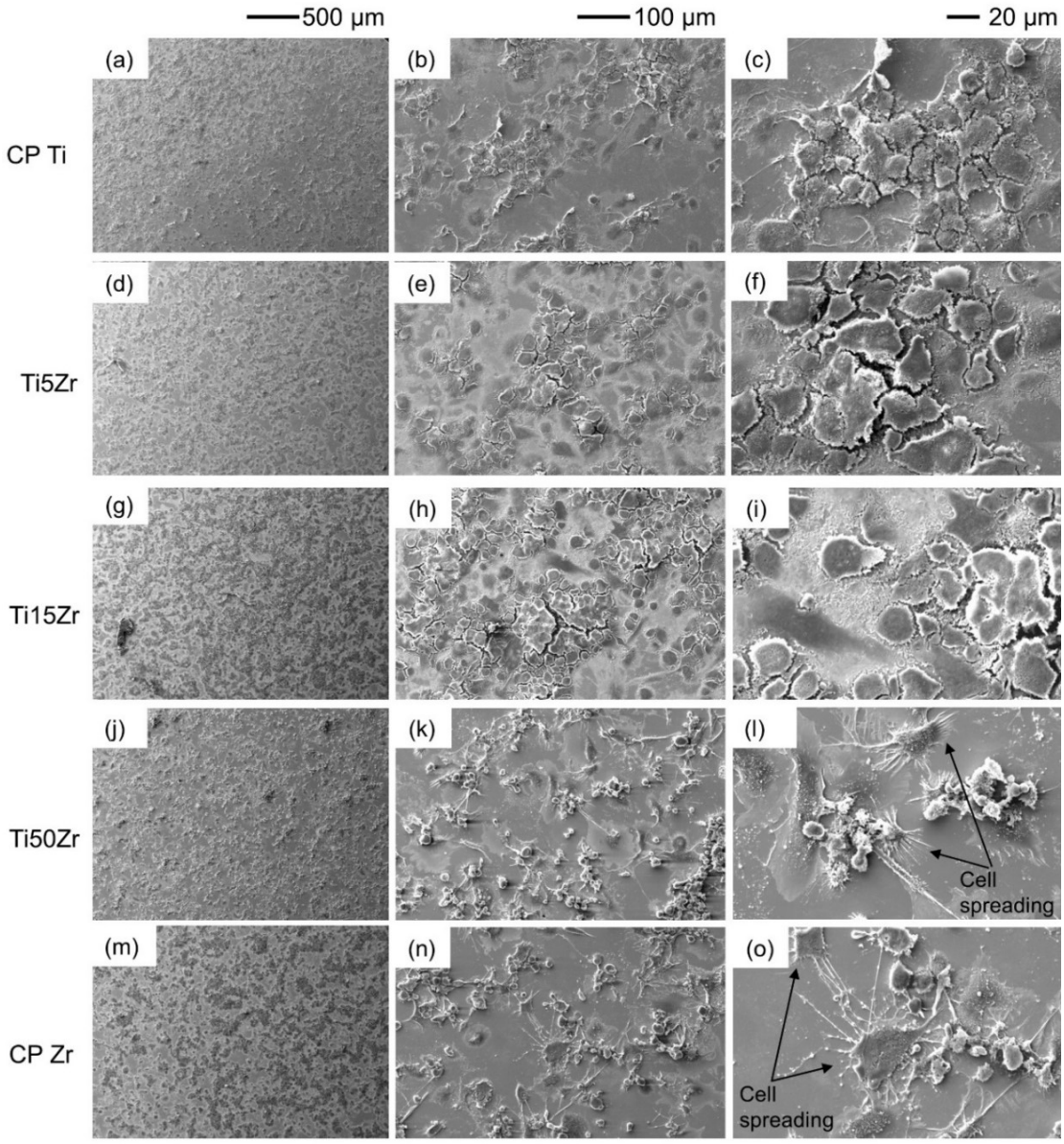

Figure 4-12. SEM images of unstimulated THP-1 cells cultured on mirror polished surfaces of CP Ti (a)-(c), Ti5Zr (d)-(f), Ti15Zr (g)-(i), Ti50Zr (j)-(l) and CP Zr (m)-(o) after incubation in RMPI 1640 medium (with addition of 10% fetal calf serum, phorbol 12 myristate 13 acetate (PMA) (10 ng/mL), penicillin (100 units/mL), streptomycin (100 µg/mL), amphotericin B (2.5 µg/mL)) for 7 days at 37 °C.

4.5.2 Morphology and surface coverage of M1 and M2 phenotypes of THP-1 cells

Figure 4-13 shows the morphology of undifferentiated THP-1 cells, THP-1 cells differentiated into a M1 or M2 phenotype after culturing on CP Ti discs for 24 h.

It can be found that induction of the M1 phenotype of THP-1 cells by stimulating with LPS and cytokine IFN-γ, caused the cells to flatten in round and circular shapes. Induction of the M2 phenotype of THP-1 cells by stimulating with the cytokine IL-4, caused the cells to elongate. Therefore, it is evident that induction of THP-1 cell phenotypes produced different adherent cell morphologies.

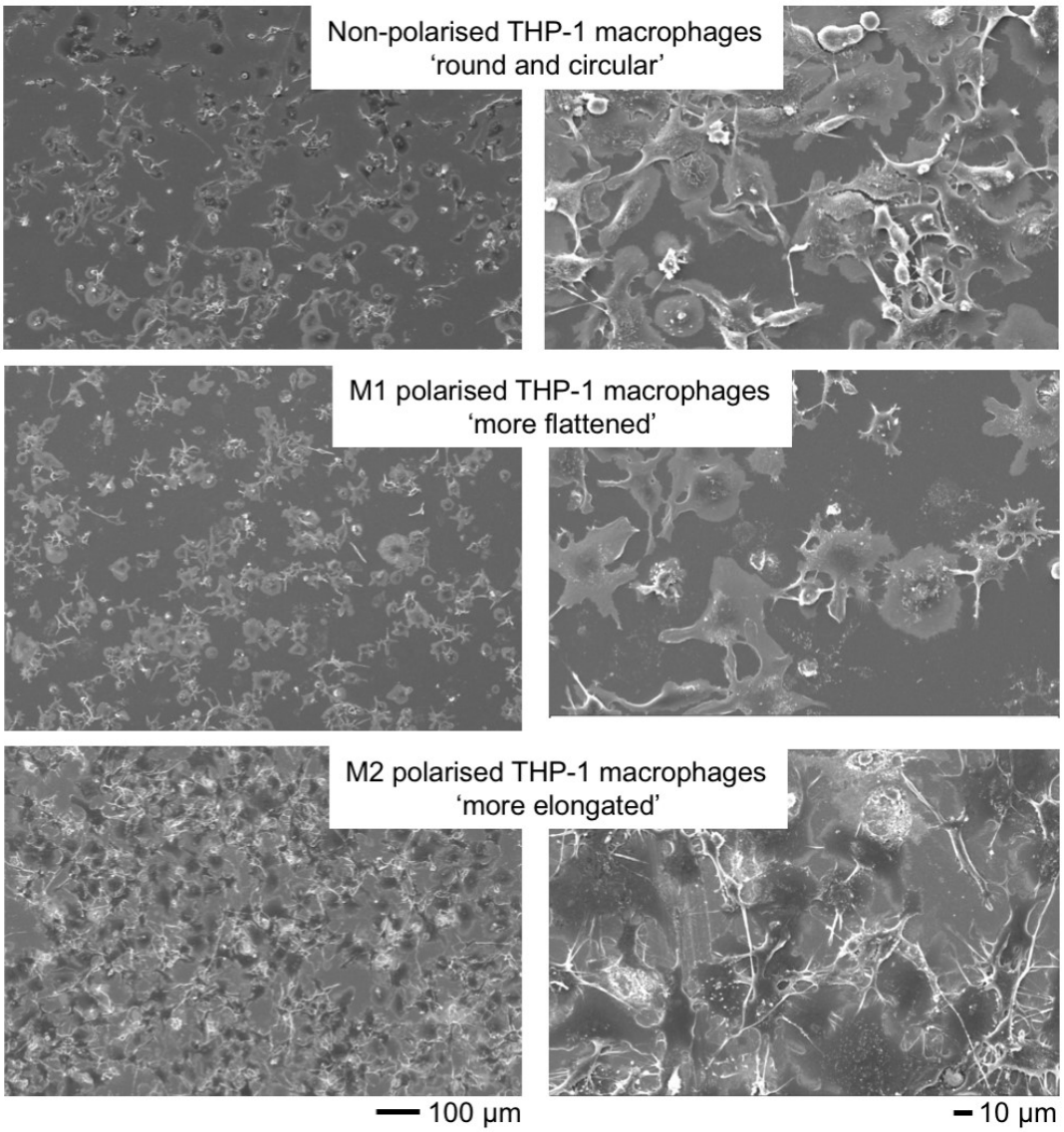

Figure 4-13. SEM images of unstimulated THP-1 cells, the stimulated M1 and M2 THP-1 cells after culturing on CP Ti surface for 24 h.

Quantitative image analysis was conducted to reveal differences in surface coverage associated with the different morphologies. Figure 4-14 shows SEM

images of M1 and M2 phenotypes of THP-1 cells before and after image segmentation. It can be observed that the M1 cells (Figure 4-14a) were accurately detected from the surface by segmentation (marked in blue, Figure 4-14b), and similarly for M2 phenotype Figure 4-14c and Figure 4-14d). The cell coverage was calculated from the segmentation images and average coverage area of M1 and M2 cells are shown in Figure 4-15. It was shown that the M1 cells exhibited surface coverage of 50% $\pm$ 13%, which was statistically lower than that of M2 phenotype which was 82% $\pm$ 2% (p=0.02).

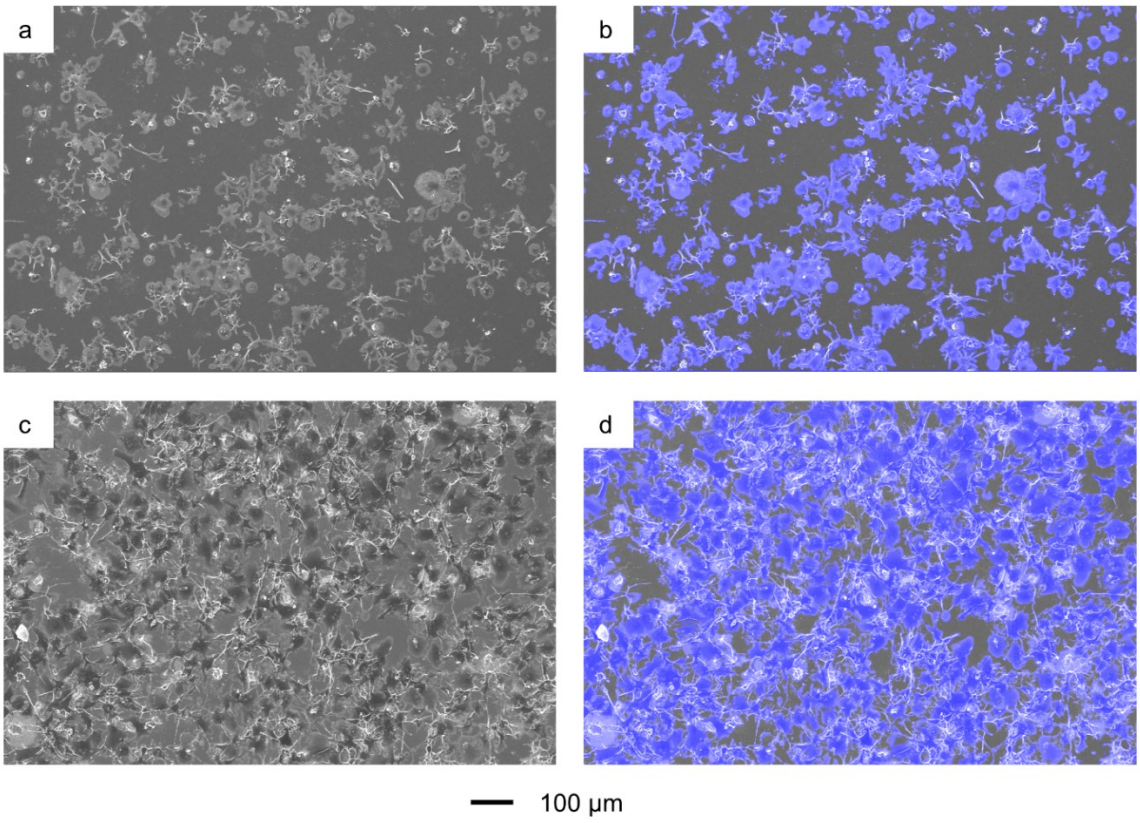

Figure 4-14. SEM images of (a) M1 phenotypes of THP-1 cells on CP Ti metal substrates. b) Overlay of the segmented area (blue) of M1 cells showing accuracy of detection. c) M2 phenotypes of THP-1 cells and d) overlay of the segmented M2 cell area (blue).

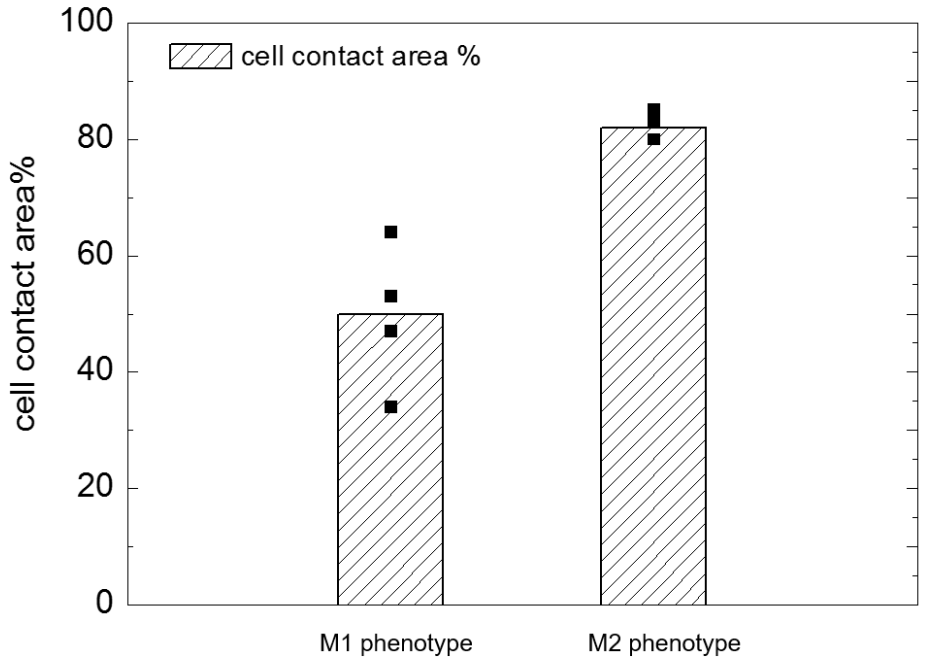

Figure 4-15. Averaged surface area of M1 and M2 phenotypes of THP-1 cells with statistically difference at p=0.02. Symbols represent each individual image analysis.

4.5.3 Cellular induced metal ion release

Figure 4-16 and Table 4-1 summarise metal release detected by ICP-MS from CP Ti, TiZr alloys and CP Zr after 13 days incubation in cell culture medium with and without THP-1 cells differentiated into M1 or M2 phenotypes. It can be seen from Figure 4-16 that in the media and metal-free cell culture controls, no Zr and negligible amounts of Ti were detected. The negligible amounts of Ti might be sourced from trace element contamination in the cell culture medium (from batch to batch) and/or fetal bovine serum which varies in purity in different grades due to the contamination with trace metal elements.

In the case of culture medium alone with no cells, Ti release was found to be the highest from CP Ti, and progressively reduced with increasing Zr content. A negligible amount was detected from CP Zr which might come from minor Ti

contamination in the medium. Zr release was found to be under the limit of detection from CP Ti, Ti5Zr and Ti15Zr. From Ti50Zr and CP Zr, Zr only showed minimal release, and increased with increasing Zr concentrations in the alloy.

For metal substrates incubated in the presence of M1 phenotype THP-1 cells, Ti metal release was found to be increased from CP Ti and all TiZr grades, compared with those in medium alone. Furthermore, it was found that Ti release was progressively reduced with increasing Zr concentrations. Zr release was close to or under the limits of detection for CP Ti, Ti5Zr and Ti15Zr. Zr release from Ti50Zr and CP Zr, was increased relative to equivalent samples incubated in cell-free conditions.

For metal substrates incubated in the presence of M2 phenotype THP-1 cells, Ti release was increased from CP Ti at levels approaching two folds the levels detected following culture with a M1 phenotype. Ti release reduced progressively from Ti5Zr to Ti50Zr. Zr release remained at low levels for Ti5Zr and Ti15Zr. Ti50Zr showed similar amount of Zr release compared with that in the presence of M1 cells, and CP Zr showed increased release in comparison with that in the presence of M1 cells.

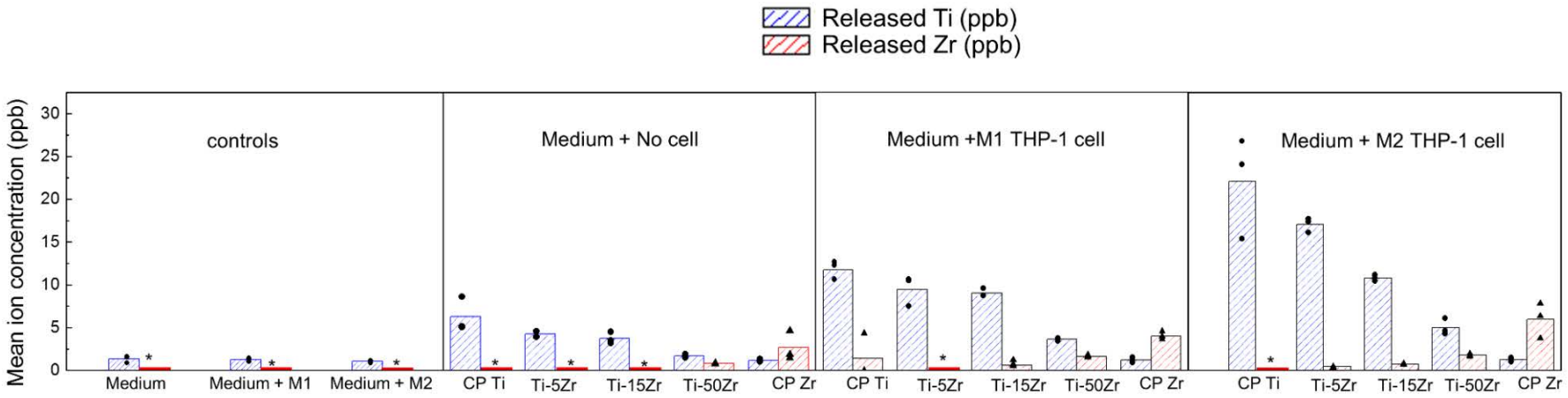

Figure 4-16. Mean concentrations (ppb) of Ti and Zr ion release from CP Ti, TiZr alloys and CP Zr in 3.4 mL RPMI-1640 cell medium with absence or presence of M1 and M2 phenotypes THP-1 cells for 13 days at 37 °C, 5% CO_2, 100% humidity. Individual measurement from each mass spectroscopy assay was indicated with symbols (square symbol for Ti, and triangle symbol for Zr). Flat columns marked with asterisks refer to Zr concentrations below the Zr detection limit of 0.4 ppb. Detection limit for Ti is 0.3 ppb.

Table 4-1 Mean concentrations with the range from individual measurements of Ti and Zr release (ppb) from CP Ti, Ti5Zr, Ti15Zr, Ti50Zr, CP Zr discs under each condition for 13 days at 37 °C, 5% CO_2, and 100% humidity.

Incubation conditions		Ti	Zr
No metal disc controls	Medium	1.4 (0.9 – 1.6)	0
	Medium + M1 THP-1 cells	1.3 (1.0 – 1.4)	0
	Medium + M2 THP-2 cells	1.1 (0.9 – 1.2)	0
Medium + metal discs	CP Ti	6.3 (5.1 – 8.6)	< 0.4
	Ti5Zr	4.3 (3.9 – 4.6)	<0.4
	Ti15Zr	3.8 (3.2 – 4.5)	<0.4
	Ti50Zr	1.7 (1.5 – 1.9)	0.8 (0.8 – 0.9)
	CP Zr	1.2 (1.0 – 1.3)	2.7 (1.5 – 4.7)
Medium + M1 THP-1 cells + metal discs	CP Ti	11.7 (10.5 – 12.5)	1.4 (0 – 4.2)
	Ti5Zr	9.4 (7.4 – 10.5)	<0.4
	Ti15Zr	9.0 (8.6 – 9.5)	0.6 (0.5 – 0.7)
	Ti50Zr	3.6 (3.4 – 3.7)	1.6 (1.5 – 1.8)
	CP Zr	1.2 (0.9 – 1.5)	4.0 (3.6 – 4.5)
Medium + M2 THP-1 cells + metal discs	CP Ti	22.1 (15.4 – 26.8)	<0.35
	Ti5Zr	17.1 (16.1 – 17.7)	0.4 (0.4 – 0.5)
	Ti15Zr	10.8 (10.5 – 11.2)	0.8 (0.7 – 0.8)
	Ti50Zr	5 (4.3 – 6.1)	1.8 (1.6 – 2.0)
	CP Zr	1.3 (1.0 – 1.5)	6.0 (3.7 – 7.8)

Figure 4-17 shows normalised Ti release (by concentration, at%, for each alloy) from CP Ti, Ti5Zr, Ti15Zr and Ti50Zr. Ti release from CP Ti and TiZr alloys (5, 15 and 50% Zr) (normalised to elemental %) in cell culture and cell-free media are shown in Figure 4-17a. In the presence of M2 THP-1 cells, Ti release from all metal discs was increased relative to M1 THP-1 cells. Moreover, with increasing Zr additions (from 5 to 50%), the normalised Ti release was shown to be progressively reduced. The sum of Ti release following culture with both M1 or M2 THP-1 cells demonstrated a clear pattern of reduced corrosion, with increasing addition of Zr. Normalised Zr release from TiZr alloys (5, 15 and 50% Zr) and CP Zr is shown in Figure 4-17b. Zr release was shown to be reduced relative to Ti when data was normalised to the at% composition of each exposed alloy.

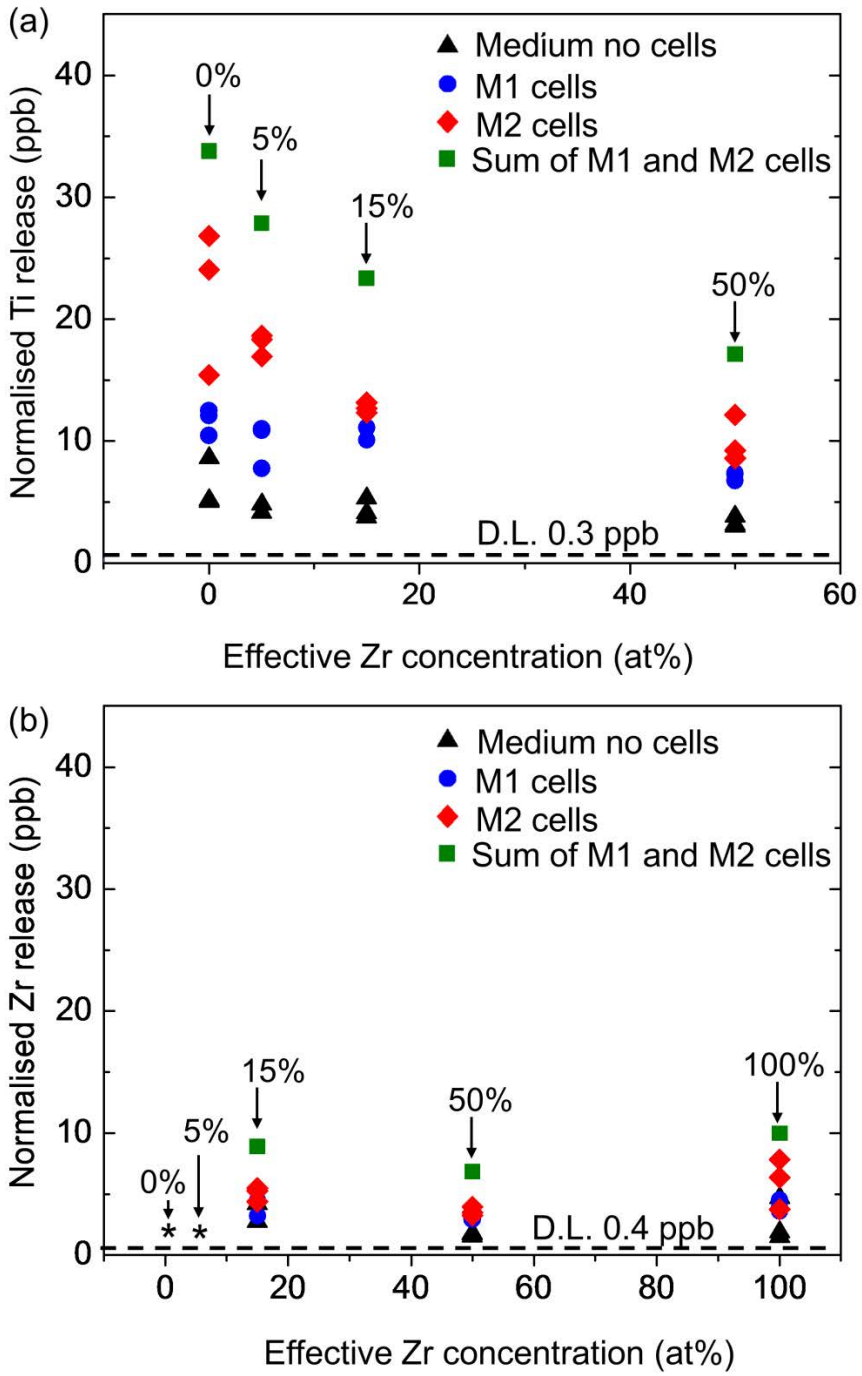

Figure 4-17. Normalised (by concentration, at%, in respective alloys) (a) Ti release (ppb) (b) Zr release (ppb) from immersed alloys CP Ti, Ti5Zr, Ti15Zr, Ti50Zr and CP Zr after 13 days of incubation in RPMI 1640 medium with or without addition of M1 or M2 phenotype THP-1 cells at 37 °C, 5% CO_2, 100% humidity. All data shown (n=3). Sum of M1 and M2 THP1 cells are total of two average values of metal releases under M1 or M2 conditions. Detection limit (D.L.) was 0.3 ppb for Ti and 0.4 ppb for Zr. Marker (*) indicates measurements made for CP Ti (0%) and Ti5Zr (5%) were below the detection limit.

4.6 Discussion

4.6.1 Zr reduces the passive current density of Ti in HCl solutions

Previously it has been established that Ti oxides became destabilised when exposed to concentrated reducing acids like HCl (77), and the addition of 50% Zr to Ti improved its oxide stability at open circuit (74) and increased its resistance to dissolution at lower potentials (44). The present work is consistent and supports previous findings, and additionally, it provides an overview of the effect of systematic additions of Zr on corrosion of Ti in acidic environments.

Figure 4-4 showed different changes in OCPs of CP Ti, binary TiZr alloys and Zr following immersion in 2 M HCl solutions for 1 h. The abrupt drops of the OCP for CP Ti are likely to be associated with chemical dissolution of the surface oxide film and the plateau of potential at approximately -650 mV is associated with ‘surface activation’, where upon the bare metal surface is exposed leading to active dissolution (77, 80). From an E-pH diagram of a Ti-H_2O system at 37 °C (76), it was observed that at the stabilised potential for CP Ti at approximately -650 mV, the thermodynamic stable form of Ti is ionic which is consistent with its active dissolution behaviour. Addition of 5 at% Zr (Ti5Zr) delayed the abrupt decrease in OCP suggesting a delayed ‘surface activation’, followed by the plateau of potentials at -600 mV at which ionic form of Ti is stable (76). Addition of 15 at% Zr (Ti15Zr) showed gradual decreases in OCPs down to -400 mV without the steep drops, suggesting an inhibited ‘surface activation’, and the potentials were found in the passivation region (TiO_2) from E-pH diagram (76). Addition of 50 at% Zr (Ti50Zr) in contrast

resulted in an increase in potential, similar to that of CP Zr, suggesting spontaneous passivation. According to the E-pH diagram of Zr-H_2O (78), the thermodynamic stable state of Zr at OCPs of Ti50Zr and CP Zr (-300 mV and -200 mV respectively, Figure 4-4) are found in aqueous Zr^{4+} rather than oxide form i.e. ZrO_2. Therefore, it is suggested that air-formed Zr oxides are kinetically resistant to chemical dissolution (77).

It can be concluded that increasing Zr additions systemically improved the oxide film stability of Ti in 2 M HCl solutions at open circuit conditions, supporting previous findings (77). It was proposed by Yu et al. (77) that the beneficial effect of the Zr addition to Ti is due to the presence of ZrO_2, which has been demonstrated with a slower chemical dissolution rate when compared with TiO_2 in HCl solutions.

From Figure 4-5, it was found that CP Ti exhibited a clear active passive transition on anodic polarisation after 1 h immersion at OCP. The active dissolution behaviour of CP Ti was observed at low potentials. Addition of 5 at% Zr suppressed the active dissolution peaks and was observed as a decrease in the critical current densities indicating an increased resistance to dissolution. Similar effects were also reported by Yu et al., where a reduced i_{crit} was exhibited by Ti-50Zr (wt%) compared with CP Ti in deaerated 5 M HCl at 37 °C (44). For 15 at% Zr and above (Figure 4-5), the surface oxide films following immersion at OCP in 2 M HCl were preserved, resulting in spontaneous passivation following anodic polarisation.

4.6.2 Zr contents increased corrosion resistance of CP Ti in physiological saline with H_2O_2

At open circuit conditions, spontaneous passivation was observed for the five types of alloys in 0.9% NaCl solutions with and without addition of 0.1 M H_2O_2. The addition of H_2O_2 increased the OCP of all alloys (Figure 4-7) which was attributed to the enhanced rates of the cathodic reactions (Figure 4-10) since H_2O_2 is a strong oxidant (17). Increasing Zr additions in Ti progressively reduced the potentials in both H_2O_2 free and H_2O_2 containing electrolytes. This was due to the reduced cathodic reactivity with increasing in Zr levels (Figure 4-10), which is likely to be a result of the formation of a thicker and less conductive oxide.

It is well-established that H_2O_2 enhances the corrosion of Ti (19-22, 86, 87) via a complexation reaction with its surface oxides. Consistently in the present work, higher passive densities of Ti were observed in the presence of H_2O_2 under both potentiostatic and potentiodynamic polarisations (Figure 4-9 and Figure 4-11). Similar increases in passive current densities were observed for both Ti5Zr and Ti15Zr but were reduced in scale (Figure 4-9). In addition, from Figure 4-11, it can be seen that increasing additions of Zr (from 5, 15 to 50%) in Ti progressively supressed the impact of H_2O_2 on the rise in passive current density, until a complete passivation behaviour observed with Ti-50%Zr alloy. It appears that Zr and/or Zr oxides are not susceptible to complexation by H_2O_2 therefore protect the surface oxides of TiZr alloys from deterioration, by forming Zr-rich oxide films that are resistant to dissolution.

4.6.3 Increased pitting susceptibility by higher Zr concentrations to Ti

An increased pitting susceptibility was found in Ti50Zr and CP Zr in both HCl solutions and in neutral 0.9% NaCl solutions with and without addition of H_2O_2 (Figure 4-5 and Figure 4-9). In 2 M HCl solutions (Figure 4-5), Ti50Zr exhibited pitting (passive film breakdown) susceptibility at potentials >500 mV while much lower pitting potentials (approximately at 100 mV) were found for CP Zr. Pits on the surface of Ti50Zr (Figure 4-6) were found to be initiated and/or propagated from the edge of the sample, indicating a potential role of crevice corrosion in these pitting events. On CP Zr, pits were found randomly distributed on the surface and initiation could be associated with the presence of Fe-enriched second phase particles as shown in Figure 4-3. The morphology of pits found on CP Zr were circular in shape, compared with facet boundaries seen on the surface of Ti50Zr. The facet boundaries and acicular structures inside the pit mirrored the as-polished and etched structures shown in optical (Figure 4-1) and BSE images (Figure 4-2), indicating an etching effect on pit propagation. Inside the pits on CP Zr surface, rough morphologies were observed suggesting dissolution is associated with a localised roughening process. In neutral saline solutions with and without addition of H_2O_2 (Figure 4-9), both Ti50Zr and CPZr exhibited similar pitting susceptibility at potentials >500 mV.

4.6.4 Zr additions enhance cell mediated corrosion resistance

Corrosion mediated by the contents of microenvironments between eukaryotic or prokaryotic cells and implant surfaces has been associated with implant degradation *in vivo* (13, 14, 119). Cell mediated corrosion has been linked to

cellular production of ROS species, including superoxide anions and H_2O_2 released or formed in the environmental niche between a metal surface and the adhered cells (13, 14). The presence of adherent THP-1 cells resulted in both Ti and Zr release (Figure 4-16).

Different functional phenotypes of THP-1 cells resulted in differences in metal releases. M1 or M2 macrophage phenotypes are distinguished by their different ability to produce inflammatory cytokines as well as oxygen and nitrogen radials (152). The pro-inflammatory M1 state is a classically activated state with enhanced microbiocidal activities including ROS production (to increase killing ability) (152, 153). The M2 state is associated with a wound-healing phenotype of macrophages, which is less efficient in producing ROS species (152). Surprisingly, Ti release was found to be higher in the presence of THP-1 cells in their M2 state when compared with the activated M1 state (Figure 4-17). It is worth pointing out the activity of the cells and ROS release are directly associated with functional activity such as phagocytosis (14), which was not simulated in this study. In addition, the extracellular chemistry in complex in nature (152) and the concentration of ROS species such as H_2O_2 can vary with time and spatially (85). The enhanced metal ion release by M2 cells in this study is most likely attributed to the significantly higher surface coverage observed by the cells on the metal surface (Figure 4-15). It was found that M2 cells induced Ti dissolution was supressed progressively by addition of Zr (Figure 4-17), similarly shown in the sum of averaged metal release induced by M1 and M2 cells, which was found to be entirely consistent with inhibiting effect

of Zr addition on dissolution of Ti in the presence of H_2O_2 (Figure 4-11) and in HCl solutions (Figure 4-4 and Figure 4-5).

4.7 Conclusion

1. In acidic environments (2 M HCl), addition of Zr inhibits surface activation and enhances oxide film stability of Ti at OCP. Furthermore, addition of Zr suppresses active dissolution and reduces the passive current density of Ti under anodic polarisation.
2. In physiological electrolytes (0.9% NaCl), addition of Zr to Ti suppresses OCP by reducing the rate of cathodic reactions without significantly altering anodic polarisation. On addition of H_2O_2 (representative of a more inflammatory environment), the increased OCPs of CP Ti were reduced by alloying with Zr via decreasing the rate of its cathodic reactions. The enhanced passive current densities of CP Ti induced by H_2O_2 under anodic polarisation was reduced by Zr additions, which were further confirmed by passive dissolution at a controlled potential. Passivation of CP Ti at the controlled potential was destabilised by the presence of H_2O_2 leading to enhanced dissolution, which was supressed progressively by increasing Zr additions suggesting a better resistance to dissolution. Higher addition of Zr e.g. 50 at% in Ti as well as CP Zr were susceptible to pitting in acidic HCl solutions and neutral solutions 0.9% NaCl with presence and absence of H_2O_2.
3. Ti release from CP Ti and TiZr binary alloys was induced by the presence of adherent THP-1 cells (both in pro-inflammatory M1 state and ’tissue healing’ M2 state). The magnitude of metal release was reduced with increasing Zr content and the pattern of corrosion behaviour was consistent with electrochemical measurements.

4. Systematic addition of Zr to Ti has been demonstrated to progressively enhance Ti passivity, however, caution needs to be taken when considering higher Zr concentrations due to an increased susceptibility to pitting corrosion. Optimisation of composition should be based on both passivity and pitting resistance such as Ti15Zr found in this study.

5 SYNERGISTIC EFFECTS OF ALBUMIN AND H_2O_2 ON CORROSION OF TI6AL4V

5.1 Introduction

The aim of the work described in this chapter is to study the synergistic effect of albumin and H_2O_2 on the corrosion of Ti6Al4V in physiological saline (i.e.0.9% NaCl). It has been previously shown by Yu et al. that a combination of H_2O_2, an inflammatory biomolecule found in the immediate implant environment, and albumin, the most abundant protein in tissue fluids, can lead to significantly higher levels of corrosion of Ti6Al4V than exposure to either species alone (17). However, the mechanisms underpinning this behaviour are not fully understood. It has been shown that albumin inhibits corrosion during short-term electrochemical polarisation but long-term metal ion release studies, using mass spectroscopy, have shown that albumin exposure can enhance corrosion (17). The synergistic action of albumin and H_2O_2 on Ti6Al4V corrosion has been previously explained, by a proposed mixed potential theory, where an “active” dissolution region has been proposed at low potentials, where adsorption of albumin would supress the corrosion potential taking it into more “active” region of Ti (17). The rationale behind the work is to understand the mechanism underpinning the synergistic effect of albumin and H_2O_2 on corrosion of Ti6Al4V as a function of time. The mechanism proposed by Yu et al. is explored, taking into account temporal effects on corrosion behaviour which were not previously considered.

In this study, both short-term (<24 h) and long-term exposures (up to 120 h) were investigated by electrochemical methods including open circuit potential, potentiodynamic and potentiostatic polarisation and electrochemical impedance spectroscopy (EIS). The surface morphology of H_2O_2 exposed Ti6Al4V oxide films was examined by SEM with EDX analysis, before and after immersion in 0.9% NaCl, containing 0.1% H_2O_2 solutions with and without the addition of albumin. Dissolution of Ti6Al4V was also measured as a function of potential: metal ion release was measured at the constant potentials which were likely to be in the “active” region of dissolution proposed by Yu et al. In parallel, EIS measurements were carried at the static potentials to characterise the metal/oxide/solution interface.

5.2 Corrosion under open circuit conditions

5.2.1 Open circuit potential

Figure 5-1 shows the OCP (open circuit potential or corrosion potential) as a function of time in different solutions. In all cases, the corrosion potential gradually increased, consistent with a decrease in the anodic current density as a consequence of thickening of the oxide film and/or corrosion product layer on the metal surface. The OCP was consistently higher in a solution containing 0.1% H_2O_2 in 0.9% NaCl, compared with that measured in 0.9% NaCl alone. This is likely to be due to an increased cathodic current since H_2O_2 is a strong oxidant (17, 19). In a solution containing 4% albumin combined with 0.1% H_2O_2 in 0.9% NaCl, the OCP was consistently lower than that measured in the presence of NaCl and H_2O_2 alone, but was higher than that measured in NaCl alone. This is consistent with previous work by Yu at al. (17), who showed that the presence of albumin decreases the rate of the cathodic reduction of H_2O_2, probably by adsorption onto the surface.

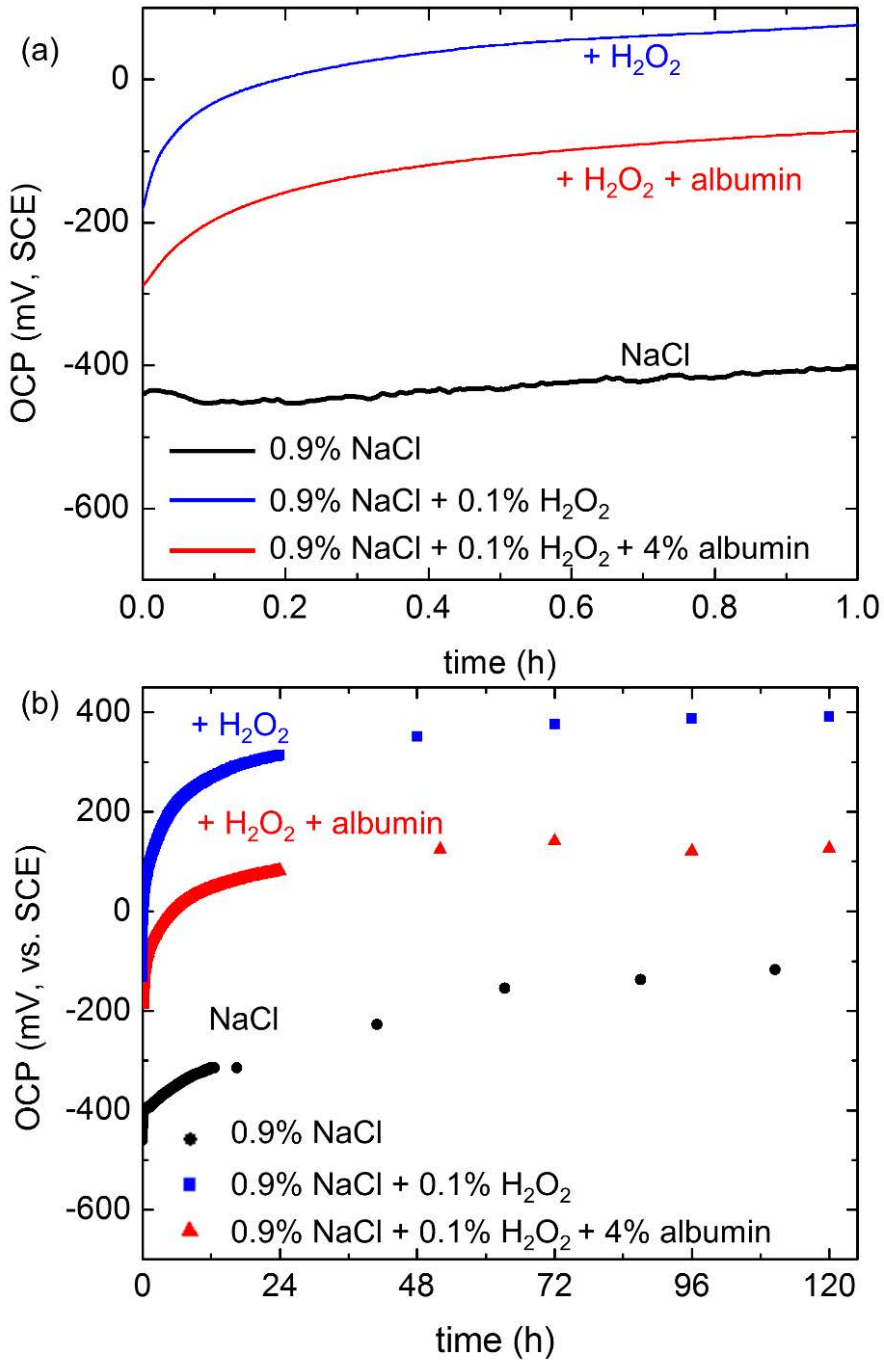

Figure 5-1. Open circuit potentials during exposure of Ti-6Al-4V in 0.9% NaCl with and without addition of 0.1% H_2O_2 or a combination of 0.1% H_2O_2 and 4% albumin at 37°C; exposure for (a) the first hour; (b) 120 h.

5.2.2 Potentiodynamic polarisation

Potentiodynamic polarisation curves can be used to confirm the interpretation of the OCP behaviour. Figure 5-2 shows the anodic polarisation curves in the

same set of solutions as those in Figure 5-1. The order of the open circuit potentials is consistent with that in Figure 5-1. The lowest OCP was observed in NaCl alone, with addition of H_2O_2 leading to a higher potential associated with a higher cathodic reaction rate (consistent with the cathodic polarisation curves shown in reference (17)). The addition of H_2O_2 to NaCl also led to an increase in the anodic reaction rate, above 400 mV (sufficiently above the OCP for the cathodic reaction to be negligible), with a small plateau seen from ~+400 to +600 mV, followed by a steady increase. In the presence of NaCl, H_2O_2 and albumin, the anodic reaction above +400 mV was the same as that for NaCl and H_2O_2 alone, suggesting that albumin caused little or no change in the anodic reaction, but the cathodic reaction appeared to be inhibited, explaining the relative values of the OCP shown in Figure 5-1.

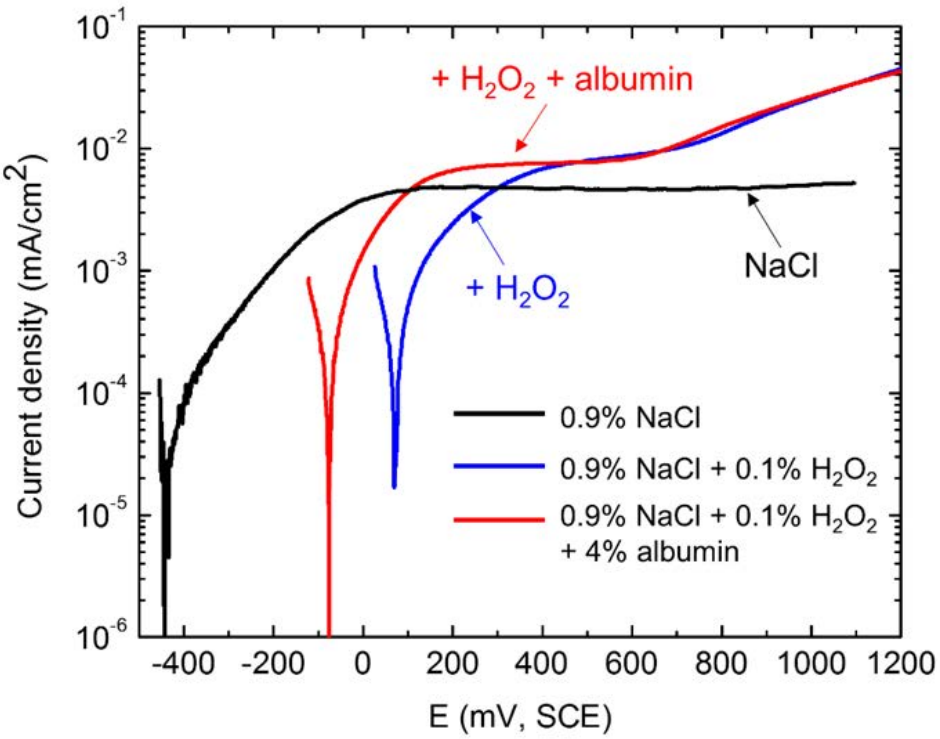

Figure 5-2. Potentiodynamic polarisation of Ti6Al4V after 1 h immersion at OCP in the solutions indicated at 37°C. The scan rate was 1 mV/s.

5.2.3 Electrochemical impedance spectroscopy (EIS)

Figure 5-3 shows the Bode and Nyquist plots of Ti6Al4V after immersion in 0.9% NaCl with and without the addition of H_2O_2 and/or albumin at OCP for 24 h and 120 h. Two-time constants corresponding to the oxide film and likely the (double) layer were observed in the Bode plot after 24 h immersion, although this was less obvious for that in 0.9% NaCl than in the presence of 0.1% H_2O_2 and in the combination of 0.1% H_2O_2 and 4% albumin. Nevertheless, after 120 h immersion, more pronounced two-time constants were observed in all solutions, which could also be associated with a two-layer structured passive film. It was also found that the real part of the impedance (diameter of semicircle in Nyquist plot, indicating the combined resistances of the passive film and the

electrochemical reaction rates at OCP), increased with immersion time which was consistent with their OCP behaviour (Figure 5-1). Furthermore, it was found that the resistance of Ti6Al4V in the presence of both albumin and H_2O_2 in 0.9% NaCl was lower than that observed in the alternative solutions over both of the measured time periods.

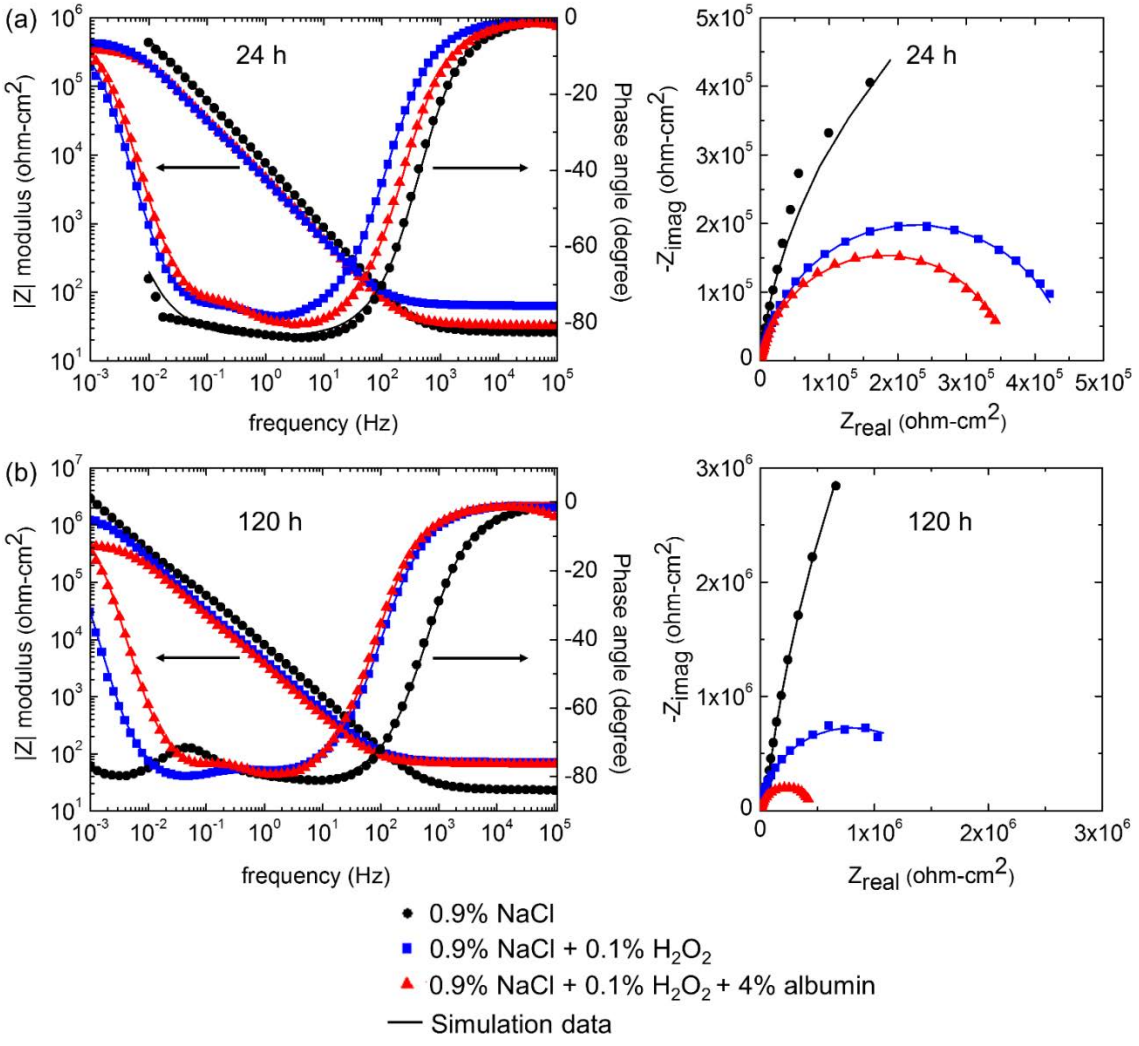

Figure 5-3. Bode and Nyquist plots of Ti6Al4V immersed at OCP in 0.9% NaCl in the absence and presence of 0.1% H_2O_2 and combination of 0.1% H_2O_2 and 4% albumin at 37°C after (a) 24 h and (b) 120 h. Symbols are experimental data and lines are simulated data using the equivalent circuit shown in Figure 3-3.

The data shown in Figure 5-3 were fitted using the equivalent circuit shown in Figure 3-3. The polarisation resistance (R_p) (Figure 5-4) is the sum of two

resistive components R_{hf} (oxide) and R_{lf} (inversely proportional to electrochemical reaction rate). It should be noted that R_p is dominated by R_{hf} (oxide resistance). Figure 5-4 shows that in all solutions, R_p gradually increased with immersion time and subsequently approached steady state after approximately 70 h. It can be seen that the presence of H_2O_2 reduced R_p by more than an order of magnitude after the initial measurement. At 24 h, the value of R_p in the presence of both albumin and H_2O_2 was similar to that observed in the presence of H_2O_2. However, at later time periods (after 120 h immersion), R_p in the presence of albumin and H_2O_2 was significantly (at a half magnitude) lower than that in the presence of H_2O_2 alone, R_p in the presence of H_2O_2 was almost 1 magnitude lower than that in the 0.9% NaCl alone.

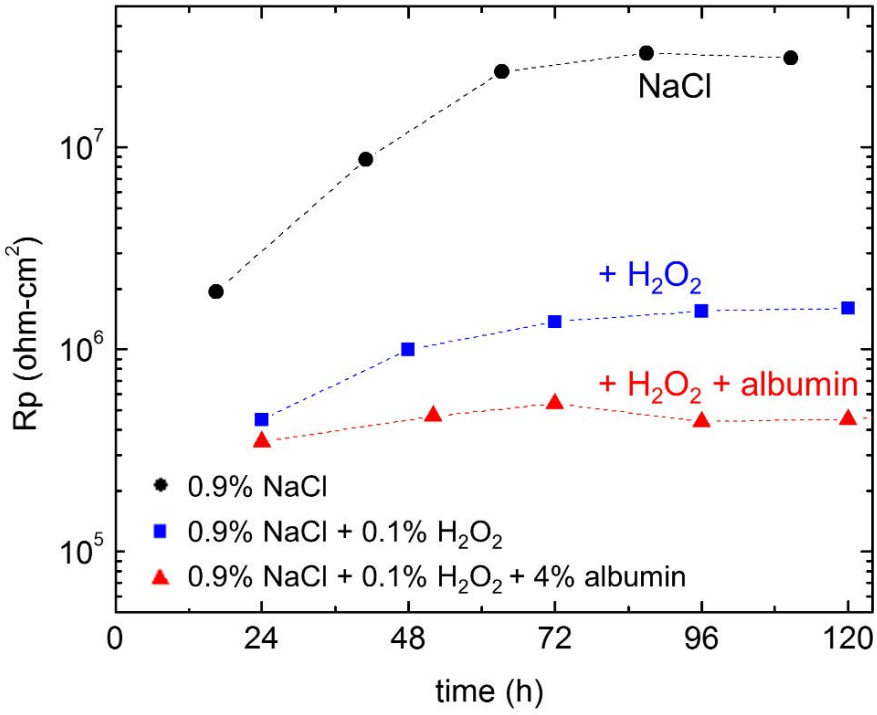

Figure 5-4. Polarisation resistance (R_p) for Ti6Al4V as a function of immersion time in 0.9% NaCl with absence and presence of 0.1% H_2O_2 and combination of 0.1% H_2O_2 and 4% albumin at 37 °C. Values were calculated by fitting the data shown in Figure 5-3 to the equivalent circuit shown in Figure 3-3.

5.2.4 Surface morphology after corrosion

Figure 5-5(a) and (b) show the as-polished surface of Ti6Al4V with a distribution of β phase (identified using EDX, Table 5-1) in an α matrix. Figure 5-5(c) and(d) show secondary electron images of Ti6Al4V after immersion in 0.9% NaCl + 10% H_2O_2 for 3 days at 37 °C. The mud-crack morphology of corrosion products suggests the formation of a thick corrosion product layer. Figure 5-5(e)-(h) show the morphology of surfaces that were pre-treated in the same way as in Figure 5-5(c) and (d) but were then subsequently immersed in 0.9% NaCl + 0.1% H_2O_2 without, (e) and (f), or with, (g) and (h), 4% albumin for 7 days at 37 °C. Figure 5-5(e) and (f) shows similar mud-crack morphology to that observed in Figure 5-5(c) and (d), but it can be seen that in the presence of albumin, Figure 5-5(g) and (h), the thick corrosion product layer was dissolved, and the microstructural features such as the β phase can be observed (confirmed using EDX).

The EDX composition of the α and β phases on the as-polished Ti6Al4V surface are shown in Table 5-1. It can be seen that the α phase is enriched in Al and the β phase is enriched in V. The air-formed surface oxides film was too thin to be detected accurately by EDX. Compositions of corrosion products (white precipitates, Figure 5-5(h)) and oxides on the bulk surface of α and β phases (Figure 5-5(h)) after immersion in the albumin containing solution are also shown. It was observed that the white precipitates found on the surface are mostly Ti oxides. The oxides on the bulk surface contain almost half the oxygen concentration of the white precipitates. It was also found that the vanadium (V)

concentration in the β phase (3.0 wt%) was lower than that of the as-polished surface (9.3 wt%) suggesting that the β phase has been preferentially dissolved.

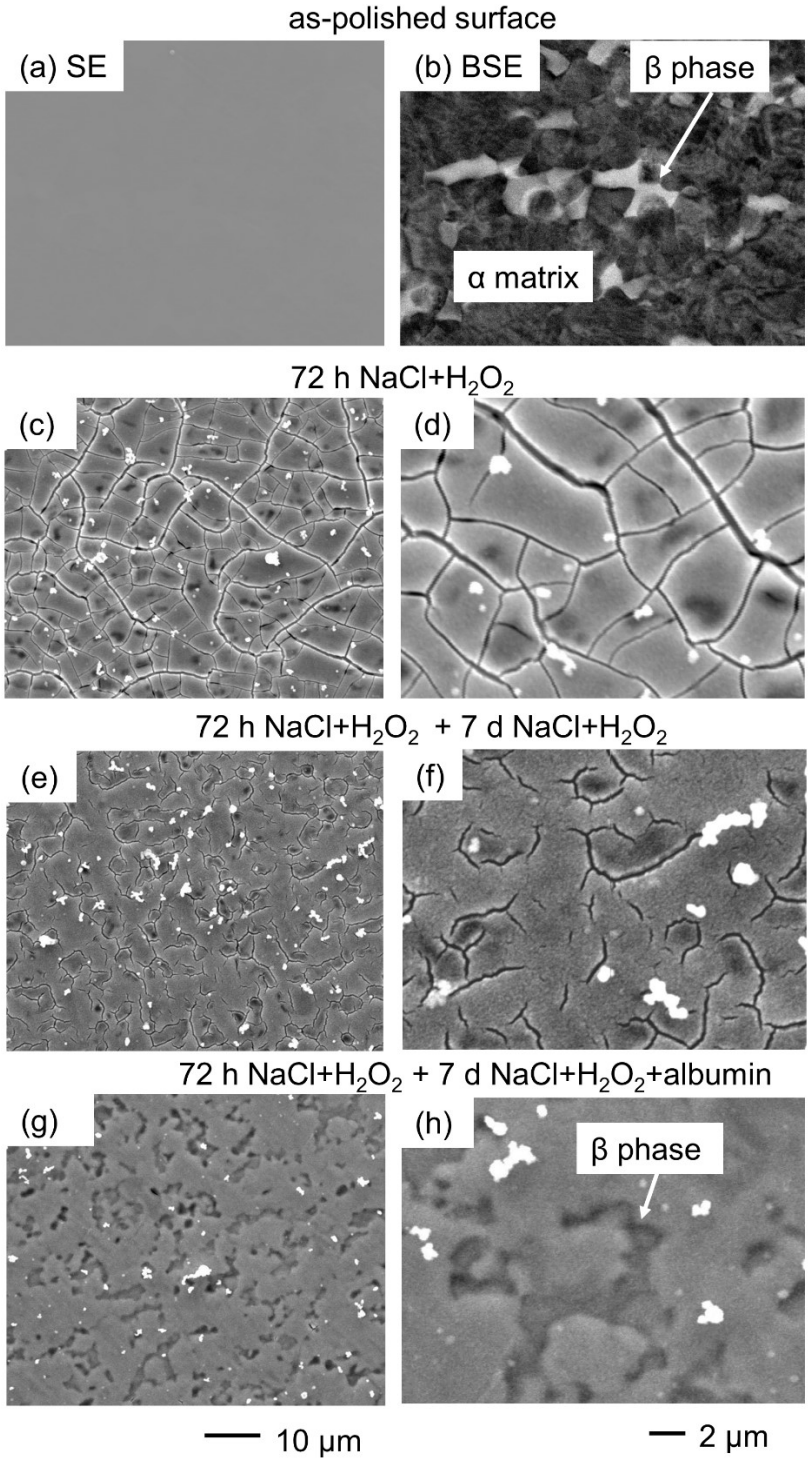

Figure 5-5. SEM images of the surface of Ti-6Al-4V as-polished (a) secondary electron micrograph, SE; and (b) backscattered electron micrograph (BSE). Secondary electron images after immersion in (c) and (d) 0.9% NaCl + 10% H_2O_2 for 72 h at 37 °C; H_2O_2 pre-treated Ti6Al4V samples were then transferred to 0.9% NaCl + 0.1% H_2O_2 solution without (e, f) and with (g, h) presence of 4% albumin for 7 days at 37 °C. The presence of β-phase (identified with EDX, Table 5-1) is indicated.

Table 5-1. A summary of the mean compositions (n=3) with a range of compositions from regions of interests by EDX analysis of the as-polished Ti6Al4V surface (Figure 5-5b) and the surfaces follow incubation in an albumin containing solution (Figure 5-5h).

Elemental% (wt%)		Ti	Al	V	O	Na
as-polished surface (Figure 5-5a)	α phase	91.2 (90.7-91.7)	6.1 (5.7-6.6)	2.5 (2.3-2.8)	0	0
	β phase	86.3 (84.8-88.6)	4.4 (3.9-4.9)	10.0 (8.2-11.3)	0	0
surface after immersion in an albumin containing solution (Figure 5-5h)	white precipitates	71.2 (70.4-72.1)	3.0 (2.9-3.1)	2.1 (1.7-2.6)	22.4 (21.8-23.2)	1.4 (1.3-1.6)
	Oxides (α phase)	81.0 (80.4-82.0)	3.0 (3.0-3.1)	2.9 (2.4-3.7)	12.1 (11.7-12.6)	0
	Oxides (β phase)	82.1 (81.1-82.9)	2.7 (2.4-3.2)	3.0 (2.5-3.5)	11.5 (10.4-12.3)	0

5.3 Time dependent corrosion behaviour at controlled potential

Figure 5-6 shows the current as a function of time for Ti6Al4V, initially immersed in 0.9% NaCl, at a constant potential of 400 mV with additions of 0.9% NaCl containing H_2O_2 or albumin. It can be seen that at an early stage (~1 h, see inset Figure), the current density increased after addition of H_2O_2 containing saline to give a concentration of 0.1% H_2O_2 in 0.9% NaCl. For times up to 20 h, the solution with the additional 4% albumin had a lower current density compared with the control that contained only 0.1% H_2O_2 in 0.9% NaCl.

However, differences became apparent over longer exposure times. In the presence of H_2O_2 alone, the initial increase in current density was found to reach a maximum value of >1 μA/cm^2 at ~1.7 h followed by a steady decay of almost two orders of magnitude, reaching ~0.03 μA/cm^2 at 70 h. This is likely to be a result of the accumulation of surface corrosion products similar to those shown in Figure 5-5(c). However, in the presence of both albumin and H_2O_2, the current density was found to be relatively constant after the initial increase, without considerable degradation. This is consistent with the observation of a much thinner corrosion product layer seen in Figure 5-5(d), and suggests that albumin can promote dissolution of the H_2O_2-induced corrosion product, so that the current reaches a steady state relatively more quickly. A cross-over point in the current densities in these two solutions was observed at ~22 h and subsequently at 70 h, the current density in the presence of albumin and H_2O_2 was measured to be almost an order of magnitude greater than that in H_2O_2 alone.

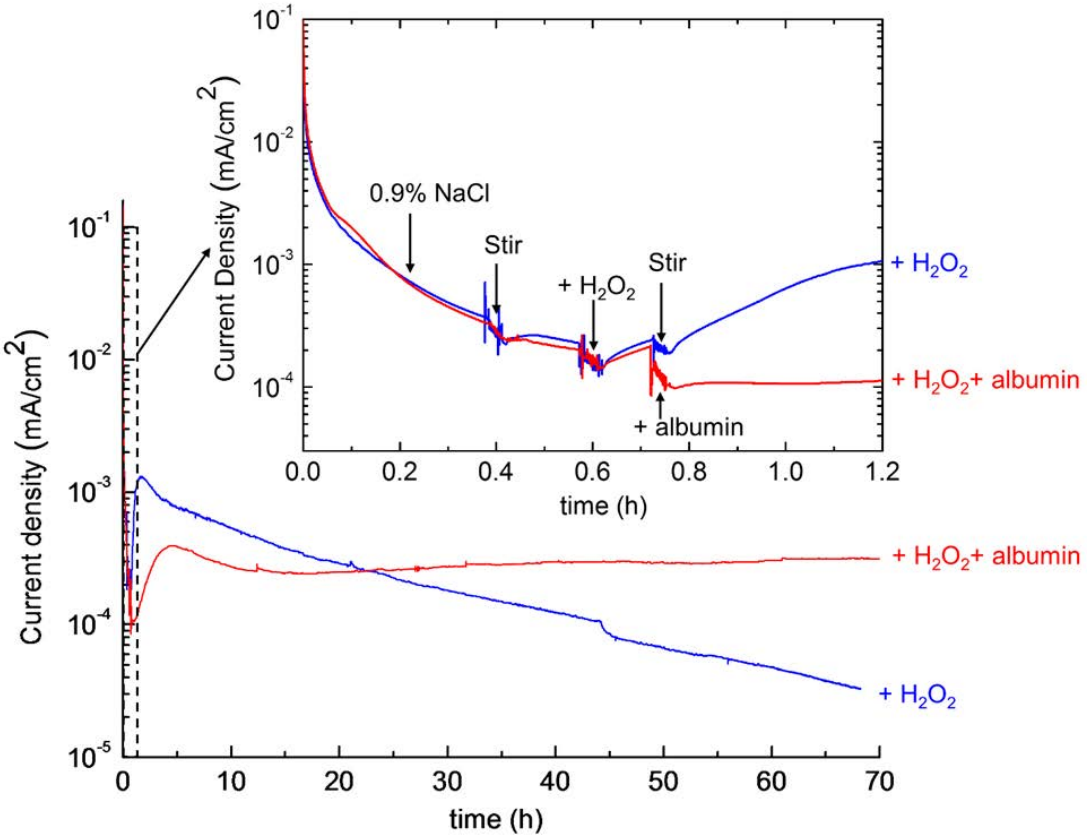

Figure 5-6. Current density as a function of time for Ti6Al4V at a fixed potential of 400 mV (vs. SCE) after 1 h immersion in 0.9% NaCl at OCP and 37°C. The solution was stirred at 0.4 h, then followed by sequential additions of solutions to give a final concentration of 0.1% H_2O_2 and 4% albumin. Addition of solution was also made with the control group to give a final concentration of 0.1% H_2O_2, followed by stirring without addition of albumin. The early stage of the measurement is shown in the inset.

5.4 Metal ion release and EIS measurement at constant potentials

5.4.1 Metal ion release at constant potentials

Yu et al.(17) proposed that the increase in metal release in the presence of both H_2O_2 and albumin compared with H_2O_2 alone might be as a consequence of enhanced corrosion at the lower potentials as a result of inhibition of the cathodic reaction by the presence of albumin. To test this hypothesis, Ti6Al4V was exposed to 0.9% NaCl containing 0.1% H_2O_2 with and without 4% albumin

for 24 h under potentiostatic control. Two potentials were chosen based on the OCP values observed in the two solutions after 24 h in Figure 5-1(b). The OCP value in the presence of 0.1% H_2O_2 alone was close to 300 mV and in the presence of 0.1% H_2O_2 and 4% albumin a value closer to 90 mV was observed. Potential values of 90 mV and 200 mV were chosen so that they could be in the potential range of the active/passive transition as proposed by Yu et al.(17)

Table 5-2 shows that at both measured potentials, Ti ion release was significantly higher in the presence of albumin by almost a factor of 2, indicating that the effect of albumin in dissolving corrosion products dominates the synergistic effect of H_2O_2 and albumin in accelerating Ti ion release. However, in the presence of albumin and H_2O_2, Ti release was significantly higher at 90 mV than that at 200 mV ($p<0.001$), supporting the hypothesis of Yu et al. (17). In the presence of H_2O_2 alone, slightly higher metal Ti ion release was observed at the lower potential, but the difference was much smaller ($p<0.01$).

Table 5-2. The mean concentration and standard deviation of Ti ion release (µg/cm^2) from Ti6Al4V after 1 h at OCP followed by 24 h at either 90 or 200 mV (vs. SCE) in 0.9% NaCl with 0.1% H_2O_2 or 0.1% H_2O_2 + 4% albumin at 37 °C. Four measurements were made for each condition.

Ti ion release (µg/cm^2)	90 mV	200 mV
0.9% NaCl + 0.1% H_2O_2	0.30 $\pm$ 0.01	0.28 $\pm$ 0.01
0.9% NaCl + 0.1% H_2O_2 + 4% albumin	0.57 $\pm$ 0.01	0.51 $\pm$ 0.01

5.4.2 Potentiostatic EIS

The metal/oxide/solution interface in 0.9% NaCl with presence of both H_2O_2 and albumin was also characterised by EIS measurements following potentiostatic polarisation for 20 h to develop a stable passive film. Figure 5-7 shows Bode and Nyquist plot of Ti6Al4V at different polarising potentials. It was observed that with potentials varying from 40 mV to 200 mV, phase angles in the Bode plot were shown to be very similar and impedance modulus (|Z|, Figure 5-7(a)), which reached plateaus at low frequency range (10^{-2} to 10^{-3} Hz), increased with increasing potentials. Similarly in Nyquist plot (Figure 5-7(b), the real part of impedance increased with increasing potentials. The polarisation resistance, oxide resistance and capacitance were obtained by fitting the EIS spectra with a two-time constant equivalent circuit (Figure 3-3) and are shown in Figure 5-8 as a function of potential. Figure 5-8(a) shows the polarisation resistance increased steadily with potential from ~360 kΩ-cm^2 at 40 mV to ~930 kΩ-cm^2 at 200 mV. Figure 5-8(b) shows the oxide resistance (R_{hf}) and capacitance (calculated from Y_{hf} using Equation 3-1 as a function of potential. The oxide resistance showed little change from 40 to 90 mV then increased significantly with potential up to 200 mV. The oxide capacitance showed some variation with potential, but appeared to give a maximum value at 90 mV.

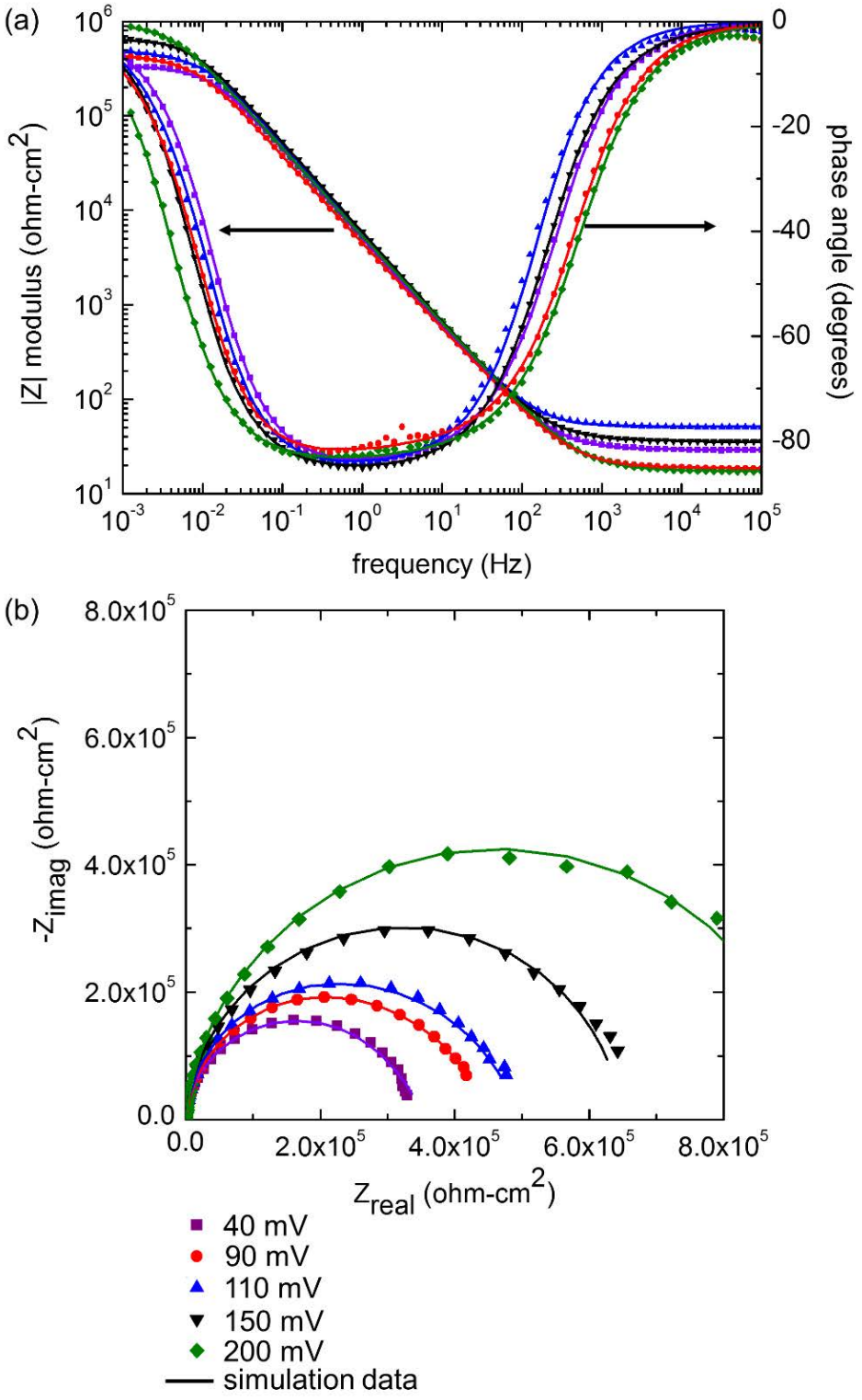

Figure 5-7. Bode and (b) Nyquist plots of Ti6Al4V at polarised potentials from 40 mV, 90 mV, 110 mV, 150 mV up to 200 mV, which were kept statically for 20 h after 1 h immersion at OCP in 0.9% NaCl + 0.1% H_2O_2 + 4% albumin at 37 °C. Symbols are experimental data and lines are simulated data using the equivalent circuit shown in Figure 3-3.

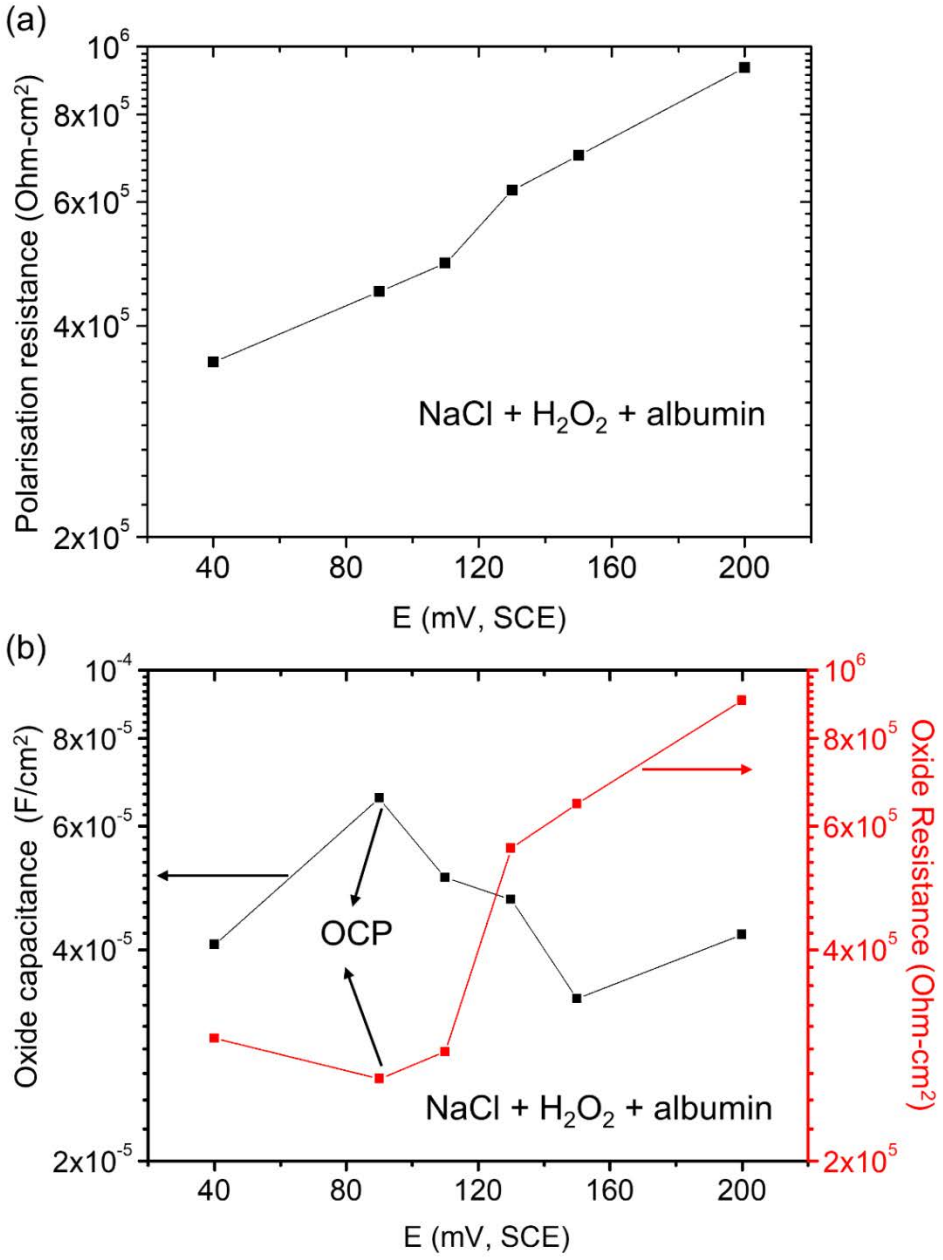

Figure 5-8. (a) Polarisation resistance and (b) Oxide resistance and capacitance of Ti6Al4V as a function of polarised potential in 0.9% NaCl + 0.1% H_2O_2 + 4% albumin at 37 °C. Error bars are not shown because the data is a single experiment. All parameters were obtained by fitting the impedance spectroscopy shown in Figure 5-7 to the equivalent circuit shown in Figure 3-3.

5.5 Discussion

5.5.1 Effect of exposure time on corrosion of Ti6Al4V in the presence of H_2O_2 with and without addition of albumin

It can be seen from potentiodynamic polarisation (Figure 5-2) that addition of H_2O_2 increased the passive current density of Ti6Al4V in 0.9% NaCl. Similarly, the potentiostatic current density (Figure 5-6) increased after addition of H_2O_2 in 0.9% NaCl. H_2O_2 is known to increase the corrosion rate of Ti (22) and its alloys (18) via a complexation reaction with Ti ions (16, 19-21).

At short time exposures (t < ~22 h), addition of 4% albumin suppressed the current density in the presence of H_2O_2 (Figure 5-6). Rapid adsorption of albumin onto the Ti6Al4V oxide surfaces has previously been observed with Quartz Crystal Microbalance (QCM) and X-ray photoelectron spectroscopy (XPS) (89, 154). In addition, using ^{125}I radio labelling, it has been shown that albumin adsorbs on oxidised Ti surfaces from the early stages of immersion with most of the adsorption taking place within the first few minutes (91). To date, most studies have reported that albumin inhibits corrosion of commercially pure (CP) Ti and Ti alloys (94, 95, 99) and also protects it from dissolution induced by e.g. fluoride ions (155). Adsorption of albumin films have been proposed to block dissolution. However, all of these experiments have taken place over short time periods, typically over no more than a few hours.

After longer term exposures (up to 72 h), it can be seen from Figure 5-6 that the potentiostatic current density in the presence of H_2O_2 alone decreased significantly after the initial increase, most likely as a result of blocking of the

surface by the peroxide corrosion product layer shown in Figure 5-5 (c) and (d). It has been proposed that Ti oxide film forms a two-layer structure in phosphate buffered saline, which consists of a thin barrier type inner layer and thick porous type outer layer, and the presence of H_2O_2 reduces corrosion resistance and thickens the outer porous layer (19-21).

In contrast, prolonged exposure in the presence of both H_2O_2 and albumin resulted in a higher current density than that in the presence H_2O_2 alone, with a cross-over point at ~22 h. This is consistent with the observation of a much thinner corrosion product layer in Figure 5-5(g) and (h), suggesting that albumin promotes dissolution of the peroxide corrosion product layer at longer time periods.

The interaction between albumin and peroxide corrosion layer has been studied by Sousa et al. via a kinetic perspective of albumin adsorption, adhesion and exchangeability (desorption) (89). It was found that the more hydrophilic surface of TiO_2 after H_2O_2 immersion adsorbed less albumin but with higher work of adhesion i.e. it was more strongly attached on the surface, compared with that of the more hydrophobic surface of sputtered TiO_2 (89). After the adsorption step, it was suggested that the exchangeability of albumin was changing with time: after 24 h the adsorbed albumin molecules on the H_2O_2-treated TiO_2 surface seem to be less exchangeable than those adsorbed on the sputtered TiO_2 surface; however after 72 h nearly all the adsorbed albumin molecules effectively exchanged with other albumin molecules, which suggested that longer time is needed for exchange of albumin molecules adsorbed on surface

of H_2O_2-TiO_2 complexes (89). Therefore, the time dependent dissolution behaviour observed in the presence work is consistent with the desorption of albumin-metal complexes as it is a slow, rate determining process (89), and can result in thinner oxides.

The time-dependent data were confirmed by the EIS data shown in Figure 5-4. The polarisation resistance (R_p) of Ti6Al4V in in the presence of H_2O_2, R_p was significantly lower than that in NaCl alone after 24 h and both increased gradually with time, consistent with the formation of a thicker corrosion product layer. At 120 h, R_p in presence of H_2O_2 was over an order of magnitude lower than that in NaCl alone. Comparable values were measured for CP Ti in PBS where R_p decreased from 2×10^7 ohm-cm^2 to 8×10^5 ohm-cm^2 in the presence of 50 mM H_2O_2 (compared with 33mM in the present work) after 125 h (87). The decreased corrosion rate of Ti6Al4V in the presence of H_2O_2 over time has been attributed to growth of a corrosion product layer.

In the presence of albumin and H_2O_2, R_p showed little change over time compared with the behaviour in H_2O_2 alone, consistent with the steady potentiostatic current shown in Figure 5-6. Moreover, it can be seen from Figure 5-4 that after 120 h, R_p in presence of H_2O_2 and albumin was significantly lower than that of H_2O_2 alone, consistent with the presence of a thinner corrosion product layer and increased dissolution. This observation correlates well with previous ICP-MS measurements carried out by Yu et al. (17), where metal ion release was measured in identical solutions after 2-week incubation and the combination of H_2O_2 and albumin was found to give a much higher Ti release

than that of H_2O_2 alone. It suggests that the explanation for this observation is likely to be the increased dissolution of the peroxide corrosion product in the presence of albumin.

A possible mechanism is proposed and shown schematically in Figure 5-9 to illustrate how the synergistic action of H_2O_2 and albumin exacerbates corrosion as a function of time. A thin, uniform metal oxide/hydroxide is formed on the metal substrate following immersion in a 0.9% NaCl electrolyte, Figure 5-9(a). In the presence of H_2O_2 (Figure 5-9(b)), the metal substrate (and its oxides) complex with H_2O_2 resulting in an increased corrosion rate and formation of a thicker, rougher and more porous corrosion product layer. The peroxide corrosion products block the surface and reduce further corrosion. In the presence of albumin (Figure 5-9(c)), the biomolecule adsorbs onto the metal/oxide surface, binds the metal ions, forms soluble metal protein complexes and subsequently desorbs from the surface. The process is time-dependent process and manifests the dissolution behaviour. As a result, the peroxide corrosion products are dissolved by albumin and a thinner corrosion product layer is formed (Figure 5-9(d)), which facilitates further corrosion.

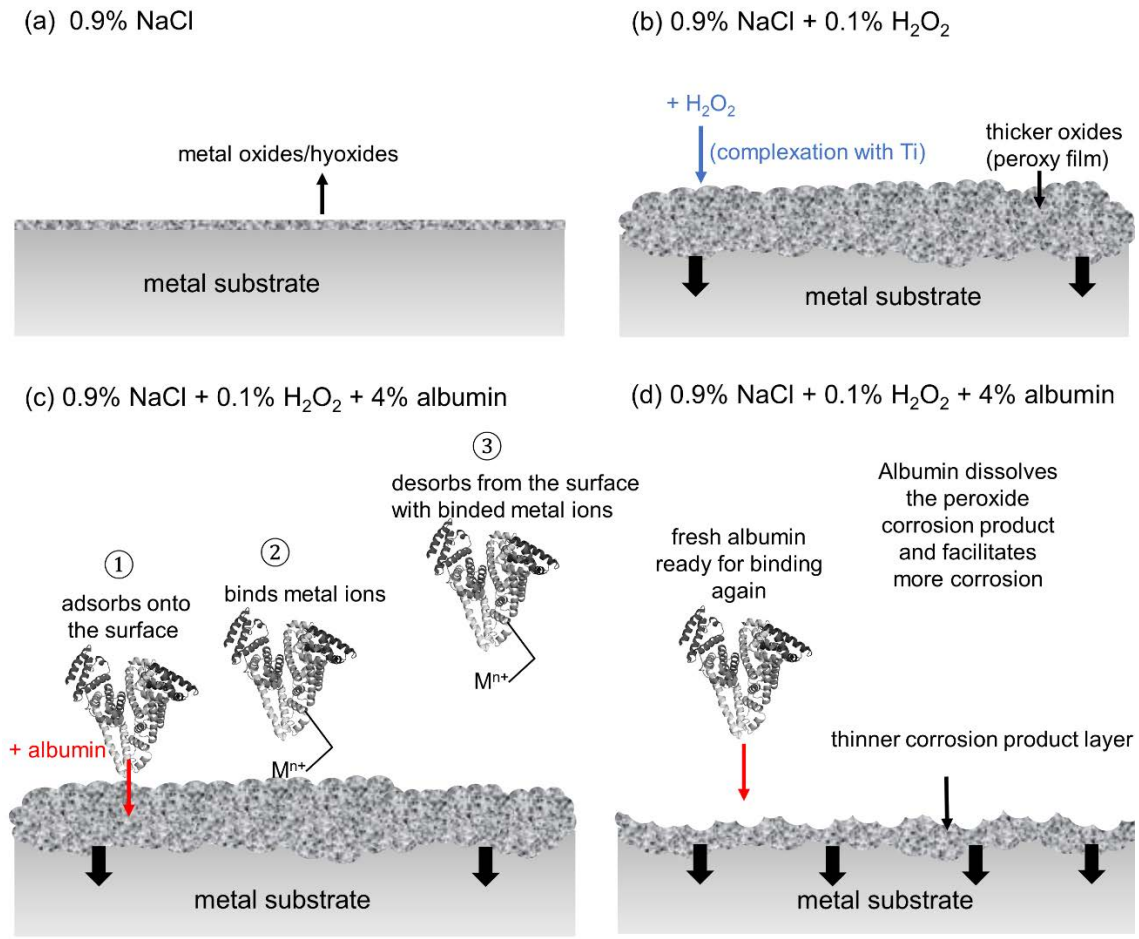

Figure 5-9. Possible mechanism of the synergistic action of H_2O_2 and albumin on corrosion of Ti6Al4V. (a) formation of a thin metal oxides/hydroxides film in 0.9% NaCl; (b) the presence of H_2O_2 results in an increased corrosion and a thicker corrosion product layer; (c) the presence of albumin adsorbs onto the peroxide corrosion product layer, binds metal ions, and subsequently desorbs from the surface; (d) a thinner corrosion product layer is formed and facilitates more corrosion. Fresh albumin molecules are ready to the cycle of adsorbing-binding-desorbing again.

5.5.2 Effect of potential on dissolution and oxide film formation on Ti6Al4V in presence of albumin and H_2O_2

In the work of Yu et al., short term electrochemistry tests (t ~ 1 h) and long term (2 weeks) ion release measurements showed contradictory results regarding the effect of albumin on dissolution of Ti6Al4V in the presence of H_2O_2 in physiological saline. The investigation explained the observation using a mixed

potential theory (Figure 5-10a), suggesting that albumin suppresses the cathodic reaction, decreasing the corrosion potential into a more “active” region for dissolution of Ti at lower potential (17). In the present work, this hypothesis was tested by measuring metal ion release from Ti6Al4V at constant applied potentials. Table 5-2 shows that in the presence of albumin and H_2O_2, the rate of Ti ion release was higher at lower potentials, consistent with the proposed “active dissolution” effect (17). However, it is clear that the increased metal ion release at both potentials is substantially greater in the presence of albumin, indicating that the synergistic effect of albumin and peroxide observed at longer exposure times is dominated by the role of albumin in dissolving the peroxide corrosion product. A new mixed potential theory was proposed (Figure 5-10b) taking into account the time dependence effects as observed in this study.

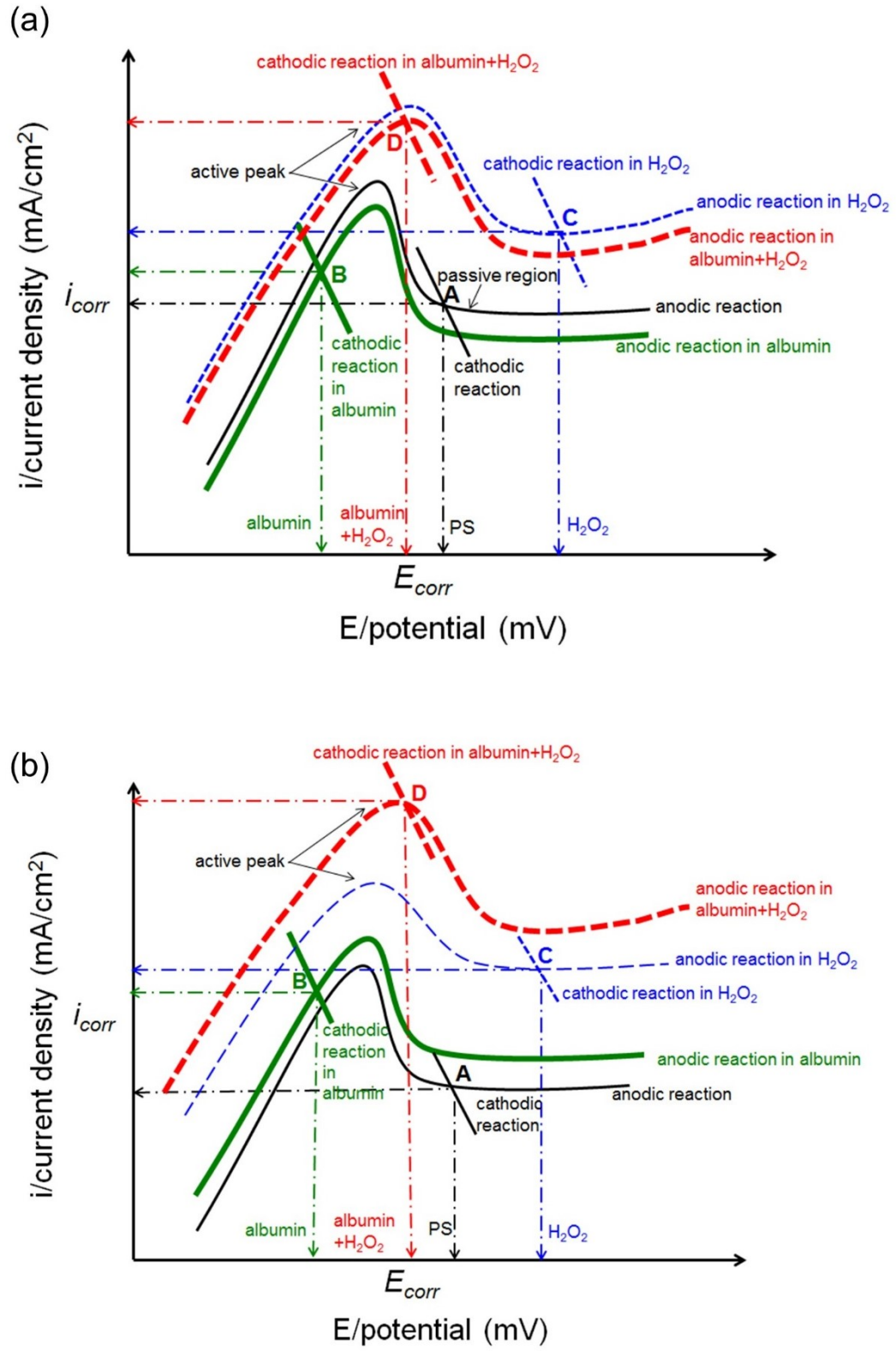

Figure 5-10. Proposed mixed potential theories by (a) Yu et al. to explain the synergistic effect of albumin and H_2O_2 on increased corrosion of Ti6Al4V (17) and (b) based on the mass spectroscopy results in this study.

Metal implants are exposed to an environment that is more complex than the physiological saline (0.9% NaCl) that is used in standard tests such as ASTM F1801-97 and ASTM F1875-98 (133, 134). In the present work on Ti6Al4V, the major protein in the body, albumin, is shown to interact with the corrosion products of Ti in the presence of H_2O_2, which is produced in inflammatory processes. The level of H_2O_2 used in this work (0.1% = 33 mM) is at the lower end of those used in previous *in vitro* corrosion studies (17-21, 23). Concentrations of H_2O_2 measured in extracellular environments are frequently reported to be in the µM range (13, 24, 25, 83, 85). However, both immune cells and microbial biofilms (such as those found on oral implants) create local micro-environments where H_2O_2 can be considerably concentrated reaching mM concentrations. For example, measurements of H_2O_2 concentration in surface biofilms of the oral microbe *Streptococcus gordinni* have been shown to increase with proximity to the biofilm with quasi-steady-state concentrations of 1.4 mM measured at 100 µm from the exposed microbial surface (85). It was proposed that the concentration of H_2O_2 may reach much higher levels within the biofilm itself and at the biofilm substrate interface.

This work also highlights the need to examine the time-dependence of corrosion behaviour of metals used for biomedical implants, since in this case there is a clear switch in the observed behaviour at ~1 day. Similar time-dependent corrosion behaviour in the presence of albumin was also found in biodegradable Mg alloys in simulated body fluid (135). It was found that albumin blocks dissolution in the first few hours of exposure, but increased corrosion was observed over longer exposures (135).

As biomolecules such as albumin and H_2O_2 are present in inflamed peri-implant tissue, these observations raise the question of whether standard testing should be complemented by testing in more realistic environments over more realistic time periods.

5.6 Conclusions

Albumin was found to have a time dependent effect on dissolution of Ti6Al4V in the presence of H_2O_2 in 0.15 M NaCl.

At short times (t < ~22 h), albumin supressed dissolution rates, but at longer times, the rate of dissolution increased to values greater than those found in absence of albumin.

The long-term dissolution behaviour in the presence of albumin and H_2O_2 can be attributed to the enhanced dissolution of peroxide corrosion products in the presence of albumin, resulting in formation of a thinner oxide layer on the metal surface.

The rate of metal ion release in the presence of albumin and H_2O_2 was found to depend on potential. At lower potential, a higher metal ion release rate was observed via ICP-MS measurements, and the oxide resistance and capacitance determined from EIS was consistent with a thinner oxide layer than that found at higher potentials.

The corrosion rate of Ti6Al4V in the presence of albumin and H_2O_2 in 0.15 M NaCl was observed to be significantly higher than that in 0.15 M NaCl alone, emphasising the need to test alloys for biomedical implants in more realistic physiological solutions. It is also essential to make measurements over longer time periods than those typically performed in standard tests involving conventional polarisation curves.

6 IN SITU CHARACTERISATION OF CORROSION PRODUCTS IN ZR ARTIFICIAL PIT AND BULK ZR ELECTROCHEMISTRY IN SIMULATED PHYSIOLOGICAL SOLUTIONS

6.1 Introduction

The aim of the work described in this chapter is to characterise the localised corrosion of Zr. The structure and speciation of Zr corrosion products formed in 'artificial pits' (139, 141), were measured in-situ using synchrotron X-ray diffraction (XRD) and X-ray absorption spectroscopy (XAS) for the first time. The Zr corrosion products were formed by growing a Zr 'artificial pit' which was controlled at a constant potential in simulated physiological electrolytes. Measurements were conducted in 0.9% NaCl with and without the addition of H_2O_2, which is a biomolecule produced during inflammation, or albumin, which is the most prevalent protein in tissue fluids, or their combination. The rationale behind this work is to provide a better understanding of the pit chemistry of Zr, which is known for its vulnerability to pitting. In addition, we aimed to identify how the nature of corrosion products, are dictated by electrolyte compositions representative of physiological solutions that can be encountered in the peri-implant environment.

Complementary characterisations of dissolved Zr surfaces from established Zr 'artificial pits' were carried out using scanning electron microscopy (SEM). The morphology and size information of Zr corrosion products formed, were further characterised using transmission electron microscopy (TEM).

Complementary electrochemistry studies, including anodic polarisation were also carried out on bulk Zr surfaces in 0.9% NaCl with and without addition of H_2O_2 and/or albumin. Pits formed following anodic breakdown were characterised by SEM and optical microscopy.

6.2 Electrochemistry of Zr artificial pits

Figure 6-1 shows the current densities and growth rates of Zr artificial pits at 0.8 V (Ag/AgCl) in solutions containing 0.9% NaCl, with and without additions of H_2O_2, or albumin, or their combinations. It was observed that at 0.8 V the current quickly reaches a peak value and decreases due to the precipitation of a salt layer from the supersaturated solution. Subsequently the current density levels out to a limiting current density at approximately 0.4 A/cm^2. Figure 6-1b shows the pit growth rate (pit depth as a function of time) at 0.8 V, where the pit depth estimated by Faraday's Law (integration of current) was cross checked with visual observations. It was demonstrated that pit depth obtained from Faraday's Law (integration of current) was consistent and seen to be slightly lower than the one measured optically, suggesting the as-measured current is mostly attributed to material loss, with possibly minor contributions from cathodic reactions. It can be seen that both the current densities and the pit growth rates were very similar in 0.9% NaCl solutions, with and without addition of H_2O_2 and/or albumin.

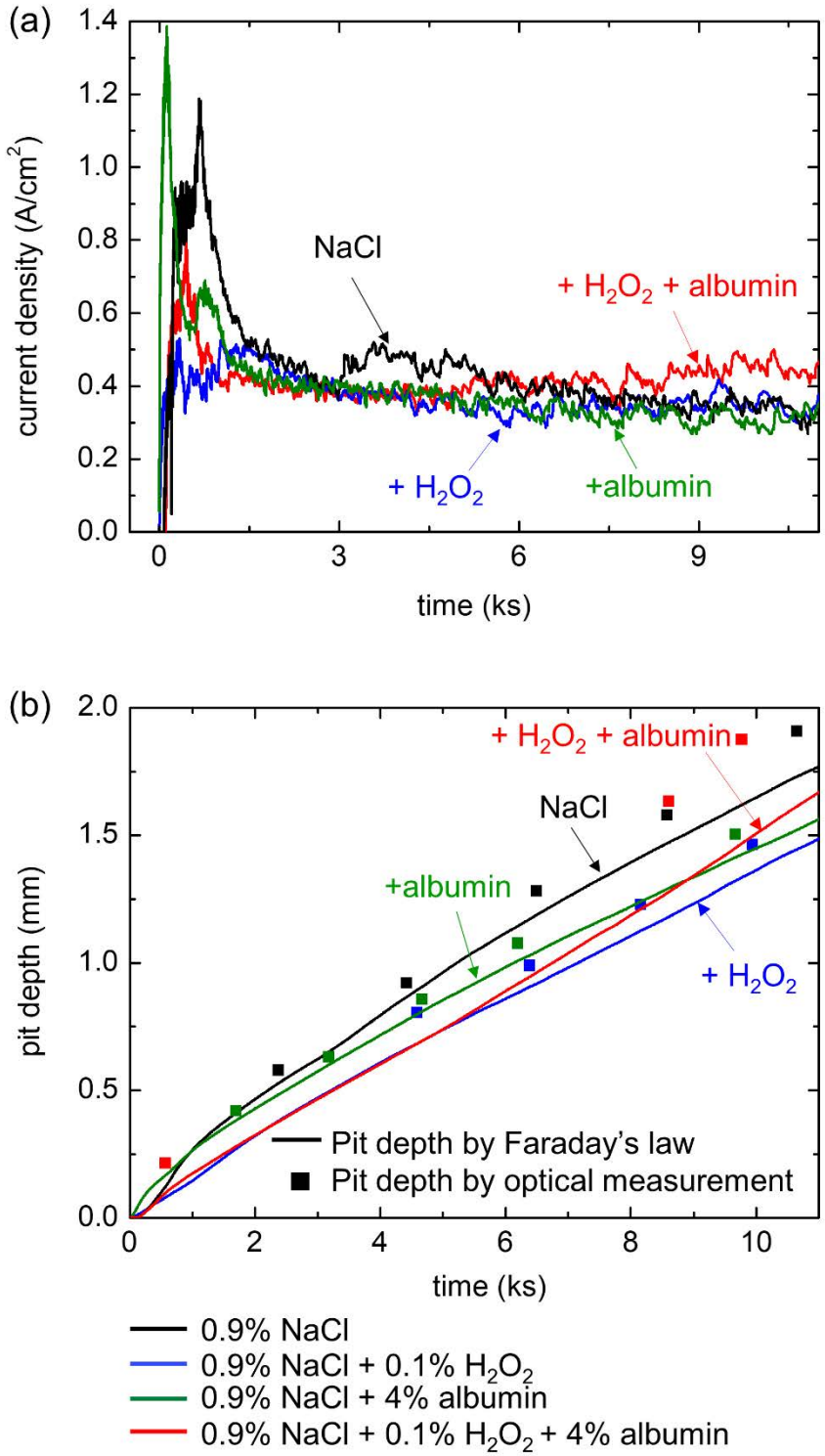

Figure 6-1. (a) current densities of Zr artificial pits at 0.8 V (vs. Ag/AgCl) in 0.9% NaCl, with and without additions of 0.1% H_2O_2, or 4% albumin, or their combinations; (b) pit depth as a function of time during growth in solutions of 0.9% NaCl, with and without additions of 0.1% H_2O_2, or 4% albumin, or their combinations. Solid lines refer to pit depth estimated by current integrations. Square scatter plot data points refer to the depth measured from optical imaging.

6.3 Structure of Zr corrosion products formed in-situ

Figure 6-2 shows an optical image of a ~3 mm deep Zr artificial pit that was grown at 0.8 V (Ag/AgCl) in physiological saline (0.9% NaCl) solution with addition of 0.1% H_2O_2 and 4% albumin. The location of XRD measurements relative to the position of the Zr foil (0 mm) are noted. Diffraction patterns are shown as a stack plot in Figure 6-2(b), and their positions are referenced to the locations marked in Figure 6-2(a). The diffraction pattern of Zr foil at 0 mm (Figure 6-2b) was consistent with a Zr powder standard (156) but with different relative heights of peaks due to the anisotropy of the foil. At 0.4 mm, where it was apparent a crevice had formed between the foil and the embedding epoxy (Figure 6-2a), the diffraction pattern shows the presence of Zr metal (foil) and zirconyl chloride octahydrate ($ZrOCl_2 \cdot 8H_2O$) (157). From 0.5 to 0.7 mm, more intense diffraction peaks consistent with the $ZrOCl_2 \cdot 8H_2O$ standard were observed. From 0.8 to 2.3 mm which corresponds to black corrosion products seen in the optical image, Figure 6-2a, the diffraction peaks are weaker, but the major diffraction peaks (intensity 20x) are consistent with a Zr powder standard (156) and three broad peaks indicated with asterisks are consistent with three major peaks of the tetragonal ZrO_2 standard (158). At 3.1 and 3.8 mm, corresponding to electrolyte inside and outside of the pit cavity (Figure 6-2a), the diffraction peaks (intensity 200x) are shown to be consistent with that of the Zr powder standard (156).

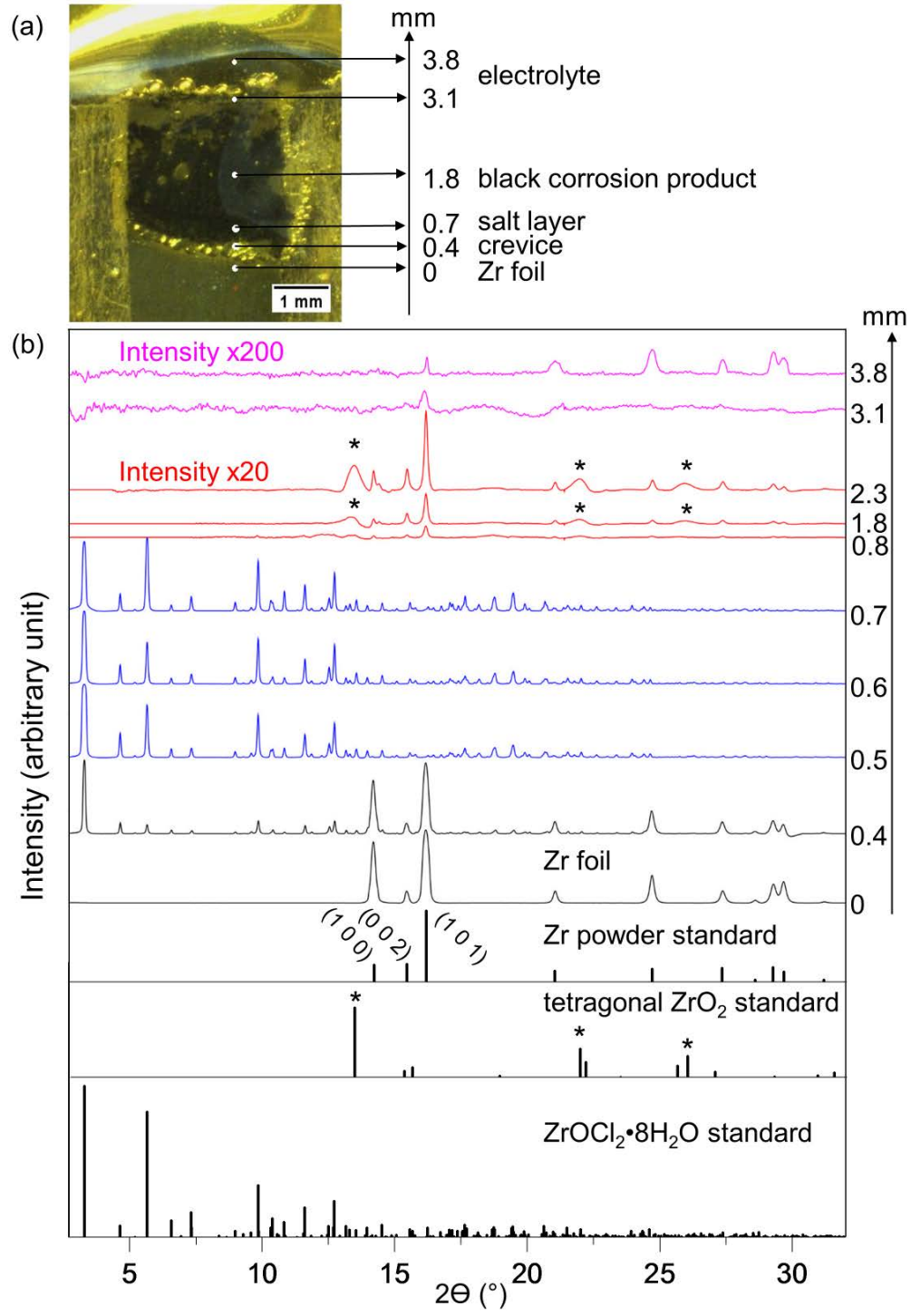

Figure 6-2. (a) Optical image of a Zr artificial pit at 0.8 V (Ag/AgCl) in 0.9% NaCl + 4% albumin + 0.1% H_2O_2 solution at ambient temperature. The height of XRD measurements above the dissolving interface are marked; (b) stack plot of selected diffraction patterns in a sequence from solution to metal. Intensities of diffraction patterns at 3.8 and 3.1 mm were multiplied by 200x and intensities of diffraction patterns at 2.3, 1.8, 0.8 mm in black corrosion products were multiplied by 20x. Standards for Zr powder (156), tetragonal ZrO_2 (158) and $ZrOCl_2 \cdot 8H_2O$ (157) are indicated. *peaks that correlate with ZrO_2.

6.4 Structure of black corrosion products further away from the corrosion front

Figure 6-3a shows an optical image of a Zr artificial pit at 0.8 V (Ag/AgCl) in 0.9% NaCl. It can be seen that black corrosion products accumulated at the left-hand side ‘bulge’ of the pit cavity. The ‘bulge’ feature enabled measurements to be made of corrosion products that were not located at the position of the original Zr foil. Figure 6-3b shows a stack plot of selected, normalised diffraction patterns at 2.2 mm, 1.8 mm, and an average of all patterns from 0 to 3 mm. It was found that the location of all major peaks from the selected patterns were consistent with the Zr powder standard (156). Furthermore, the relative heights of the peaks from the corrosion products were more consistent with the Zr powder standard than the anisotropic foil, suggesting that the corrosion products are randomly-oriented Zr metal fragments. In addition to sharp Zr metal peaks, fainter broad peaks were consistently observed (marked with asterisks), and from the averaged diffraction pattern (Figure 6-3c), it was found that the peaks were consistent with the tetragonal ZrO_2 standard (158).

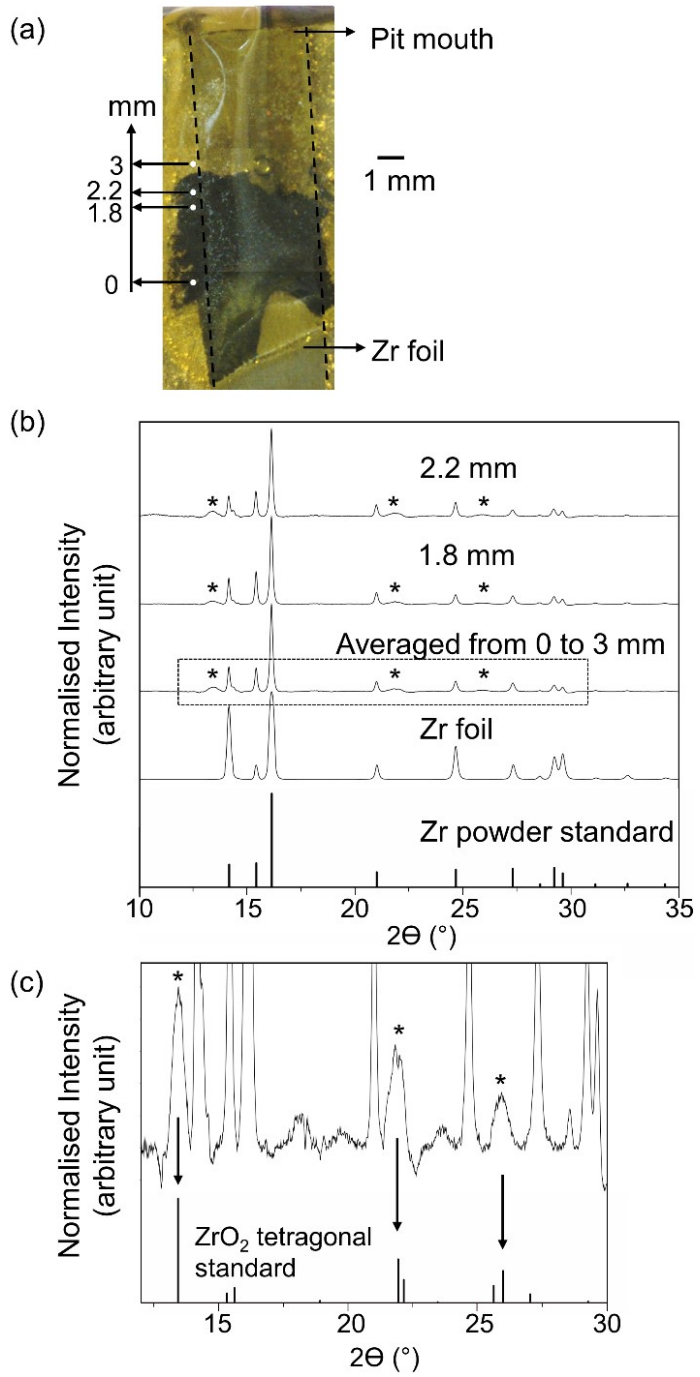

Figure 6-3. (a) Optical image of a Zr artificial pit at 0.8 V (Ag/AgCl) in 0.9% NaCl at ambient temperature. The location of selected diffraction patterns from a XRD scan with 100 µm step-size are shown at the left-hand side 'bulge' of the artificial pit are shown (mm) relative to 0 mm indicated at the bottom; (b) diffraction patterns at 2.2 mm and 1.8 mm (locations marked in (a)), the average of all patterns from 0 mm to 3 mm, and the Zr foil. Intensities were normalised to the maximum Zr peak. Peaks marked with asterisks are shown in detail in (c) with intensity normalised to the maximum ZrO_2 peak. The Zr powder standard (156) and tetragonal ZrO_2 standard (158) are indicated at the bottom of (b), and (c), respectively.

Figure 6-4a shows the diffraction pattern of the Zr foil with clear anisotropy in the (0 0 2), (1 0 0) and (1 0 1) reflections highlighted. Figure 6-4(b), (c) and (d), show diffraction patterns of the Zr fragments found in the black corrosion products. Figure 6-4(b) and (c) show less anisotropy and a different preferential orientation of crystals, suggesting that fragments may have rotated they became detached. The average of the diffraction patterns from 0 mm to 3 mm (Figure 6-4d) shows isotropic scattering with continuous and smooth diffraction rings at all planes, suggesting many fine randomly oriented crystallites.

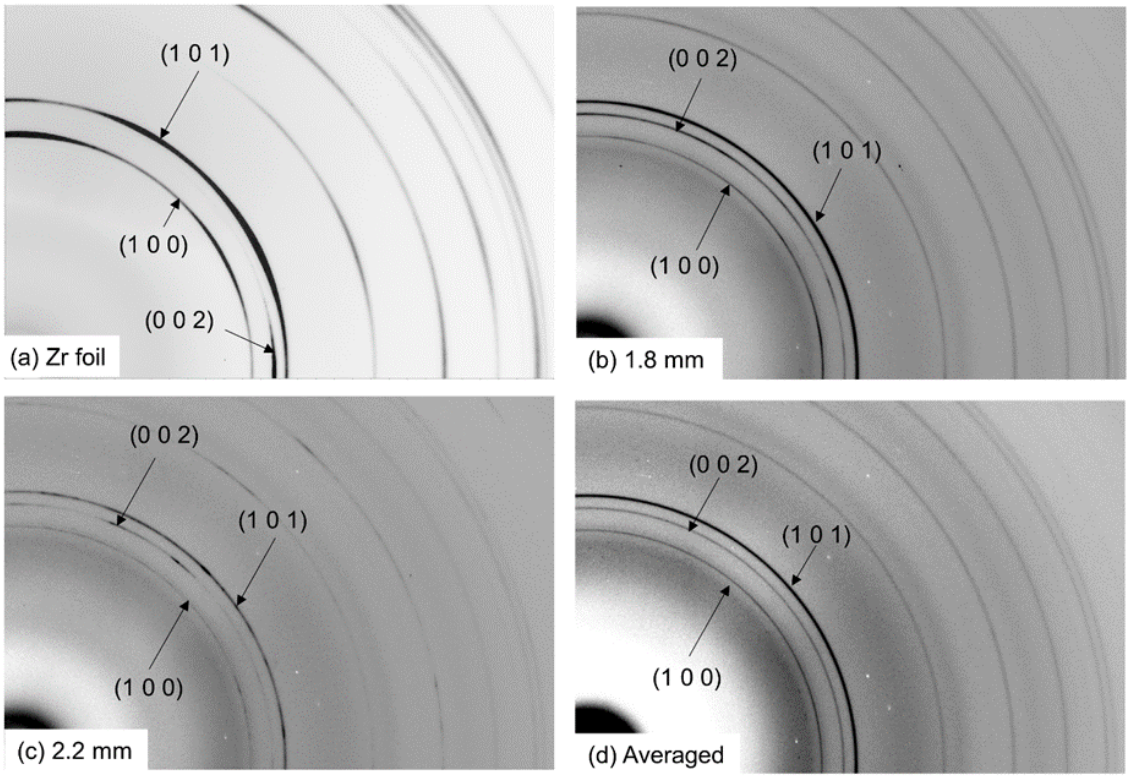

Figure 6-4. Diffraction pattern images at positions as shown in Figure 6-3. Image (b), (c) and (d) are shown with brightness and contrast adjusted for clarity.

6.5 Structure of the salt layer adjacent to the corrosion front

Figure 6-5a shows an optical image of a Zr artificial pit with magnified views of the salt layer for the sample containing 0.9% NaCl + 0.1% H_2O_2. The dissolving interface is not flat: there appears to have been some crevice corrosion. The point marked 0 µm is the highest point that appears to have no crevice corrosion (the diffraction pattern, shown in Figure 6-6, gives diffraction peaks from the foil). At 100 µm, there are strong diffraction rings from the foil (indicated with upward arrows) showing characteristic anisotropy (Figure 6-5b), but also a few rings that are characteristic of $ZrOCl_2 \cdot 8H_2O$ (Figure 6-6 and Figure 6-5b indicated with diagonal arrows). The presence of rings from both the Zr foil and $ZrOCl_2 \cdot 8H_2O$ indicate that there is crevice corrosion down the interface between the epoxy and the foil. At 130 µm (Figure 6-5c), more intense and smooth diffraction rings of $ZrOCl_2 \cdot 8H_2O$ were observed. At 570 µm (Figure 6-5d), further away from the interface, $ZrOCl_2 \cdot 8H_2O$ was also observed, but diffraction rings were found to be spotty indicating coarsening of the salt crystals. At 680 µm (Figure 6-5e), even further away from the interface and close to the black corrosion products, the diffraction pattern exhibited discrete speckles consistent with coarse crystals of $ZrOCl_2 \cdot 8H_2O$ and faint diffraction rings from Zr metal indicating the presence of Zr fragments, which was consistent for all solutions studied.$ZrOCl_2 \cdot 8H_2O$ was consistently observed from the dissolving surface to a distance of approximately 500 µm to 600 µm away from the interface with gradual coarsening of the salt crystals further into the solution.

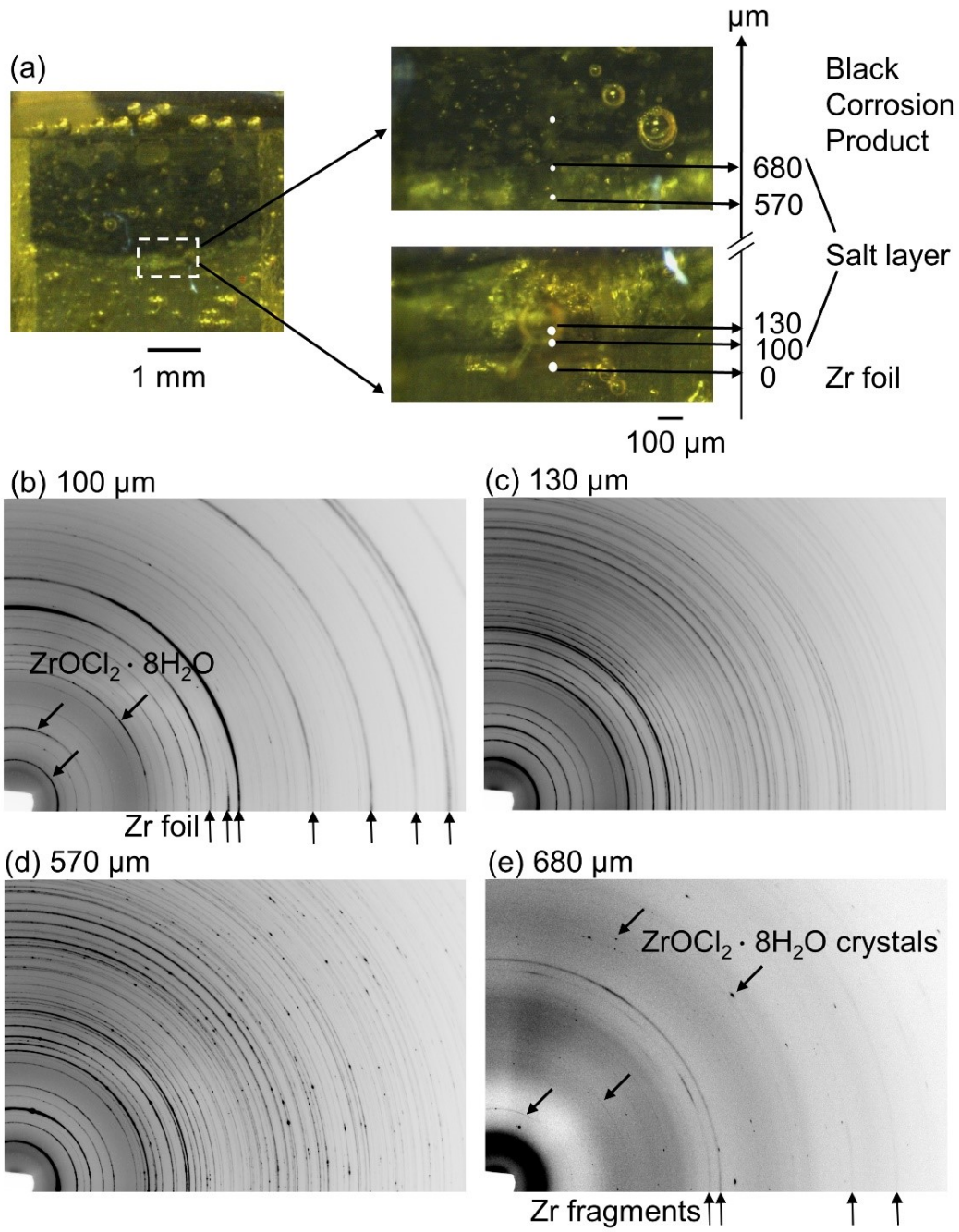

Figure 6-5. (a) An optical image of a Zr artificial pit formed at 0.8 V (Ag/AgCl) in 0.9% NaCl + 0.1% H_2O_2 at ambient temperature. (b)-(e) Diffraction patterns from a 10 μm step line scan in a sequence from the black corrosion products through the salt layer and into the metal. The positions of the selected patterns are referenced in μm relative to the top of the uncorroded Zr foil (0 mm). Arrows shown diagonally indicate diffraction rings from $ZrOCl_2 \cdot 8H_2O$ phase; arrows shown upwards indicate diffraction from Zr metal. Diffraction images at (b) 100 μm; (c) 130 μm; (d) 570 μm and (e) 680 μm are shown with adjusted brightness and contrast.

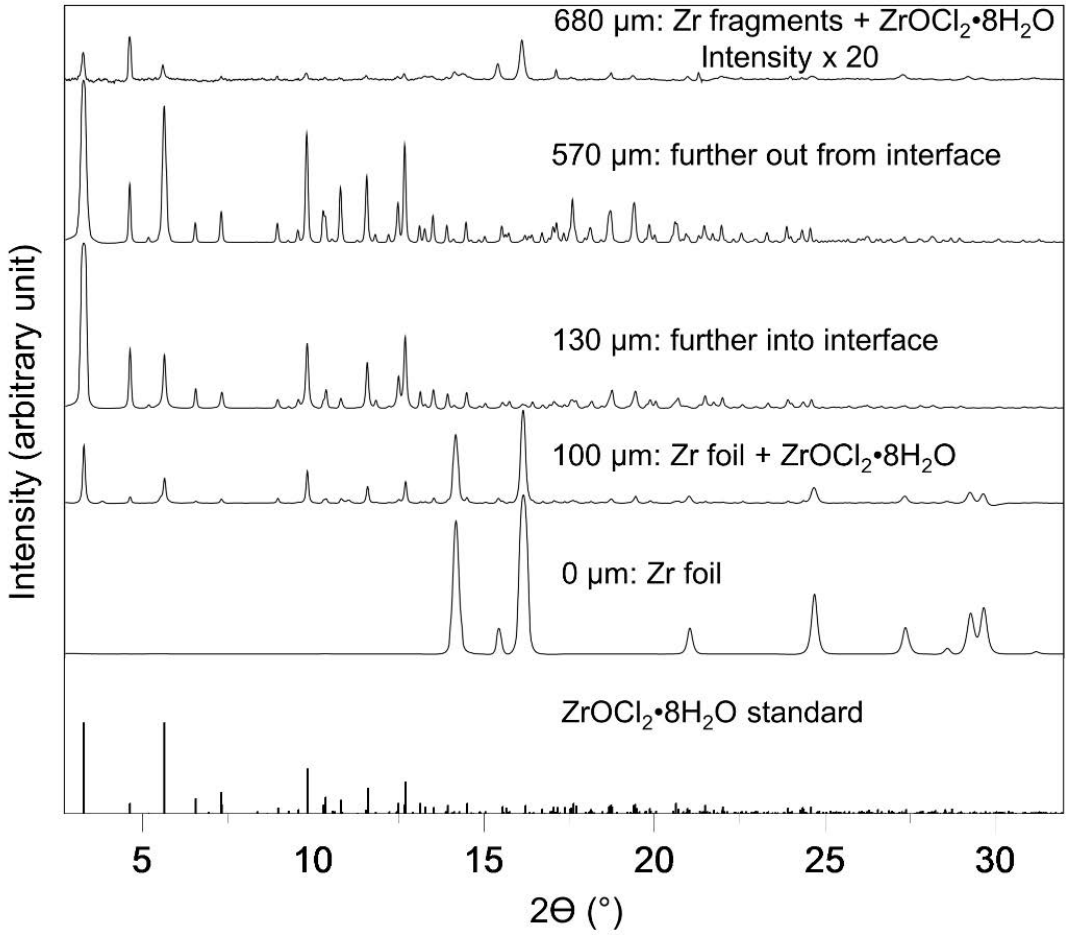

Figure 6-6. A stack plot of integrated diffraction patterns as shown in Figure 6-5. Diffraction patterns of Zr foil and $ZrOCl_2 \cdot 8H_2O$ are shown at the bottom for reference.

6.6 Comparison of corrosion species in the simulated physiological solutions

Figure 6-7 demonstrates the averaged diffraction patterns of the black corrosion products distant from the corrosion front (Figure 6-7a), and of the salt layer close to the corrosion front (Figure 6-7b) in the various electrolytes. It was observed that the averaged patterns of the black corrosion products in the different solutions presented the same phase constitution of Zr metal (powder) and tetragonal ZrO_2 (marked with asterisks) (Figure 6-7a). It was also observed that the averaged diffraction patterns from the salt layer in the different solutions

exhibited the same diffraction pattern of $ZrOCl_2 \cdot 8H_2O$ (Figure 6-7b). It can be concluded that the presence of H_2O_2 and/or albumin did not affect the formation of corrosion species in Zr artificial pits in terms of speciation.

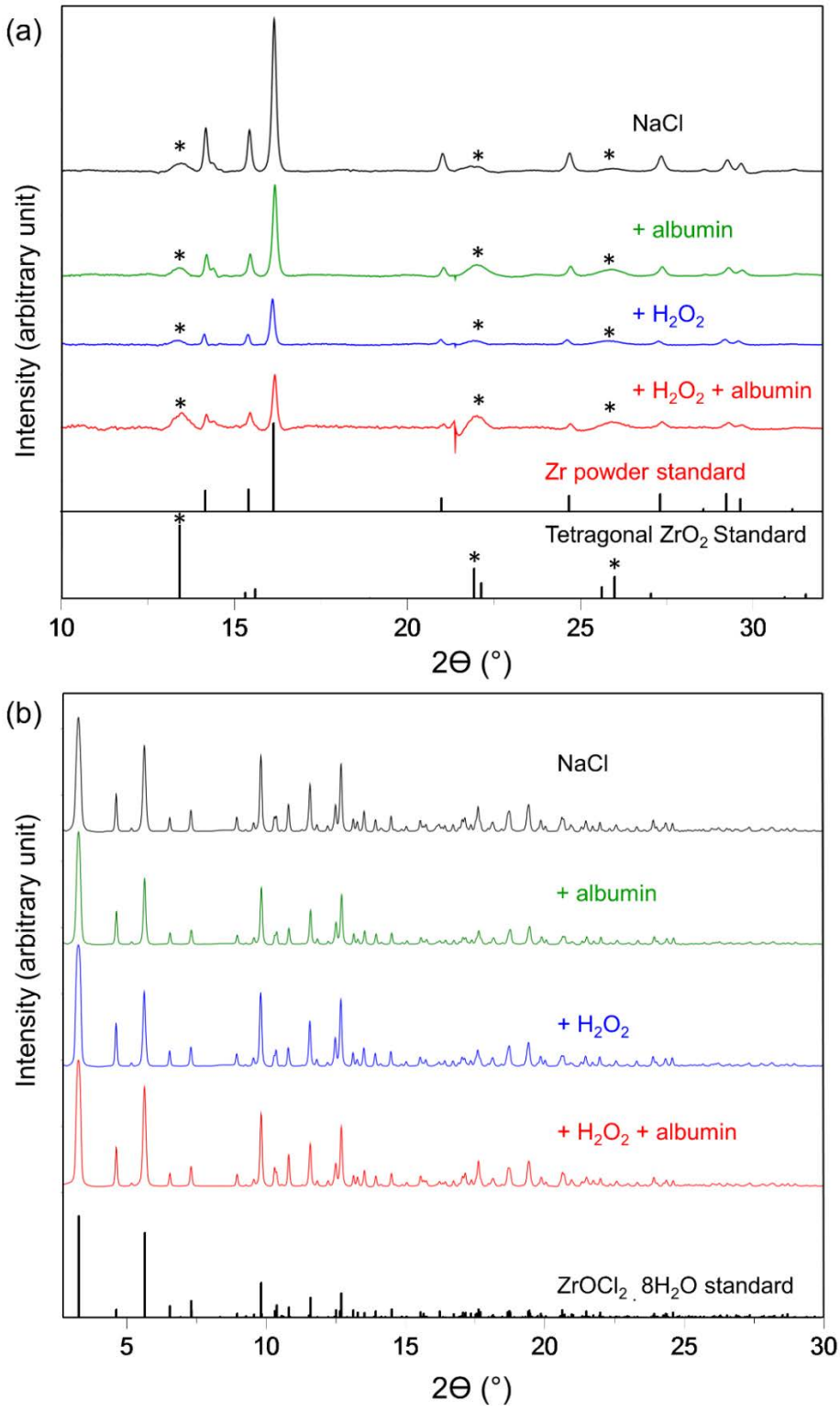

Figure 6-7. Stack plots of the averaged diffraction patterns from a) black corrosion products in 0.9% NaCl with and without addition of 0.1% H_2O_2 and/or 4% albumin; b) salt layer in 0.9% NaCl with and without addition of 0.1% H_2O_2 and/or 4% albumin in Zr artificial pits at 0.8 V (Ag/AgCl) and room temperature. Standards of Zr powder, ZrO_2, $ZrOCl_2 \cdot 8H_2O$ are shown at the base of the figure.

6.7 XANES of Zr solution species

Figure 6-8a shows a series of normalised XANES spectra for solution species in a Zr artificial pit grown in at 0.8 V (Ag/AgCl) in 0.9% NaCl + 4% albumin + 0.1% H_2O_2 as well as Zr reference compounds. The spectra of the Zr^{4+} reference compounds are all very similar, and show identical features to the spectra of the artificial pit solution species: a relatively featureless edge feature with an absorption edge peak at 18,020 eV and a weak pre-edge peak, more easily observed in the first derivative (Figure 6-8b), at 18,000 eV. This confirms that the solution species in the artificial pit is Zr in the tetravalent state, but no further information on its co-ordination environment can be inferred.

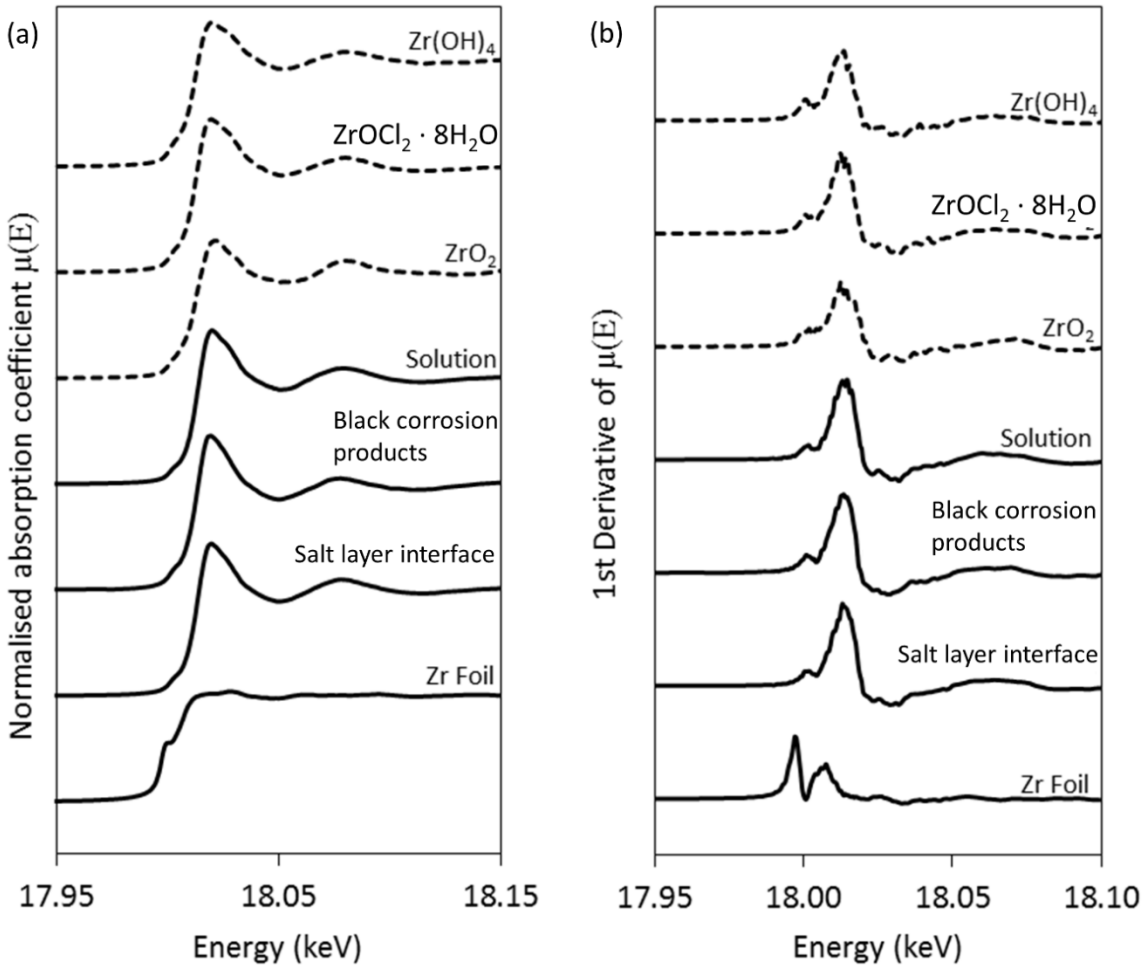

Figure 6-8. (a) Normalised XANES spectra of solution species as well as Zr reference compounds ZrO_2, $Zr(OH)_4$, $ZrOCl_2 \cdot 8H_2O$. The solution spectrum was measured from a Zr artificial pit previously shown in Figure 6-2. (b) are first derivatives of the spectra shown in (a).

6.8 *ex situ* microscopy of Zr corrosion products and its dissolving interface

6.8.1 SEM of the dissolving Zr interface

Figure 6-9 shows SEM images of different regions of the Zr surface from an artificial pit grown at 0.8 V (Ag/AgCl) in 0.9% NaCl + 4% albumin + 0.1% H_2O_2 for approximately 5 h. It can be seen that the corroding interface shows a high level of roughness (Figure 6-9a), and in some areas localised variations of roughness were also observed (Figure 6-9b).

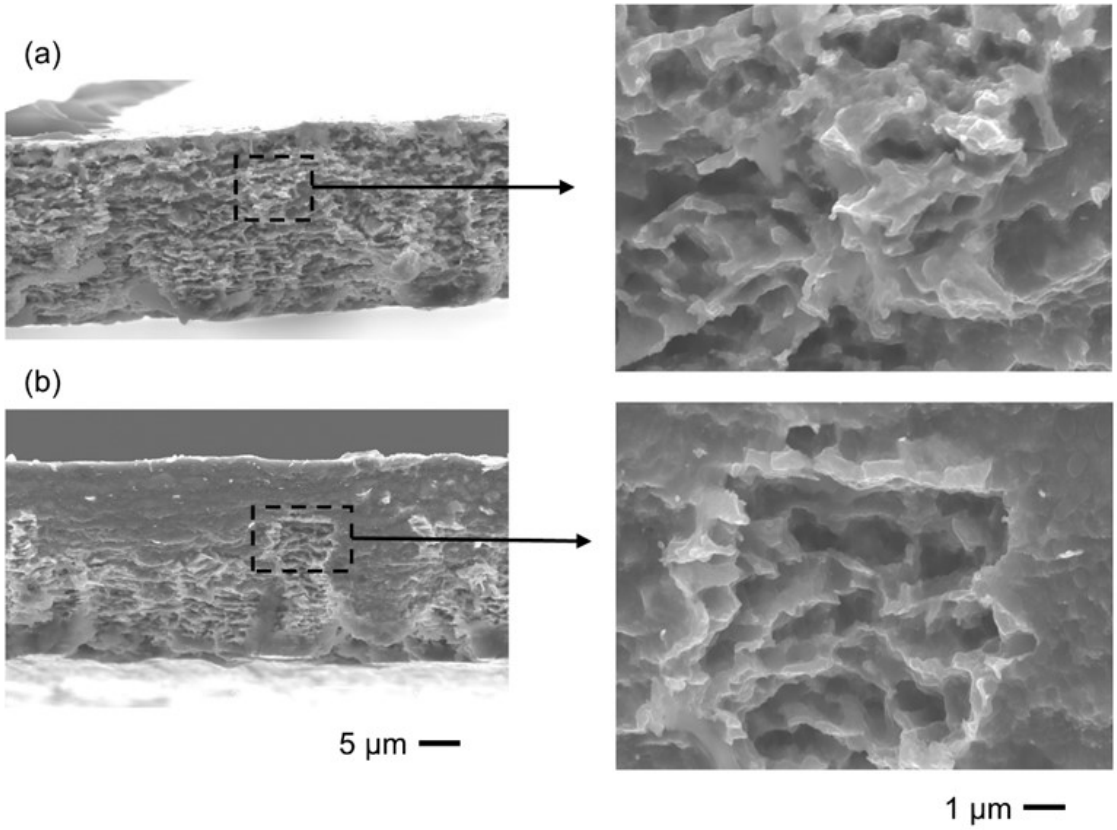

Figure 6-9. SEM images of different regions, (a) and (b), of the top surface of a Zr artificial pit grown at 0.8 V (Ag/AgCl) in 0.9% NaCl + 4% albumin + 0.1% H_2O_2 for approximately 5 h at ambient temperature.

6.8.2 TEM of Zr corrosion products

TEM with EDX was used to identify the chemical compositions and morphologies of corrosion products collected from the Zr artificial pit cavity (Figure 6-10). EDX confirmed the presence of Zr metal particles with a composition of 98.9 $\pm$ 0.2% Zr (marked as * in Figure 6-10). The compositions from individual point analysis are shown in Table 6-1. Some metal fragments appeared to show some directionality to the dissolution, with parallel strips of metal with sizes up to 2 µm, although smaller fragments were seen. The compositions of corrosion products (marked as Θ in Figure 6-10) showed 82% of Zr and 18% of O, suggesting the presence of Zr oxides/hydroxides. It can be

seen that these Zr oxides/hydroxides are in a “mesh” morphology engulfing the metal particles.

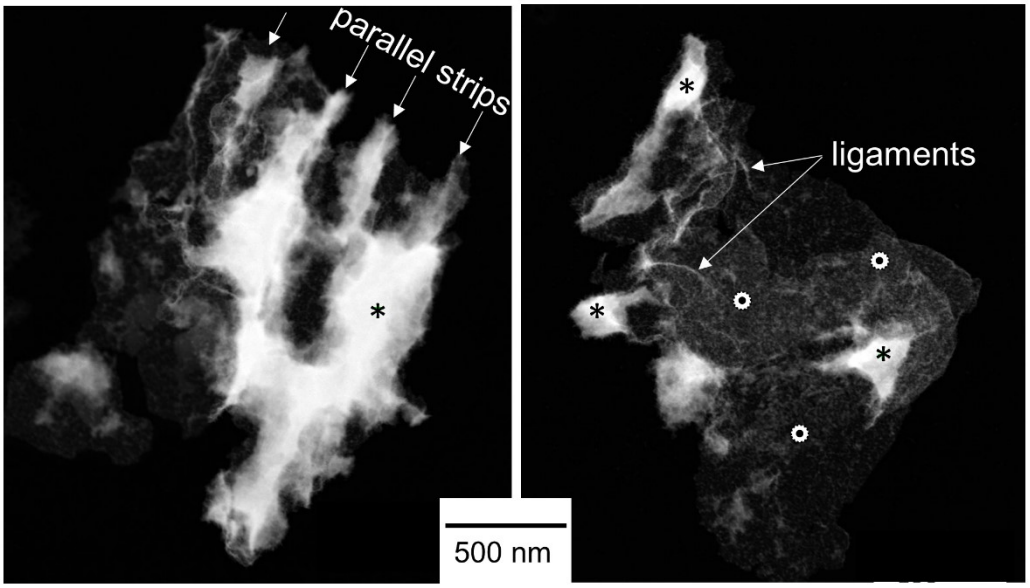

wt%	Zr	O	n
*	98.9 ± 0.2	1.1 ± 0.2	3
⊙	82 ± 2	18 ± 2	4

Figure 6-10. TEM images (dark field) of corrosion products from Zr artificial pit grown at 0.8 V (Ag/AgCl) in 0.9% NaCl for 3 h, at ambient temperature. Positions of EDX point analysis are marked with * and Θ, and relative compositions (wt%) are shown in the Table with mean values (n=3 for position * and n=4 for position Θ) and standard deviation. Features of the morphology (ligaments and parallel strips) of fragments are labelled. The direction ‘Parallel strips’ is associated with the rolling direction of the Zr foil.

Table 6-1. EDX compositions (all in wt%) of points as indicated in Figure 6-10.

Composition (wt%) / Position of EDX point analysis	Zr	O	Cl
* 1	98.8	1.1	0.1
* 2	99.1	0.9	0
* 3	98.7	1.3	0
* 4	99	1	0
Θ 5	83.4	16.6	0
Θ 6	83.9	16.1	0
Θ 7	79.9	20.1	0

6.9 Electrochemical polarisation on bulk Zr surfaces

6.9.1 Anodic Polarisation

Figure 6-11a shows anodic polarisation curves for bulk Zr samples in 0.9% NaCl solution with or without addition of H_2O_2 and/or albumin. It can be seen that the open circuit potentials of Zr in 0.9% NaCl were shifted to a more positive direction by addition of H_2O_2, and slightly shifted to negative directions by addition of albumin. The open circuit potentials in the presence of both H_2O_2 and albumin were found to be between those in solutions containing H_2O_2 or albumin individually. The bulk Zr samples were passive with current densities in the range of 3 to 10 μA/ cm^2 for all solutions up to approximately 500 mV (vs. SCE), at which point the current density increased rapidly above the “pitting potential”. Figure 6-11b shows pitting potentials in the different testing solutions, which varied from 550 to 1000 mV (vs. SCE) and were found to be similar regardless of the presence of H_2O_2 and/or albumin in 0.9% NaCl.

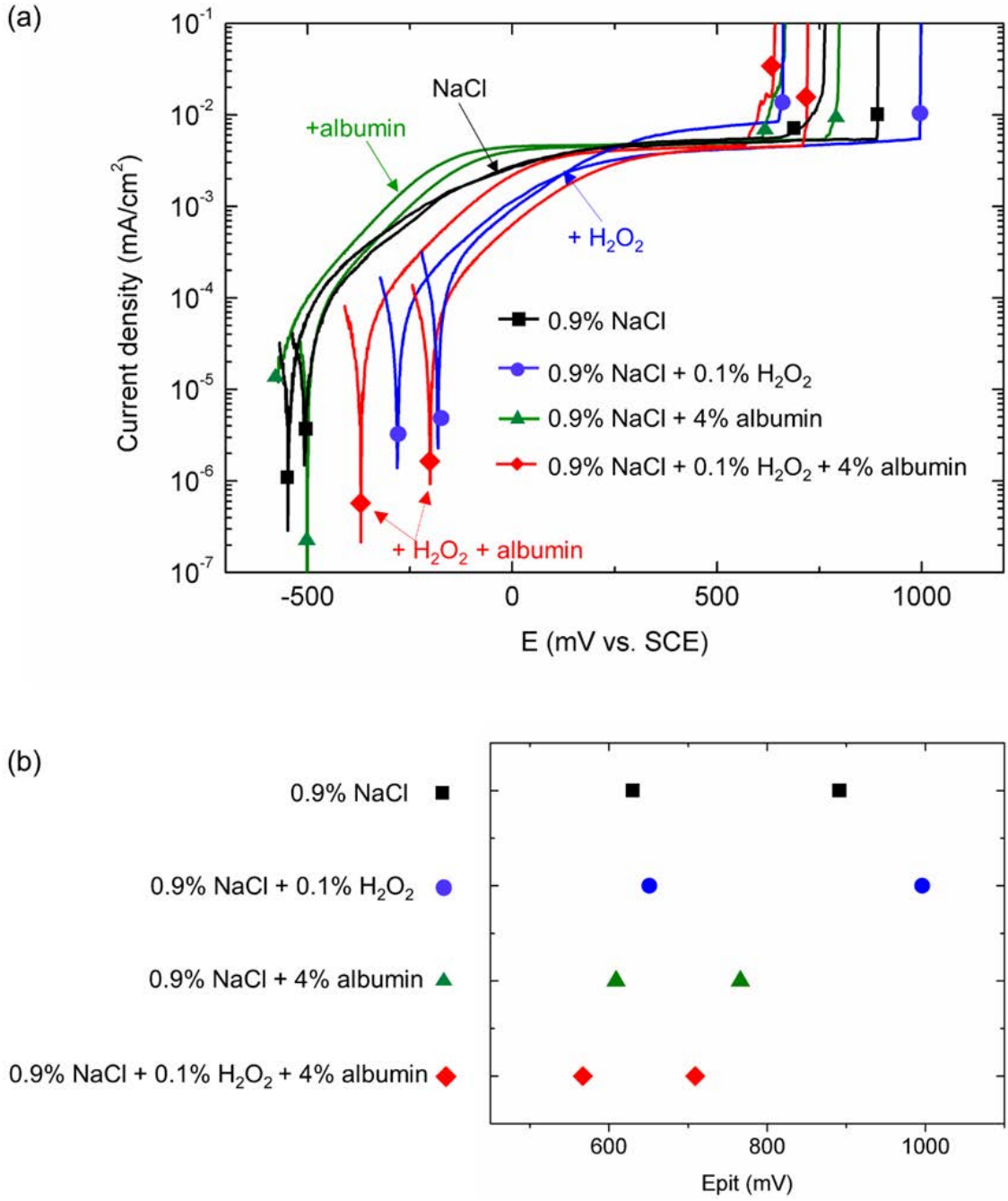

Figure 6-11. (a) Anodic polarisation of bulk Zr samples in 0.9% NaCl, with and without addition of 0.1% H_2O_2 and/or 4% albumin at 37 ± 1°C after 1 h at OCP. Scan rate was 1mV/s. Potentials are referenced to a standard calomel electrode (SCE). (b) Pitting potentials from the data shown in (a), as the potential at 0.1 mA/cm^2 was reached.

6.9.2 SEM of Zr pits following anodic breakdown

Figure 6-12 shows pit morphologies on bulk Zr samples after anodic polarisations in 0.9% NaCl with and without presence of H_2O_2 and/or albumin. It was observed that pit surfaces exhibited varying localised roughness in all solutions, regardless of the presence of H_2O_2 and/or albumin in 0.9% NaCl. At higher magnifications, localised areas inside the pit showed honeycomb-like structure, consistent with undercutting processes likely to lead to the formation of metal fragments (indicated by arrows in Figure 6-12b).

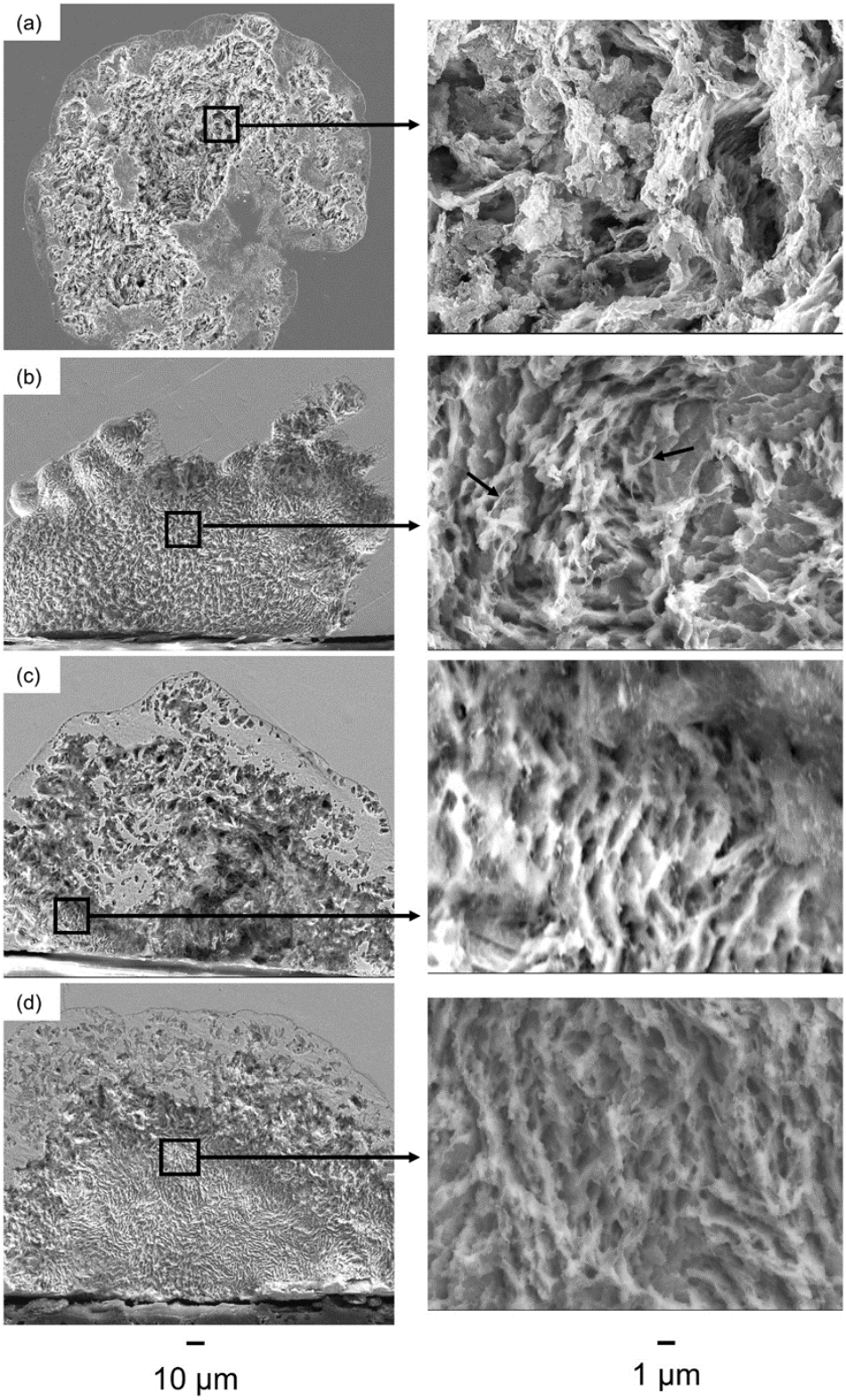

Figure 6-12. SEM images of pits on bulk Zr surfaces after anodic polarisation (Figure 6-11) in (a) 0.9% NaCl; (b) 0.9% + 4% albumin; (c) 0.9% NaCl + 0.1% H_2O_2; (d) 0.9% NaCl + 0.1% H_2O_2 +4% albumin. Arrows indicated in part (b) show evidence of metal fragments inside the pit.

6.10 Discussions

6.10.1 Formation of Zr metal fragments

Zr metal fragments were detected in-situ by XRD in the pit cavity (Figure 6-2b), including at locations in the pit 'bulges' at some distance from the original location of the bulk foil (Figure 6-3b). The original foil showed distinctive anisotropy (Figure 6-4a) owing to the preferential alignment of crystals with the rolling direction during manufacture. The Zr fragments in individual point measurements showed some anisotropy but with different orientations (Figure 6-4b and c), whereas the average number of diffraction patterns through the thickness of the corrosion product layer (Figure 6-4d), was more consistent with a Zr powder standard (156). TEM was subsequently used to characterise the corrosion products (Figure 6-10) and Zr metal fragments were identified by EDX analysis. Some metal fragments were found to show parallel 'strips', and 'ligament' morphologies with sizes ranging from nm to < 2 µm (Figure 6-10).

The dissolving interface of Zr exhibited a high level of roughness for both Zr artificial pits, and in pits on bulk Zr samples after anodic polarisation (Figure 6-9a and Figure 6-12). A similar observation was reported by Palit and Gadyar (54) who showed that the dissolving surfaces of Zr pits were irregular, exhibiting a 'spongy' morphology. It was also claimed that in the active growing pit, 'a black powder' was formed which was shown to contain α-Zirconium by X-ray analysis (56), supporting the findings of this study. Although the dissolving interface was highly roughened at multiple locations, there was also variation in roughness across localised areas (Figure 6-9b).

Based on the XRD measurements, the sub-micron size and fragmented morphologies of Zr fragments, and the highly roughened dissolution surfaces, it can be speculated that Zr metal fragments are produced by an undercutting mechanism which is well established in stainless steel systems (159). Pits on stainless steel grow by undercutting of the passive metal surface. The upward growth of lateral lobes perforates the metal surface and produces metal particles leaving a porous cover known as a 'lacy cover' (159). Similar observations on the formation of metal particles as a result of dissolution process have been reported in commercially pure (CP) Ti artificial pits (129). Micron-sized Ti metal particles were detected from a pit cavity, generated by only an electrochemical corrosion process. It was proposed that pits only propagate at the front where the metal ion concentration is sufficiently high, while the remaining pit surface is passive, and the propagating front grows by undermining the metal and perforating the surface generating metal particles (129).

6.10.2 $ZrOCl_2 \cdot 8H_2O$

$ZrOCl_2 \cdot 8H_2O$ was identified at the corrosion front, in the artificial pit and formed a salt layer a few hundred-microns thick above the dissolving interface (Figure 6-2b and Figure 6-6). Crystal coarsening observed further out into the solution (Figure 6-5e). Hydrated Zr^{4+} ions are reported to be stable in strongly acidic solutions (H^+, 1 M) and in a concentration lower than 10^{-4} M (160, 161). In more concentrated and/or less acidic solutions, Zr^{4+} will undergo a vigorous hydrolysis reaction and forms zirconyl ions i.e. $[Zr_4(OH)_8 \cdot 16H_2O]^{8+}$ that are kinetically

stable (162). In chloride containing environments, the zirconyl ions can form zirconyl chloride octahydrate ($ZrOCl_2 \cdot 8H_2O$) which was observed as the dominant species in the XRD data.

The zirconyl species $[Zr_4(OH)_8 \cdot 16H_2O]^{8+}$ is a complex, consisting of four Zr atoms in the corners of a slightly distorted square plane and linked by double hydroxo bridges. Four additional water molecules are bound to each Zr atom so that the Zr atom is coordinated by eight O atoms in a distorted square antiprism (157). The remaining water molecules and chloride ions form a matrix which holds the zirconyl complexes together to form $ZrOCl_2 \cdot 8H_2O$ (157).

The clinical relevance of $ZrOCl_2 \cdot 8H_2O$ species could be associated with situations where rapid dissolution interfaces occur, which could be encountered when passive films are deteriorated or ruptured such as during mechanically assisted crevice corrosion (MACC), leading to a burst of dissolution (62).

6.10.3 Tetragonal ZrO_2

Tetragonal ZrO_2 was detected, in-situ, in regions where black corrosion products were visible (Figure 6-2 and Figure 6-3). Broadening of the diffraction peaks of tetragonal ZrO_2 (marked with asterisks in Figure 6-2b and Figure 6-3b) is likely to be attributable to particle size broadening. The ZrO_2 crystallite size was estimated using the Scherrer equation (163) (Equation 6-1),

Equation 6-1

$$B = \frac{K\lambda}{L\cos\theta}$$

Where B is peak width determined by full width half maximum (FWHM) in radians, K is the Scherrer constant and here assumed to be 1, λ is the wavelength of the X-ray, L is particle size and Θ is Bragg's angle in degrees. Peak broadening was considered to be attributed solely by a particle size factor and instrumental broadening was considered negligible in this case. A Williamson-Hall plot (164) was created by plotting BcosΘ against sinΘ from data at the three reflection planes corresponding to the three major peaks of ZrO_2 from the averaged diffraction pattern shown in Figure 6-3b. The plot gives the size component (Kλ/L) from the intercept, which was 0.0062 and suggests a particle size of ~10 nm. The size estimation was consistent with TEM/EDX observations which was consistent with the presence of nano-scale Zirconium oxides/hydroxides (82% Zr and 18% O in wt%, Figure 6-10).

Nano-scale ZrO_2 particles can be synthesised by hydrolysis of an aqueous solution of $ZrOCl_2 \cdot 8H_2O$ (165, 166). Hydrolytic polymerization of $ZrOCl_2 \cdot 8H_2O$ solutions, produces a hydrated amorphous gel of ZrO_2. This can be transformed into crystalline phases such as monoclinic and tetragonal ZrO_2 on heating, with the phase formed, dependent on the precipitation conditions (166). It is reported that the crystal structure of ZrO_2 is dependent on the pH of the precipitation solution and the time taken to attain this pH, although the thermodynamic stable phase of crystalline ZrO_2 is monoclinic at room temperature (166, 167). Tetragonal ZrO_2 was found to be formed more effectively in precipitation solutions of higher pH and with slower precipitation rates. Further studies also propose that the tetragonal phase can be stabilised against transformation to monoclinic if the particle size is less than 30 nm (166-168). In this study,

tetragonal ZrO_2 was found dispersed above the $ZrOCl_2 \cdot 8H_2O$ salt layer towards the pit mouth when Zr artificial pits were grown for 3-5 h. Although the exact formation mechanism is not fully understood as there is no thermal factor evident, it is not unreasonable to propose that more neutral pH conditions (further away from the dissolving interface) and a slow precipitation process facilitated the formation of tetragonal ZrO_2 by polymeric hydrolysis of the $ZrOCl_2 \cdot 8H_2O$ solutions (166, 167).

6.10.4 The effects of H_2O_2 and albumin on electrochemistry of Zr and formation of Zr corrosion products and their biomedical implications

It can be observed in Figure 6-1 that the current densities of a Zr artificial pit growing at 0.8 V were stabilised at similar values in different solutions and unaffected by the presence of H_2O_2 and/or albumin, suggesting similar electrochemical dissolution rates. Similar pit growth rates were also observed when considering the role of H_2O_2 and/or albumin, although the presence of H_2O_2 seemed to be associated with a slower growth rate at later time periods. Further measurements would be required to confirm this behaviour. Regarding the electrochemistry of bulk Zr surfaces, as can be seen in Figure 6-11, the addition of H_2O_2 and/or albumin in physiological saline did not have an significant effect on the passive current densities and pitting potentials. A comparison of pit morphologies following anodic breakdown showed a similar characteristic ‘honeycomb’ morphology as well as a rough pit surface regardless of the presence of H_2O_2 and/or albumin in physiological saline (Figure 6-12). In-situ XRD characterisation of Zr corrosion products in pits at

0.8 V demonstrated the generation of the same corrosion species, namely Zr metal fragments, tetragonal ZrO_2 and $ZrOCl_2 \cdot 8H_2O$ (Figure 6-7). Similarly, identical corrosion species were observed in Zr artificial pits growing at 1.3 V, suggesting replication of the pit chemistry at higher potentials. Therefore, it can be concluded that H_2O_2 and/or albumin induces very limited effects on the pitting susceptibility and pit chemistry of Zr in physiological saline. The behaviour of Zr is different from that of Ti alloys, where H_2O_2 and albumin have a significant effect on passive behaviour (17).

Corrosion products including small micron and sub-micron sized metal particles have frequently been identified in retrieved peri-implant tissues associated with a variety of devices and metal substrates (7, 127, 169). It is also accepted that the implant degradation products induce inflammatory responses in the peri-implant environment, leading to adverse clinical outcomes such as bone resorption and aseptic loosening (170). When considering the potential biological ‘reactivity’ of corrosion species identified in this study, it has been previously shown that sub-micron sized (0.2–0.9 µm) Zr based particles (Zr-2.5Nb particles and ZrO_2) can be directly toxic to bone (osteoblast) and stromal cells (fibroblast) as well as induce an inflammatory response in innate immune cells, although to a less extent than that of Ti6Al4V and CoCrMo particles (128). Soluble Zr^{4+} ions in chloride solution have also been shown to induce a decrease in the proliferation of (MG-63) osteoblasts, be moderately inhibitory to fibroblasts, and moderately toxic to osteoblasts, fibroblasts and lymphocytes (50% reduction in viability at concentration between 0.5 to 5 mM (171, 172). Although not the focus of this study, it is likely that the corrosion

products characterised will elicit biological responses which should be carefully assessed prior to considering Zr usage as an implant element.

6.11 Conclusion

In-situ synchrotron X-ray diffraction and XANES were used to characterise corrosion products in Zr artificial pits in 0.9% NaCl (physiological saline) with the presence or absence of 0.1% H_2O_2, or 4% albumin, or their combinations.

In solutions of 0.9% NaCl with both 0.1% H_2O_2 and 4% albumin, Zr fragments and tetragonal ZrO_2 were found dispersed distant from the corroding interface, and $ZrOCl_2 \cdot 8H_2O$ crystallites were found close to the corroding interface and coarsened further out into the solution. XANES measurements of the solution showed spectra that were identical to a number of Zr reference compounds confirming the Zr solution species were in a tetravalent state.

Diffraction patterns of the Zr foil were anisotropic whereas Zr fragments seen inside of the pit gave an isotropic pattern. The fragments generated appearred anisotropic but randomly oriented and dispersed in the pit cavity. TEM of the corrosion products showed the Zr fragments to be sub-micron size. SEM on the dissolved surface of an Zr artificial pit showed a highly-roughened dissolution interface with variability in roughness in localised areas. Therefore, it is likely that Zr fragments are produced by an undercutting mechanism.

The speciation of the corrosion products was not affected by the presence or absence of H_2O_2, or albumin, or their combinations in 0.9% NaCl.

Anodic polarisation of bulk Zr samples in physiological saline exhibited similar passive current density and pitting potentials in both the absence and presence of H_2O_2, albumin and their combinations. SEM images showed similar pit

morphologies when compared across the different solutions. Therefore, H_2O_2 and albumin are proposed to have limited effects on the bulk electrochemistry of Zr and its pitting susceptibility.

7 GENERAL DISCUSSION AND FUTURE WORK

7.1 General discussion

7.1.1 The need for improved environmental conditions and methods for corrosion testing

Standard corrosion assessments (130-134) of metallic biomaterials do not necessarily provide a reliable estimation of the implant corrosion that occurs *in vivo*. Clinical observations of significantly higher levels of corrosion than expected have been attributed to the biological complexity of the peri-implant environment, and in particular, crevice geometries such as those found in modular implants. Extensive studies have been carried out to identify corrosion-mediating factors which have been shown to include bio-chemical species, proteins and cells (see section 2.4). It has been identified that the inflammatory system, which include innate immune cells and cellular physiological products such as ROS species, can significantly influence the corrosion of implanted metals (13, 14, 173).

Inflammation is associated with the production of ROS species, by immune cells that have infiltrated the peri-implant tissues. Common ROS species include superoxide anions and H_2O_2 (24, 25). H_2O_2 is known as a strong oxidant and its effect on corrosion of Ti has been extensively studied, albeit using a great variation in the levels of H_2O_2 exposure in simulated *in vitro* tests (17-21, 23). It is agreed that H_2O_2 increases corrosion of Ti (and Ti6Al4V) by forming Ti(IV)-H_2O_2 complexes (16-22), leading to formation of rougher, thicker and more porous surface oxide films.

In this study, exposure of Ti6Al4V surface to H_2O_2, at the levels relative to the lowest concentrations used in previous studies (17-21, 23), was demonstrated to induce more corrosion and result in the formation of thick corrosion product layer in mud-cracking morphology. Furthermore, the prolonged exposure (up to 120 h) of H_2O_2 showed a reduced corrosion rate with time, which was attributed to the thick surface layer of corrosion products that act to block further dissolution. If the role of H_2O_2 alone is significant for implant degradation *in vivo*, it would appear, based on studying the addition of H_2O_2 on corrosion alone, that long exposure of the representative conditions would lead to a reduced corrosion rate.

Albumin is an alternative important corrosion mediating factor, which has been subject of considerable attention because it is the most abundant protein in extracellular tissue fluid (26). It is generally accepted that albumin inhibits cathodic reactions on Ti surface by adsorption (17, 92-95). However, the effect of albumin on corrosion of Ti6Al4V (and CP Ti) has been inconsistently reported as promoting (17, 92, 96, 99), inhibiting (94, 95, 99) or producing no effect (98, 101, 102). It has been suggested that albumin interacts with the metal surface in two ways: adsorption in which the metal surface is protected from corrosion by the adsorbed protein film (94, 95); chelation in which soluble metal-protein complexes are formed, enhancing the rate of dissolution (92, 106, 107). It is also worthy to point out that the metal-protein interactions can exist in either or both ways. If the role of albumin alone is significant for implant degradation *in vivo*, it would be anticipated that little or no significant corrosion would occur.

Although the role of H_2O_2 or albumin on corrosion of Ti has been studied extensively in isolation, their combined effect has not been investigated comprehensively. Yu et al. found that, for the first time, the presence of both albumin and H_2O_2 in physiological saline (0.9% NaCl, ASTM standard (133, 134)) synergistically enhances the corrosion of Ti6Al4V (17). It was also shown that the effect of the combined species was only exhibited to enhance corrosion after long-term (2 weeks) incubation, but from short-term (standard) electrochemistry tests, albumin appeared to supress the corrosion of Ti6Al4V in the presence of H_2O_2.

In this study, it was shown that albumin induces a time-dependent dissolution of Ti6Al4V in the presence of H_2O_2. It was demonstrated that at short times (<24 h), albumin supresses the rate of dissolution in the presence of H_2O_2 and at longer times, it accelerates the corrosion by dissolving the corrosion product layer. Furthermore, the rate of dissolution of Ti6Al4V was also found to vary with potentials, a higher Ti release was found at a lower potential, depending on the environmental exposure conditions. It is clear that studies into albumin or H_2O_2 alone would not have predicted the observed behaviour *in vivo*. Moreover, the studies Yu et al. (17) which produced conclusions based on early time points failed to predict the temporal variation in corrosion that was seen here. Future testing must consider the combination of species and adequately associate corrosion behaviour over time.

The time-dependent enhanced corrosion of Ti6Al4V in the presence of H_2O_2 and albumin was associated with possible desorption and/or exchange of

absorbed albumin complexed to metal ions, as reported previously in protein interactions with stainless steel systems (106). Extrapolation of the synergistic action of albumin and H_2O_2 on corrosion of other metallic systems is uncertain. Although Zr has been used as a common element in alloy compositions for biomedical implants (28, 29) (174-178) but corrosion resistance of pure Zr in biological context has been poorly characterised. From the present work, the corrosion behaviour of Zr was characterised in the same simulated physiological environment with Ti6Al4V. It was found that the corrosion of Zr was not significantly affected by the presence of H_2O_2 and/or albumin in physiological saline, including its passivation and pitting susceptibility. This suggests the interactions of albumin with different surface oxide films including TiO_2 and ZrO_2, are different. This finding is not surprising given the different physiochemical properties of the interfaces. Therefore, it should be expected that TiZr binary alloys may provide a better resistance to dissolution in the presence of the combined species, in comparison to Ti, giving the surface oxides consisting of both TiO_2 and ZrO_2.

It has also been previously reported that the albumin interactions are kinetically different with passive and active metals such as pure Fe and stainless steels (106), leading to the opposite effects on metal dissolution. Therefore, the corrosion behaviour of metallic biomaterials in more physiologically relevant testing electrolytes can be varied significantly, when compared with standard testing solutions, making it useful to discriminate between materials' degradation behaviour in physiological environments.

The work presented in this thesis highlights the findings of the variation of corrosion rates with time and shifts in potentials in more realistic solutions where implants were exposed to physiological environments, which are useful to be considered for assessment of corrosion resistance of metallic biomaterials. Whilst the focus of this study is on the combined effect of H_2O_2 and albumin on corrosion of Ti6Al4V, there are many other corrosion mediators that the surface of the implant may be exposed to, which requires further, more comprehensive investigations.

7.1.2 Characterisation of degradation products in simulated physiological environment

The breakdown of passive implant surface films occurs *in vivo* and is associated with either wear and/or corrosion. It has been demonstrated that this leads to the generation of particulate products and/or busts of metal ion release, which themselves may readily react to form insoluble precipitates for example oxidation of Ti ions and reactions between Cr and phosphate. Metal degradation products have been detected both locally (127, 128, 170) and sites distant from the implant in humans (179, 180). Enhanced levels of implant metal species (such as Co, Cr, Ti, Ni Al and V) have been reported in peri-prosthetic tissues and fluids such as serum, urine and whole blood (8, 127, 128, 170, 181). Metal species found in tissues and disseminated systemically vary in size, chemical forms such as inorganic precipitates and organometallic complexes, and can elicit pathophysiological consequences such as periprosthetic bone loss (65). Therefore, it is essential to understand both the chemical and physical forms of metal degradation products to fully assess its biocompatibility.

The most significant release of metal debris from implant is associated with articulating prostheses, where the passive films are fractured with subsequent active dissolution, in contrast to passive dissolution (65). In this study, localised corrosion (breakdown of passive films) of Zr was simulated by growing a Zr 'artificial pit' electrochemically (137, 141) The as-produced corrosion products in the 'artificial pit cavity' were characterised *in situ* by synchrotron radiation techniques, which had been successfully applied in previous studies (138, 182). It was found that in physiological saline, Zr corrosion products were identified to be $ZrOCl_2 \cdot 8H_2O$, Zr metal fragments and tetragonal ZrO_2. Furthermore, these identified products were found unchanged with variations in the exposure environment including the presence of H_2O_2, or albumin or their combinations in physiological saline.

The observation of small micron-sized Zr metal fragments (observed with TEM) together with the particle morphology and a rough dissolving interface of Zr suggested an undercutting mechanism leading to the release of fragments of metal species from a passivated surface. Similar observations have been reported in a Ti 'artificial pit' system in which metallic Ti and oxide species were generated by an electrochemical dissolution process of a passivated surface (129). Therefore, these observations suggest that metal species can be generated purely by a localised corrosion process, in absence of wear. Clinically it has been evidenced that fine fragments of both Ti and oxides were detected in the retrieved peri-implant tissue when mechanical loading is not considered at risk. It was proposed to be attributed to micro-motion and localised corrosion processes in the passivated surface crevices (7). Therefore,

further studies are needed to be carried out regarding the physical and chemical mechanisms of implant degradation of *in vivo.*

7.1.3 Corrosion behaviour and development opportunities of binary TiZr alloys

Binary TiZr alloys may offer more suitable mechanical properties when compared with CP Ti for clinical situations where narrow diameter implants are needed. A commercialised example (Roxolid®, Straumann), containing between 13%-18% Zr with exact composition undisclosed, has been demonstrated to possess enhanced mechanical strength with similar osseointegration properties and 'biocompatibility' when compared with CP Ti Grade IV (2). The corrosion behaviour of TiZr alloys had been characterised in various exposure environments, but with limited biological relevance (44, 77, 183-185). Whilst it is commonly agreed that TiZr alloys possess enhanced corrosion resistance and passivity compared with CP Ti, systematic studies are needed to understand how Zr modifies the corrosion of Ti in a more approximated peri-implant environment in order to make reliable predictions on its likely behaviour *in vivo*.

In this study, the effect of Zr additions on corrosion of Ti was systematically studied, with effective Zr concentrations from 0, 5, 15, 50, to 100%. It was found that in highly acidic environment (2 M HCl), mimicking localised acidification as a result of processes such as MACC, Zr additions to Ti enhanced its oxide film stability and passivity to both active and passive dissolution. In a more inflammatory environment (physiological saline with addition of H_2O_2), Zr additions to Ti progressively supressed the enhanced corrosion induced by

H_2O_2. In a cellular culture environment, in which ROS (including H_2O_2) were produced by stimulated macrophages, the pattern of supressed Ti release (normalised) by addition of Zr was identified again, mirrored with the order of corrosion resistance in the presence of H_2O_2. The consistent patterns of enhanced corrosion resistance for both electrochemical dissolution in the presence of H_2O_2 and cellular induced metal release associated with ROS production, suggests that ZrO_2 has a better resistance to degradation in the oxidative environment when compared with TiO_2. Therefore, the passivity of TiZr alloys were enhanced when compared with CP Ti due to the presence of TiO_2 and more resistive (to dissolution) ZrO_2 on the surface.

However, it is well known that Zr has high pitting susceptibility, especially in chloride-containing environment. In this study, the higher addition of Zr to Ti (such as Ti50Zr vs. Ti5Zr and Ti15Zr) has been demonstrated to be more susceptible to pitting breakdown in all testing solutions. Based on the range of TiZr compositions investigated in this study, as well as the consideration of the optimum balance of passivity and pitting resistance, we propose that Ti15Zr is a promising alloy for future use in clinical applications, but may not necessary be the optimum composition.

Systematic studies on different TiZr compositions would open many opportunities to fully understand and explore the end-route behaviour by modifying microstructures, chemical compositions of surface oxides, and using post-processing manufacture routes. Future work can be conducted to find any correlation between the structure and properties with optimised behaviour.

Binary TiZr alloys also offer possibilities for future development of new alloys. Addition of elements that are ‘biologically’ beneficial for clinical applications can be considered, to develop ternary alloys based on TiZr alloys. A preliminary ZrTi based ternary alloy has been developed, with minor additions of Ag, intended to enhance corrosion resistance and confer anti-microbial resistance (186). Future work can be conducted to develop more promising TiZr based ternary alloys with an optimised balance of enhanced corrosion and mechanical properties.

7.2 Future Work

7.2.1 Improved approximation of testing solutions to peri-implant environment

The synergistic action of albumin and H_2O_2 on corrosion of Ti6Al4V has been found to vary with time and shifts in potential in the present work. To extrapolate this synergistic effect with more biological relevance, the effect of H_2O_2 exposures of lower concentrations should be explored. Biologically relevant concentrations of H_2O_2- reflecting levels of cellular physiology, are often reported in the µM range (187). Identifying whether a threshold value of H_2O_2 concentration exists to maintain the synergistic actions of the two species is necessary.

Additionally, advanced corrosion characterisation methods should be used to complement conventional electrochemistry measurements in order to effectively detect ‘true’ corrosion rates therefore discriminate between different materials. For instance, advanced atomic emission spectroelectrochemistry (AESEC) method (27, 188), which provides ultra-high sensitivity to metal release *in situ*

as a result of corrosion and/or polarisation, has been shown powerful enough to discriminate real metal loss as a function of potential and/or time which are often overlooked by polarisation curves. Other complementary methods including mass spectroscopy (e.g. ICPMS), electrochemical impedance (EIS) should also be considered when necessary if corrosion behaviours are found similar irrespective of solution chemistry and materials from standard tests.

7.2.2 Further studies of corrosion tests on TiZr binary alloys

Corrosion of TiZr alloys were studied under various chemical or cellular exposures. Here, we observed a largely consistent pattern of corrosion resistance between different alloy compositions in all media. However, whether TiZr alloys exhibited an enhanced corrosion in the presence of albumin and H_2O_2 was not explored. Future studies can be carried out to investigate further on corrosion behaviour of TiZr alloys in physiological solutions with addition of relevant biomolecules such as albumin, or combination of protein and H_2O_2, at the same time considering the temporal effect as identified in Ti6Al4V systems.

7.2.3 Characterisation of degradation products of TiZr

Corrosion products of Zr have been characterised *in situ* using synchrotron X-ray methods. It has been found that the Zr speciation was consistent in regardless of the presence or absence of H_2O_2 and/or albumin, making it possible to predict the likely nature of the degradation products likely to be seen *in vivo*. A Similar approach can be used in future studies to study the corrosion products for TiZr alloys given its promising use in dental implant applications.

Artificial corrosion pits of TiZr can be used again to simulate localised corrosion process, for instance, pitting breakdown of Ti50Zr alloy found in this study. Advantage of artificial corrosion pits is the ability to generate corrosion products in simulated physiologically relevant environments.

7.2.4 Exposing cells to simulated corrosion products

To further investigate the biological consequence of detected or simulated corrosion products, cells can be exposed and stimulated to the forms of corrosion products identified *in vitro* and subsequent cell immune responses can be examined. For example, neutrophils, the predominate acute inflammatory cells in peri-implant sites, can be stimulated to the TiZr corrosion products such as mixed TiO_2 and ZrO_2 in nanometric size, and an array of subsequent neutrophil immune responses can be analysed including phagocytosis, respiratory burst and cytokine secretion. This experimental approach potentially provides new insights on the biological responses to metal degradation products and how cellular responses (e.g. generation of ROS species) can adversely affect corrosion.

7.2.5 Opportunities for the development of new TiZr based ternary alloys

TiZr binary alloys open up future opportunities for the development of ternary alloys for biomedical applications. A metastable β phase Ti-13Zr-13Nb ternary alloy (189) has been developed and used as orthopaedic implants, providing significantly improved mechanical properties and resistance to tribo-corrosion. Future work can be carried out to develop novel TiZr based ternary alloys,

incorporating minor additions of alloying elements, without deteriorating mechanical properties and biocompatibility. Preliminary studies have been carried out (but not presented in the thesis) to develop new ternary alloys with minor additions of Cu or Ag, to enhance anti-microbial activity. However, comprehensive work is required to engineer the metallurgical microstructure to optimally balance the mechanical properties, the corrosion resistance and biocompatibility.

8 CONCLUSIONS

Corrosion of Ti6Al4V alloy, CP Ti (Grade 2), CP Zr and TiZr binary alloys has been investigated in simulated physiological conditions approximating the per-implant environment. In addition, corrosion products of Zr have been characterised *in situ* to predict possible degradation products for service *in vivo*.

1. A time-dependent enhanced corrosion of Ti6Al4V has been found in the presence of H_2O_2, an inflammatory biomolecule encountered in peri-implant environment, and albumin, the most prevalent protein in blood plasma and extracellular tissue fluid, in 0.15 M NaCl:

   a) in short term ($t < \sim 22$ h), albumin inhibited the rate of dissolution in the presence of peroxide.

   b) over longer time periods (up to 120 h), the rate of dissolution was found to be higher than that in the absence of albumin, which was associated with the enhanced dissolution of peroxide corrosion products, resulting in the formation of a thinner oxide layer on the metal substrate.
2. Corrosion of Ti6Al4V in the presence of albumin and H_2O_2 was also found to vary with potential. Higher metal release was found at a lower potential.
3. In contrast to Ti6Al4V, corrosion of pure Zr was not found to be significantly affected by the presence of H_2O_2, or albumin, or their combinations in 0.15 M NaCl. Similar pitting susceptibilities and pits morphologies were also observed in the various electrolytes.
4. Corrosion products from Zr were characterised *in situ* using synchrotron X-ray methods by electrochemically growing a Zr artificial corrosion pit. In the pit cavity, $ZrOCl_2 \cdot 8H_2O$, tetragonal ZrO_2, and Zr metal fragments were

detected, and found to be consistent in morphology and speciation when generated in the presence or absence of H_2O_2, or albumin, or their combinations in 0.15 M NaCl.

5. The Zr metal fragments detected were found randomly dispersed and oriented in the pit cavity. TEM observations on Zr fragments (identified by EDX) showed morphologies in ‘strips’ with a size in small microns. In addition. the Zr dissolving interfaces were found to exhibit a high level of roughness. An undercutting mechanism was proposed whereby metal fragments can be produced purely by a corrosion process, in the absence of mechanical damage.
6. Corrosion of TiZr alloys has been systematically studied in simulated physiological environments. The effect of systematic Zr additions to Ti was found to progressively enhance Ti passivity, consistently in the various exposure conditions including acidic solutions (2 M HCl), neutral H_2O_2 containing 0.15 M NaCl, and cellular culture environment (macrophage cell culture).
7. Optimisation of Zr additions to Ti need to balance both enhanced passivity and pitting susceptibility (which increases with increasing Zr additions). Ti15Zr was the best performing composition identified from a corrosion prospective in this study.

9 REFERENCES

1. Lemons JE, Misch-Dietsh F, McCracken MS. Biomaterials for Dental Implants. In: Misch C.E. (ed.) *Dental Implant Prosthetics* (Second Edition). St. Louis: Mosby; 2015. p. 66-94.

2. Grandin HM, Berner S, Dard M. A Review of Titanium Zirconium (TiZr) Alloys for Use in Endosseous Dental Implants. *Materials*. 2012;5(8):1348-60.

3. Allum SR, Tomlinson RA, Joshi R. The impact of loads on standard diameter, small diameter and mini implants: a comparative laboratory study. *Clinical Oral Implants Research*. 2008;19(6):553-9.

4. Steinemann SG. Titanium--the material of choice? *Periodontology 2000*. 1998;17:7-21.

5. Okazaki Y, Gotoh E. Comparison of metal release from various metallic biomaterials in vitro. *Biomaterials.* 2005;26(1):11-21.

6. Cadosch D, Chan E, Gautschi OP, Filgueira L. Metal is not inert: Role of metal ions released by biocorrosion in aseptic loosening-Current concepts. *Journal of Biomedical Materials Research Part A*. 2009;91A(4):1252-62.

7. Addison O, Davenport AJ, Newport RJ, Kalra S, Monir M, Mosselmans JFW, Proops D, Martin RA. Do ‘passive’ medical titanium surfaces deteriorate in service in the absence of wear? *Journal of the Royal Society Interface*. 2012;9(76):3161-4.

8. Nuevo-Ordóñez Y, Montes-Bayón M, Blanco-González E, Paz-Aparicio J, Raimundez JD, Tejerina JM, Peña MA, Sanz-Medel A. Titanium release in serum of patients with different bone fixation implants and its interaction with serum biomolecules at physiological levels. *Analytical and Bioanalytical Chemistry*. 2011;401(9):2747.

9. Kalra S, The distribution and pro-inflammatory implant of titanium debris accumulation in the peri-implant environment [Ph.D. thesis]. Birmingham: University of Birmingham; 2013.

10. Dorr LD, Bloebaum R, Emmanual J, Meldrum R. Histologic, biochemical, and ion analysis of tissue and fluids retrieved during total hip-arthroplasty. *Clinical Orthopaedics and Related Research*. 1990(261):82-95.

11. Leopold SS, Berger RA, Patterson L, Skipor AK, Urban RM, Jacobs JJ. Serum titanium level for diagnosis of a failed, metal-backed patellar component. *Journal of Arthroplasty*. 2000;15(7):938-43.

12. Jacobs JJ, Skipor AK, Black J, Urban RM, Galante JO. Release and excretion of metal in patients who have a total hip-replacement component

made of titanium-base alloy. *Journal of Bone and Joint Surgery-American Volume*. 1991;73A(10):1475-86.

13. Gilbert JL, Kubacki GW. Oxidative Stress, Inflammation, and the Corrosion of Metallic Biomaterials: Corrosion Causes Biology and Biology Causes Corrosion. In: Butterfield DA, Dziubla T. (eds.). *Oxidative Stress and Biomaterials*: Academic Press; 2016. p. 59-88.

14. Mu Y, Kobayashi T, Sumita M, Yamamoto A, Hanawa T. Metal ion release from titanium with active oxygen species generated by rat macrophages in vitro. *Journal of Biomedical Materials Research*. 2000;49(2):238-43.

15. Yu F. Corrosion of Titanium for Biomedical Applications. [Ph.D. Thesis]. Birmingham: University of Birmingham; 2015.

16. Tengvall P, Lundström I. Physico-chemical considerations of titanium as a biomaterial. *Clinical Materials*. 1992;9(2):115-34.

17. Yu F, Addison O, Davenport AJ. A synergistic effect of albumin and H_2O_2 accelerates corrosion of Ti6Al4V. *Acta Biomaterialia*. 2015;26:355-65.

18. Takemoto S, Hattori M, Yoshinari M, Kawada E, Oda Y. Discoloration of titanium alloy in acidic saline solutions with peroxide. *Dental Materials Journal*. 2013;32(1):19-24.

19. Pan J, Thierry D, Leygraf C. Electrochemical and XPS studies of titanium for biomaterial applications with respect to the effect of hydrogen peroxide. *Journal of Biomedical Materials Research*. 1994;28(1):113-22.

20. Pan J, Thierry D, Leygraf C. Electrochemical impedance spectroscopy study of the passive oxide film on titanium for implant application. *Electrochimica Acta*. 1996;41(7–8):1143-53.

21. Pan J, Thierry D, Leygraf C. Hydrogen peroxide toward enhanced oxide growth on titanium in PBS solution: Blue coloration and clinical relevance. *Journal of Biomedical Materials Research*. 1996;30(3):393-402.

22. Mabilleau G, Bourdon S, Joly-Guillou ML, Filmon R, Baslé MF, Chappard D. Influence of fluoride, hydrogen peroxide and lactic acid on the corrosion resistance of commercially pure titanium. *Acta Biomaterialia*. 2006;2(1):121-9.

23. Tengvall P, Elwing H, Sjöqvist L, Lundström I, Bjursten LM. Interaction between hydrogen peroxide and titanium: a possible role in the biocompatibility of titanium. *Biomaterials.* 1989;10(2):118-20.

24. Fantone JC, Ward PA. Role of oxygen-derived free radicals and metabolites in leukocyte-dependent inflammatory reactions. *The American Journal of Pathology*. 1982;107(3):395-418.

25. Nakagawara A, Nathan CF, Cohn ZA. Hydrogen peroxide metabolism in human monocytes during differentiation in vitro. *Journal of Clinical Investigation*. 1981;68(5):1243-52.

26. Peters Jr T. Serum Albumin. In: Anfinsen CB, Frederic JTE, Richards M (ed.) *Advances in Protein Chemistry*. Volume 37: Academic Press; 1985. p. 161-245.

27. Wang JL, Liu RL, Majumdar T, Mantri SA, Ravi VA, Banerjee R, Birbilis N. A closer look at the in vitro electrochemical characterisation of titanium alloys for biomedical applications using in-situ methods. *Acta Biomaterialia*. 2017;54:469-78.

28. Niinomi M, Nakai M, Hieda J. Development of new metallic alloys for biomedical applications. *Acta Biomaterialia*. 2012;8(11):3888-903.

29. Zhao XL, Niinomi M, Nakai M, Ishimoto T, Nakano T. Development of high Zr-containing Ti-based alloys with low Young's modulus for use in removable implants. *Materials Science & Engineering: C*. 2011;31(7):1436-44.

30. McCracken M. Dental implant materials: commercially pure titanium and titanium alloys. *Journal of prosthodontics*. 1999;8(1):40-3.

31. Anthogyr SAS. *Summary report of AXIOM® 2.8* [Available from: https://www.accessdata.fda.gov/cdrh_docs/pdf14/K141450.pdf [Accessed 23 March 2017]

32. Osman R, Swain M. A critical review of dental implant materials with an emphasis on titanium versus zirconia. *Materials.* 2015;8(3):932.

33. Correa DRN, Vicente FB, Donato TAG, Arana-Chavez VE, Buzalaf MAR, Grandini CR. The effect of the solute on the structure, selected mechanical properties, and biocompatibility of Ti–Zr system alloys for dental applications. *Materials Science and Engineering: C*. 2014;34(0):354-9.

34. Atapour M, Pilchak A, Frankel GS, Williams JC, Fathi MH, Shamanian M. Corrosion Behavior of Ti-6Al-4V with Different Thermomechanical Treatments and Microstructures. *CORROSION*. 2010;66(6).

35. Kobayashi E, Matsumoto S, Doi H, Yoneyama T, Hamanaka H. Mechanical properties of the binary titanium-zirconium alloys and their potential for biomedical materials. *Journal of Biomedical Materials Research*. 1995;29(8):943-50.

36. Predel B. Ti-Zr (Titanium-Zirconium). In: Madelung O (ed.). *Pu-Re-Zn-Zr*. Berlin, Heidelberg: Springer Berlin Heidelberg; 1998. p. 1-3.

37. Ho WF, Chen WK, Wu SC, Hsu HC. Structure, mechanical properties, and grindability of dental Ti–Zr alloys. *Journal of Materials Science: Materials in Medicine*. 2008;19(10):3179-86.

38. Williams JC. Critical review: kinetics and phase transformations In: Jaffee RI and Burte HM (ed.). *Titanium Science and Technology; Proceeding*. Volume 3. New York: Plenum Press; 1973. p. 1434-94.

39. Gottlow J, Dard M, Kjellson F, Obrecht M, Sennerby L. Evaluation of a New Titanium-Zirconium Dental Implant: A Biomechanical and Histological Comparative Study in the Mini Pig. *Clinical Implant Dentistry and Related Research*. 2012;14(4):538-45.

40. Pound BG. Passive films on metallic biomaterials under simulated physiological conditions. *Journal of Biomedical Materials Research Part A*. 2014;102(5):1595-604.

41. Parr GR, Gardner LK, Toth RW. Titanium: the mystery metal of implant dentistry. Dental materials aspects. *Journal of Prosthetic Dentistry*. 1985;54(3):410-4.

42. Lausmaa J, Kasemo B, Mattsson H. Surface spectroscopic characterization of titanium implant materials. *Applied Surface Science*. 1990;44(2):133-46.

43. Milošev I, Metikoš-Huković M, Strehblow HH. Passive film on orthopaedic TiAlV alloy formed in physiological solution investigated by X-ray photoelectron spectroscopy. *Biomaterials*. 2000;21(20):2103-13.

44. Yu SY, Scully JR, Vitus CM. Influence of niobium and zirconium alloying additions on the anodic dissolution behaviour of activated titanium in HCl solutions. *Journal of the Electrochemical Society*. 2001;148(2):B68-B78.

45. Virtanen S, Milosev I, Gomez-Barrena E, Trebse R, Salo J, Konttinen YT. Special modes of corrosion under physiological and simulated physiological conditions. *Acta Biomaterialia*. 2008;4(3):468-76.

46. Sundgren JE, Bodö P, Lundström I. Auger electron spectroscopic studies of the interface between human tissue and implants of titanium and stainless steel. *Journal of Colloid and Interface Science*. 1986;110(1):9-20.

47. McQueen D, Sundgren JE, Ivarsson B, Lundstrom I, Af-Ekenstam, B, Svensson A, Brånemark PI, Albrektsson T. Auger electron spectroscopic studies of titanium implants. In: Lee AJC, Albrektsson T, Brånemark PI (ed.) *Clinical Applications of Biomaterials*. Chichester: Wiley; 1982. p. 179-85.

48. Gilbert JL, Sivan S, Liu Y, Kocagöz SB, Arnholt CM, Kurtz SM. Direct in vivo inflammatory cell-induced corrosion of CoCrMo alloy orthopedic implant surfaces. *Journal of Biomedical Materials Research Part A*. 2015;103(1):211-23.

49. Hodgson AWE, Mueller Y, Forster D, Virtanen S. Electrochemical characterisation of passive films on Ti alloys under simulated biological conditions. *Electrochimica Acta*. 2002;47(12):1913-23.

50. Zsklarska-Smialowska Z. Pitting corrosion of metals. Houston, TX: National Association of Corrosion Engineers; 1986.

51. Burstein GT, Liu C, Souto RM. The effect of temperature on the nucleation of corrosion pits on titanium in Ringer's physiological solution. *Biomaterials*. 2005;26(3):245-56.

52. Burstein GT, Liu C. Nucleation of corrosion pits in Ringer's solution containing bovine serum. *Corrosion Science*. 2007;49(11):4296-306.

53. Knittel DR, Bronson A. Pitting Corrosion on Zirconium—A Review. *CORROSION*. 1984;40(1):9-14.

54. Palit GC, Gadiyar HS. Pitting corrosion of zirconium in chloride solution. *CORROSION*. 1987;43(3):140-8.

55. Palit GC, Elayaperumal K. Passivity and pitting of corrosion resistant pure metals Ta, Nb, Ti, Zr, Cr and Al in chloride solutions. *Corrosion Science*. 1978;18(2):169-79.

56. Postlethwaite J, Onofrei M. Hydrogen evolution and anodic disintegration during electrochemical pitting of zirconium in alkaline-chloride solutions. *CORROSION*. 1979;35(4):185-9.

57. Malik F. A study of passive films on valve metals. *Thin Solid Films*. 1991;206(1–2):345-8.

58. He X, Noël JJ, Shoesmith DW. Temperature Dependence of Crevice Corrosion Initiation on Titanium Grade 2. *Journal of the Electrochemical Society*. 2002;149(9):B440-B9.

59. Willert HG, Broback LG, Buchhorn GH, Jensen PH, Koster G, Lang I, Ochsner P, Schenk R. Crevice corrosion of cemented titanium alloy stems in total hip replacements. *Clinical Orthopaedics and Related Research*. 1996(333):51-75.

60. Hallam P, Haddad F, Cobb J. Pain in the well-fixed, aseptic titanium hip replacement - The role of corrosion. *Journal of Bone and Joint Surgery-British Volume*. 2004;86B(1):27-30.

61. Geetha M, Singh AK, Asokamani R, Gogia AK. Ti based biomaterials, the ultimate choice for orthopaedic implants - A review. *Progress in Materials Science*. 2009;54(3):397-425.

62. Gilbert JL, Buckley CA, Jacobs JJ. In vivo corrosion of modular hip prosthesis components in mixed and similar metal combinations. The effect

of crevice, stress, motion, and alloy coupling. *Journal of Biomedical Materials Research*. 1993;27(12):1533-44.

63. ASTM international. ASTM: STP12020S. Gilbert JL, Jacobs JJ. The mechanical and electrochemical processes associated with taper fretting crevice corrosion: A review. In: Marlowe DE, Parr JE, Mayor MB (eds.) *Modularity of orthopaedic implants*. West Conshohocken, United States: ASTM international; 1997, p.45-59.

64. Khan MA, Williams RL, Williams DF. In-vitro corrosion and wear of titanium alloys in the biological environment. *Biomaterials*. 1996;17(22):2117-26.

65. Jacobs JJ, Gilbert JL, Urban RM. Corrosion of metal orthopaedic implants. *Journal of Bone and Joint Surgery-American Volume*. 1998;80A(2):268-82.

66. Rodrigues DC, Urban RM, Jacobs JJ, Gilbert JL. In vivo severe corrosion and hydrogen embrittlement of retrieved modular body titanium alloy hip implants. *Journal of Biomedical Materials Research Part B*. 2009;88B(1):206-19.

67. Reclaru L, Meyer JM. Effects of fluorides on titanium and other dental alloys in dentistry. *Biomaterials*. 1998;19(1–3):85-92.

68. Mareci D, Bolat G, Cailean A, Santana JJ, Izquierdo J, Souto RM. Effect of acidic fluoride solution on the corrosion resistance of ZrTi alloys for dental implant application. *Corrosion Science*. 2014;87:334-343.

69. Huang HH. Effect of fluoride and albumin concentration on the corrosion behavior of Ti-6Al-4V alloy. *Biomaterials*. 2003;24(2):275-82.

70. Wang LN, Huang XQ, Shinbine A, Luo JL. Influence of albumin on the electrochemical behaviour of Zr in phosphate buffered saline solutions. *Journal of Materials Science: Materials in Medicine*. 2013;24(2):295-305.

71. Barao VA, Mathew MT, Assuncao WG, Yuan JC, Wimmer MA, Sukotjo C. The role of lipopolysaccharide on the electrochemical behaviour of titanium. *Journal of Dental Research*. 2011;90(5):613-8.

72. Souza JCM, Ponthiaux P, Henriques M, Oliveira R, Teughels W, Celis JP, Rocha, LA. Corrosion behaviour of titanium in the presence of Streptococcus mutans. *Journal of Dentistry*. 2013;41(6):528-34.

73. Menkin V. Biology of inflammation; chemical mediators and cellular injury. *Science*. 1956;123(3196):527-34.

74. Rajamäki K, Nordström T, Nurmi K, Åkerman KEO, Kovanen PT, Öörni K, Eklund KK. Extracellular Acidosis Is a Novel Danger Signal Alerting Innate Immunity via the NLRP3 Inflammasome. *The Journal of Biological Chemistry*. 2013;288(19):13410-9.

75. Roiniotis J, Dinh H, Masendycz P, Turner A, Elsegood CL, Scholz GM, Hamilton JA. Hypoxia prolongs monocyte/macrophage survival and enhanced glycolysis is associated with their maturation under aerobic conditions. *Journal of immunology.* 2009;182(12):7974-81.

76. Yu SY, Scully JR. Corrosion and passivity of Ti-13% Nb-13% Zr in comparison to other biomedical implant alloys. *CORROSION*. 1997;53(12):965-76.

77. Yu SY, Brodrick CW, Ryan MP, Scully JR. Effects of Nb and Zr alloying additions on the activation behaviour of Ti in hydrochloric acid. *Journal of the Electrochemical Society*. 1999;146(12):4429-38.

78. Pourbaix M. Atlas of Electrochemical Equilibria in Aqueous Solutions. Houston, Texas, USA: National Association of Corrosion Engineers; 1974.

79. Dyer CK, Leach JSL. Reversible reactions within anodic oxide films on titanium electrodes. *Electrochimica Acta*. 1978;23(12):1387-94.

80. Blackwood DJ, Peter LM, Williams DE. Stability and open circuit breakdown of the passive oxide film on titanium. *Electrochimica Acta*. 1988;33(8):1143-9.

81. Schutz RW. 2003 F.N. Speller Award Lecture: Platinum Group Metal Additions to Titanium: A Highly Effective Strategy for Enhancing Corrosion Resistance. CORROSION. 2003;59(12):1043-57.

82. Carlo MB, Stefania G, Alessia D, Carlo C. Oxygen, Reactive Oxygen Species and Tissue Damage. *Current Pharmaceutical Design*. 2004;10(14):1611-26.

83. Dupré-Crochet S, Erard M, Nüβe O. ROS production in phagocytes: why, when, and where? *Journal of Leukocyte Biology*. 2013;94(4):657-70.

84. Segal AW. How neutrophils kill microbes. *Annual Review of Immunology*. 2005;23(1):197-223.

85. Liu X, Ramsey MM, Chen X, Koley D, Whiteley M, Bard AJ. Real-time mapping of a hydrogen peroxide concentration profile across a polymicrobial bacterial biofilm using scanning electrochemical microscopy. *Proceedings of the National Academy of Sciences*. 2011;108(7):2668-73.

86. Tengvall P, Lundström I, Sjöqvist L, Elwing H, Bjursten LM. Titanium-hydrogen peroxide interaction: model studies of the influence of the inflammatory response on titanium implants. *Biomaterials*. 1989;10(3):166-75.

87. Fonseca C, Barbosa MA. Corrosion behaviour of titanium in biofluids containing H_2O_2 studied by electrochemical impedance spectroscopy. *Corrosion Science*. 2001;43(3):547-59.

88. Zhou FY, Wang BL, Qiu KJ, Li HF, Li L, Zheng YF, Han Y. In vitro corrosion behaviour and cellular response of thermally oxidized Zr-3Sn alloy. *Applied Surface Science*. 2013;265:878-88.

89. Sousa SR, Moradas-Ferreira P, Saramago B, Viseu Melo L, Barbosa MA. Human serum albumin adsorption on TiO_2 from single protein solutions and from plasma. *Langmuir*. 2004;20(22):9745-54.

90. Lefaix H, Prima F, Zanna S, Vermaut P, Dubot P, Marcus P, et al. Surface properties of a nano-quasicrystalline forming Ti based system. *Materials Transactions*. 2007;48(3):278-86.

91. Lima J, Sousa SR, Ferreira A, Barbosa MA. Interactions between calcium, phosphate, and albumin on the surface of titanium. *Journal of Biomedical Materials Research*. 2001;55(1):45-53.

92. Cheng XL, Roscoe SG. Corrosion behaviour of titanium in the presence of calcium phosphate and serum proteins. *Biomaterials*. 2005;26(35):7350-6.

93. Karimi S, Alfantazi AM. Electrochemical corrosion behaviour of orthopaedic biomaterials in presence of human serum albumin. *Journal of Electrochemical Society*. 2013;160(6):C206-C14.

94. Ouerd A, Alemany-Dumont C, Berthomé G, Normand B, Szunerits S. Reactivity of titanium in physiological medium: I. Electrochemical Characterization of the Metal/Protein Interface. *Journal of the Electrochemical Society*. 2007;154(10):C593-C601.

95. Contu F, Elsener B, Böhni H. Characterization of implant materials in fetal bovine serum and sodium sulfate by electrochemical impedance spectroscopy. I. Mechanically polished samples. *Journal of Biomedical Materials Research*. 2002;62(3):412-21.

96. Williams RL, Brown SA, Merritt K. Electrochemical studies on the influence of proteins on the corrosion of implant alloys. *Biomaterials*. 1988;9(2):181-6.

97. Karimi S, Alfantazi AM. Ion release and surface oxide composition of AISI 316L, Co–28Cr–6Mo, and Ti–6Al–4V alloys immersed in human serum albumin solutions. *Materials Science and Engineering: C*. 2014;40(0):435-44.

98. Karimi S, Nickchi T, Alfantazi AM. Long-term corrosion investigation of AISI 316L, Co–28Cr–6Mo, and Ti–6Al–4V alloys in simulated body solutions. *Applied Surface Science*. 2012;258(16):6087-96.

99. Karimi S, Nickchi T, Alfantazi A. Effects of bovine serum albumin on the corrosion behaviour of AISI 316L, Co-28Cr-6Mo, and Ti-6Al-4V alloys in phosphate buffered saline solutions. *Corrosion Science*. 2011;53(10):3262-72.

100. Mareci D, Bolat G, Chelariu R, Sutiman D, Munteanu C. The estimation of corrosion behaviour of ZrTi binary alloys for dental applications using electrochemical techniques. *Materials Chemistry and Physics*. 2013;141(1):362-9.

101. Okazaki Y, Tateishi T, Ito Y. Corrosion Resistance of Implant Alloys in Pseudo Physiological Solution and Role of Alloying Elements in Passive Films. *Materials Transactions, JIM*. 1997;38(1):78-84.

102. Clark GCF, Williams DF. The effects of proteins on metallic corrosion. *Journal of Biomedical Materials Research*. 1982;16(2):125-34.

103. Kocijan A, Milosev I, Pihlar B. The influence of complexing agent and proteins on the corrosion of stainless steels and their metal components. *Journal of Materials Science: Materials in Medicine*. 2003;14(1):69-77.

104. Sousa SR, Barbosa MA. Electrochemistry of AISI 316L stainless steel in calcium phosphate and protein solutions. *Journal of Materials Science: Materials in Medicine*. 1991;2(1):19-26.

105. Wagener V, Faltz AS, Killian MS, Schmuki P, Virtanen S. Protein interactions with corroding metal surfaces: comparison of Mg and Fe. *Faraday Discussions*. 2015;180:347-60.

106. Hedberg Y, Wang X, Hedberg J, Lundin M, Blomberg E, Wallinder IO. Surface-protein interactions on different stainless steel grades: effects of protein adsorption, surface changes and metal release. *Journal of Materials Science: Materials in Medicine*. 2013;24(4):1015-33.

107. Grebner T, Hansen DC. The effect of galvanic coupling between modern fracture fixation constructs in physiologically relevant solutions: the role of serum proteins on the corrosion of Ti6Al4V and 316L alloys. *ECS Transactions*. 2008;11(21):13-27.

108. Hedberg Y, Midander K. Size matters: mechanism of metal release from 316L stainless steel particles is governed by size-dependent properties of the surface oxide. *Materials Letters*. 2014;122:223-6.

109. Hedberg YS, Wallinder IO. Metal release from stainless steel in biological environments: A review. *Biointerphases*. 2016;11(1):17.

110. Nagassa ME, Daw AE, Rowe WG, Carley A, Thomas DW, Moseley R. Optimisation of the hydrogen peroxide pre-treatment of titanium: surface characterisation and protein adsorption. *Clinical Oral Implants Research*. 2008;19(12):1317-26.

111. Paul NE, Skazik C, Harwardt M, Bartneck M, Denecke B, Klee D, Salber J, Zwadlo-Klarwasser G. Topographical control of human macrophages by a regularly microstructured polyvinylidene fluoride surface. *Biomaterials*. 2008;29(30):4056-64.

112. Huang L, Zhang T, Liaw PK, He W. Macrophage responses to a Zr-based bulk metallic glass. *Journal of Biomedical Materials Research Part A*. 2014;102(10):3369-78.

113. Mantovani A, Sica A, Locati M. Macrophage Polarization Comes of Age. *Immunity*. 2005;23(4):344-6.

114. Tan HY, Wang N, Li S, Hong M, Wang X, Feng Y. The reactive oxygen species in macrophage polarization: reflecting its dual role in progression and treatment of human diseases. *Oxidative Medicine and Cellular Longevity*. 2016;2016:2795090.

115. Cadosch D, Al-Mushaiqri MS, Gautschi OP, Meagher J, Simmen H-P, Filgueira L. Biocorrosion and uptake of titanium by human osteoclasts. *Journal of Biomedical Materials Research Part A*. 2010;95A(4):1004-10.

116. Minkin C. Bone acid phosphatase: Tartrate-resistant acid phosphatase as a marker of osteoclast function. *Calcified Tissue International*. 1982;34(1):285-90.

117. Vaananen HK, Zhao H, Mulari M, Halleen JM. The cell biology of osteoclast function. *Journal of cell science*. 2000;113 (Pt 3):377-81.

118. Halleen JM, Raisanen S, Salo JJ, Reddy SV, Roodman GD, Hentunen TA, et al. Intracellular fragmentation of bone resorption products by reactive oxygen species generated by osteoclastic tartrate-resistant acid phosphatase. *The Journal of Biological Chemistry*. 1999;274(33):22907-10.

119. Lin HY, Bumgardner JD. In vitro biocorrosion of Ti-6Al-4V implant alloy by a mouse macrophage cell line. *Journal of Biomedical Materials Research Part A*. 2004;68A(4):717-24.

120. Esposito M, Lausmaa J, Hirsch JM, Thomsen P. Surface analysis of failed oral titanium implants. *Journal of Biomedical Materials Research*. 1999;48(4):559-68.

121. Esposito M, Thomsen P, Ericson LE, Lekholm P. Histopathologic observations on early oral implant failures. *International Journal of Oral & Maxillofacial Implants*. 1999;14(6):798-810.

122. Alsaadi G, Quirynen M, Komarek A, van Steenberghe D. Impact of local and systemic factors on the incidence of oral implant failures, up to abutment connection. *Journal of Clinical Periodontology*. 2007;34(7):610-7.

123. Koldsland OC, Scheie AA, Aass AM. Prevalence of peri-implantitis related to severity of the disease with different degrees of bone loss. *Journal of Periodontology*. 2010;81(2):231-8.

124. Academy report: Peri-implant mucositis and peri-implantitis: a current understanding of their diagnoses and clinical implications. *Journal of Periodontology*. 2013;84(4):436-43.

125. Ramanauskaite A, Juodzbalys G. Diagnostic principles of peri-implantitis: a systematic review and guidelines for peri-implantitis diagnosis proposal. *Journal of Oral & Maxillofacial Research*. 2016;7(3):e8.

126. Hanawa T. Metal ion release from metal implants. *Materials Science and Engineering: C*. 2004;24(6–8):745-52.

127. Willert HG, Buchhorn GH, Gobel D, Koster G, Schaffner S, Schenk R, Semlitsch M. Wear behavior and histopathology of classic cemented metal on metal hip endo-prostheses. *Clinical Orthopaedics and Related Research*. 1996(329 Suppl):S160-86.

128. Dalal A, Pawar V, McAllister K, Weaver C, Hallab NJ. Orthopedic implant cobalt-alloy particles produce greater toxicity and inflammatory cytokines than titanium alloy and zirconium alloy-based particles in vitro, in human osteoblasts, fibroblasts, and macrophages. *Journal of Biomedical Materials Research Part A*. 2012;100A(8):2147-58.

129. Monir M. XANES Study of Chemistry of Localised Corrosion in Artificial Pits of 316L Stainless Steel and Titanium. [Ph.D. thesis]. Birmingham: University of Birmingham; 2011

130. Holland RI. Corrosion testing by potentiodynamic polarization in various electrolytes*. Dental Materials*. 1992;8(4):241-5.

131. Pourbaix M. Electrochemical corrosion of metallic biomaterials. *Biomaterials*. 1984;5(3):122-34.

132. ASTM International. ASTM F2129-17. *Standard Test Method for Conducting Cyclic Potentiodynamic Polarization Measurements to Determine the Corrosion Susceptibility of Small Implant Devices*. West Conshohocken, United States: ASTM international; 2017.

133. ASTM international. ASTM F1801-97 A. *Standard Practice for Corrosion Fatigue Testing of Metallic Implant Materials*. West Conshohocken, United States: ASTM International; 2014.

134. ASTM international. ASTM F1875-98 A. *Standard Practice for Fretting Corrosion Testing of Modular Implant Interfaces: Hip Femoral Head-Bore and Cone Taper Interface*. West Conshohocken, United States: ASTM International; 2014.

135. Rettig R, Virtanen S. Time-dependent electrochemical characterization of the corrosion of a magnesium rare-earth alloy in simulated body fluids. *Journal of Biomedical Materials Research Part A*. 2008;85A(1):167-75.

136. Diamond RF cavities. *Bird's eye view of the synchrotron* Available from: http://www.diamond.ac.uk/Science/Machine/Components/rfcavity.html. [Accessed 2 May 2017]

137. Rayment T, Davenport AJ, Dent AJ, Tinnes JP, Wiltshire RJK, Martin C, Clark G, Quinn P, Mosselmans, JFW. Characterisation of salt films on dissolving metal surfaces in artificial corrosion pits via in situ synchrotron X-ray diffraction. *Electrochemistry Communications*. 2008;10(6):855-8.

138. Street SR, Xu WC, Amri M, Guo LY, Glanvill SJM, Quinn PD, Mosselmans JFW, Vila-Comamala J, Rau C, Rayment T, Davenport AJ. The effect of nitrate on salt layers in pitting corrosion of 304L stainless steel. *Journal of the Electrochemical Society*. 2015;162(9):C457-C64.

139. Xu WC, Street SR, Amri M, Mosselmans JFW, Quinn PD, Rayment T, Davenport AJ. In-situ synchrotron studies of the effect of nitrate on iron artificial pits in chloride solutions. *Journal of the Electrochemical Society*. 2015;162(6):C238-C42.

140. Xu WC, Street SR, Amri M, Mosselmans JFW, Quinn PD, Rayment T, Davenport AJ. In-situ synchrotron studies of the effect of nitrate on iron artificial pits in chloride solutions II. on the effect of carbon. *Journal of the Electrochemical Society*. 2015;162(6):C243-C50.

141. Tester JW, Isaacs HS. Diffusional Effects in Simulated Localized Corrosion. *Journal of the Electrochemical Society*. 1975;122(11):1438-45.

142. Yano J, Yachandra VK. X-ray absorption spectroscopy. *Photosynthesis Research*. 2009;102(2):241.

143. Rondelli G, Torricelli P, Fini M, Giardino R. In vitro corrosion study by EIS orthopaedic of a nickel-free stainless steel for applications. *Biomaterials*. 2005;26(7):739-44.

144. Hsu CH, Mansfeld F. Technical Note: Concerning the Conversion of the Constant Phase Element Parameter Y_0 into a Capacitance. *CORROSION*. 2001;57(9):747-8.

145. Martinez FO, Gordon S. The M1 and M2 paradigm of macrophage activation: time for reassessment. *F1000 Prime Reports*. 2014;6:13.

146. Mosselmans JFW, Quinn PD, Dent AJ, Cavill SA, Moreno SD, Peach A, Leicester PJ, Keylock SJ, Gregory SR, Atkinson KD, Rosell JR. I18 - the microfocus spectroscopy beamline at the Diamond Light Source. *Journal of Synchrotron Radiation*. 2009;16(6):818-24.

147. Basham M, Filik J, Wharmby MT, Chang PCY, El Kassaby B, Gerring M, Aishima J, Levik K, Pulford BCA, Sikharulidze I, Sneddon D, Webber M, Dhesi SS, Maccherozzi F, Svensson O, Brockhauser S, Náray G,

Ashton, AW. Data Analysis Workbench (DAWN). *Journal of Synchrotron Radiation*. 2015;22(Pt 3):853-8.

148. Roisnel T, Rodriguez-Carvajal J. A windows tool for powder diffraction patterns analysis Materials Science Forum. *Proceedings of the European Powder Diffraction Conference (EPDIC7)*. 2001;378-381:118-23.

149. Ravel B, Newville M. ATHENA, ARTEMIS, HEPHAESTUS: data analysis for X-ray absorption spectroscopy using IFEFFIT. *Journal of Synchrotron Radiation*. 2005;12(4):537-41.

150. Vyas N, Sammons RL, Addison O, Dehghani H, Walmsley AD. A quantitative method to measure biofilm removal efficiency from complex biomaterial surfaces using SEM and image analysis. *Scientific Reports*. 2016;6:32694.

151. Goldberg MB. Actin-Based Motility of Intracellular Microbial Pathogens. *Microbiology and Molecular Biology Reviews*. 2001;65(4):595-626.

152. Mosser DM, Edwards JP. Exploring the full spectrum of macrophage activation. *Nature Reviews Immunology*. 2008;8(12):958-69.

153. Dale DC, Boxer L, Liles WC. The phagocytes: neutrophils and monocytes. *Blood*. 2008;112(4):935-45.

154. Kusakawa Y, Yoshida E, Hayakawa T. Protein adsorption to titanium and zirconia using a quartz crystal microbalance method. *BioMed Research International*, 2017;2017:1521593.

155. Takemoto S, Hattori M, Yoshinari M, Kawada E, Oda Y. Corrosion behaviour and surface characterization of titanium in solution containing fluoride and albumin. *Biomaterials*. 2005;26(8):829-37.

156. Swanson HE, Fuyat RK. Standard X-ray diffraction powder patterns II. *National Bureau of Standards (U.S.) Circular.* 1953; 539(2):1-65.

157. Clearfield A, Vaughan PA. The crystal structure of zirconyl chloride octahydrate and zirconyl bromide octahydrate. *Acta Crystallographica*. 1956;9(7):555-8.

158. Bondars B, Heidemane G, Grabis J, Laschke K, Boysen H, Schneider J, Frey F. Powder diffraction investigations of plasma sprayed zirconia. *Journal of Materials Science*. 1995;30(6):1621-5.

159. Ghahari M, Krouse D, Laycock N, Rayment T, Padovani C, Stampanoni M, Marone F, Mokso R, Davenport AJ. Synchrotron X-ray radiography studies of pitting corrosion of stainless steel: Extraction of pit propagation parameters. *Corrosion Science*. 2015;100:23-35.

160. Messner CB, Hofer TS, Randolf BR, Rode BM. Structure and dynamics of the Zr(4+) ion in water. *Physical Chemistry Chemical Physics: PCCP*. 2011;13(1):224-9.

161. Zielen AJ, Connick RE. The hydrolytic polymerization of zirconium in perchloric acid solutions. *Journal of the American Chemical Society*. 1956;78(22):5785-92.

162. Hagfeldt C, Kessler V, Persson I. Structure of the hydrated, hydrolysed and solvated zirconium(iv) and hafnium(iv) ions in water and aprotic oxygen donor solvents. A crystallographic, EXAFS spectroscopic and large angle X-ray scattering study. *Dalton Transactions*. 2004(14):2142-51.

163. Langford JI, Wilson AJC. Scherrer after sixty years: A survey and some new results in the determination of crystallite size. *Journal of Applied Crystallography*. 1978;11(2):102-13.

164. Williamson GK, Hall WH. X-ray line broadening from filed aluminium and wolfram. *Acta Metallurgica*. 1953;1(1):22-31.

165. Hu MZC, Harris MT, Byers CH. Nucleation and growth for synthesis of nanometric zirconia particles by forced hydrolysis. *Journal of Colloid and Interface Science*. 1998;198(1):87-99.

166. Srinivasan R, Harris MB, Simpson SF, De Angelis RJ, Davis BH. Zirconium oxide crystal phase: The role of the pH and time to attain the final pH for precipitation of the hydrous oxide. *Journal of Materials Research*. 1988;3(4):787-97.

167. Clearfield A. The mechanism of hydrolytic polymerization of zirconyl solutions. *Journal of Materials Research*. 1990;5(1):161-2.

168. Garvie RC, Swain MV. Thermodynamics of the tetragonal to monoclinic phase transformation in constrained zirconia microcrystals. *Journal of Materials Science*. 1985;20(4):1193-200.

169. Golish SR, Anderson PA. Bearing surfaces for total disc arthroplasty: metal-on-metal versus metal-on-polyethylene and other biomaterials. *The Spine Journal*. 2012;12(8):693-701.

170. Willert HG, Semlitsch M. Reactions of the articular capsule to wear products of artificial joint prostheses. *Journal of Biomedical Materials Research*. 1977;11(2):157-64.

171. Popa MV, Vasilescu E, Drob P, Vasilescu C. Electrochemical stability of a new Ti base bioalloy in simulated human fluids. In: Dossel O, Schlegel WC (eds.) *World Congress on Medical Physics and Biomedical Engineering*, September 7-12, 2009, Munich, Germany. IFMBE Proceedings, vol 25/10. Springer, Berlin, Heidelberg.

172. ASTM international. ASTM: STP37561S. Hallab NJ, Anderson S, Caicedo M, Jacobs JJ. Zirconium and niobium affect human osteoblasts, fibroblasts, and lymphocytes in a similar manner to more traditional implant alloy metals. In: L. Zardiackas, H. Freese, and M. Kraay (ed.) *Titanium, Niobium, Zirconium, and Tantalum for Medical and Surgical Applications*. West Conshohocken, United States: ASTM International; 2006, p. 248-259. https://doi.org/10.1520/STP37561S

173. Di Laura A, Hothi HS, Meswania JM, Whittaker RK, de Villiers D, Zustin J, Blunn GW, Skinner JA, Hart AJ . Clinical relevance of corrosion patterns attributed to inflammatory cell-induced corrosion: A retrieval study. *Journal of Biomedical Materials Research Part B*. 2017;105(1):155-64.

174. Altuna P, Lucas-Taulé E, Gargallo-Albiol J, Figueras-Álvarez O, Hernández-Alfaro F, Nart J. Clinical evidence on titanium-zirconium dental implants: a systematic review and meta-analysis. *International Journal of Oral and Maxillofacial Surgery*.45(7):842-50.

175. Chiapasco M, Casentini P, Zaniboni M, Corsi E, Anello T. Titanium–zirconium alloy narrow-diameter implants (Straumann Roxolid®) for the rehabilitation of horizontally deficient edentulous ridges: prospective study on 18 consecutive patients. *Clinical Oral Implants Research*. 2012;23(10):1136-41.

176. Morrison ML, Buchanan RA, Peker A, Peter WH, Horton JA, Liaw PK. Cyclic-anodic-polarization studies of a $Zr_{41.2}Ti_{13.8}Ni_{10}Cu_{12.5}Be_{22.5}$ bulk metallic glass. *Intermetallics*. 2004;12(10–11):1177-81.

177. Hiromoto S, Tsai AP, Sumita M, Hanawa T. Polarization behavior of bulk Zr-base amorphous alloy immersed in cell culture medium. *Materials Transactions*. 2002;43(12):3112-7.

178. Hiromoto S, Asami K, Tsai A-P, Sumita M, Hanawa T. Surface composition and anodic polarization behaviour of zirconium-based amorphous alloys in a phosphate-buffered saline solution. *Journal of the Electrochemical Society*. 2002;149(4):B117-B22.

179. Michel R, Hofmann J, Loer F, Zilkens J. Trace-element burdening of human-tissues due to the corrosion of hip-joint prosthesis made of cobalt-chromium alloys. *Archives of Orthopaedic and Trauma Surgery*. 1984;103(2):85-95.

180. Dobbs HS, Minski MJ. Metal-ion release after total hip-replacement. *Biomaterials*. 1980;1(4):193-8.

181. Sunderman FW, Jr., Hopfer SM, Swift T, Rezuke WN, Ziebka L, Highman P, Edwards B, Folcik M, Gossling HR. Cobalt, chromium, and

nickel concentrations in body fluids of patients with porous-coated knee or hip prostheses. *Journal of Orthopaedic Research*. 1989;7(3):307-15.

182. Davenport AJ, Dent AJ, Monir M, Hammons JA, Ghahari SM, Quinn PD, Rayment T. XANES Study of the Chemistry of Molybdenum in Artificial Corrosion Pits in 316L Stainless Steel. *Journal of the Electrochemical Society*. 2011;158(5):C111-C7.

183. Moreno JMC, Vasilescu E, Drob P, Osiceanu P, Vasilescu C, Drob SI, Popa M. Surface analysis and electrochemical behaviour of Ti-20Zr alloy in simulated physiological fluids. *Materials Science and Engineering: B*. 2013;178(18):1195-204.

184. Zhang YM, Chai F, Hornez JC, Li CL, Zhao YM, Traisnel M, Hildebrand HF. The corrosion and biological behaviour of titanium alloys in the presence of human lymphoid cells and MC3T3-E1 osteoblasts. *Biomedical Materials*. 2009;4(1).

185. Han MK, Hwang MJ, Yang MS, Yang HS, Song HJ, Park YJ. Effect of zirconium content on the microstructure, physical properties and corrosion behavior of Ti alloys. *Materials Science and Engineering: A*. 2014;616(0):268-74.

186. Cui W, Liu N, Qin G. Microstructures, mechanical properties and corrosion resistance of the ZrxTi (Ag) alloys for dental implant application. *Materials Chemistry and Physics.* 2016;176:161-166.

187. Winterbourn CC, Hampton MB, Livesey JH, Kettle AJ. Modeling the reactions of superoxide and myeloperoxidase in the neutrophil phagosome - Implications for microbial killing. *Journal of Biological Chemistry*. 2006;281(52):39860-9.

188. Shkirskiy V, King AD, Gharbi O, Volovitch P, Scully JR, Ogle K, Birbilis N. Revisiting the Electrochemical Impedance Spectroscopy of Magnesium with Online Inductively Coupled Plasma Atomic Emission Spectroscopy. *Chemphyschem*. 2015;16(3):536-9.

189. ASTM international, ASTM: STP16073S. Mishra, A., Davidson, J., Poggie, R., Kovacs, P., and FitzGerald, T., Mechanical and Tribological Properties and Biocompatibility of Diffusion Hardened Ti-13Nb-13Zr — A New Titanium Alloy for Surgical Implants, In: S. Brown and J. Lemons (eds.) *Medical Applications of Titanium and Its Alloys: The Material and Biological Issues*. West Conshohocken, United States: ASTM International; 1996, p. 96-113, https://doi.org/10.1520/STP16073S